UNIVERSITY OF CALIFORNIA, SAN DIEGO

Gravity changes associated with underground injection of CO_2 at the Sleipner storage reservoir in the North Sea, and other marine geodetic studies.

A dissertation submitted in partial satisfaction of the
requirements for the degree Doctor of Philosophy
in
Earth Sciences

By

Scott L. Nooner

Committee in charge:

Mark A. Zumberge, Chair
Donna K. Blackman
Ahmed-Waeil Elgamal
Robert L. Parker
Glenn S. Sasagawa
Fred N. Spiess

2005

The dissertation of Scott L. Nooner is approved, and it is acceptable in quality and form for publication on microfilm:

Chair

University of California, San Diego

2005

"There's two possible outcomes: if the result confirms the hypothesis, then you've made a discovery. If the result is contrary to the hypothesis, then you've made a discovery."

–Enrico Fermi

TABLE OF CONTENTS

LIST OF FIGURES

LIST OF TABLES

ACKNOWLEDGEMENTS

I would like to express my gratitude to everyone who helped make completion of this dissertation possible, even if I don’t mention every name. There are a few specific names I will mention, however.

Mark Zumberge has been my advisor for almost six years—the entire time I’ve been at SIO. Throughout this time, he has been a consistent source of feedback and good advice. From his example of hands on hard work I have learned some key elements essential for good research, including the importance of careful diligence. Through working with Mark, I have been exposed to a wide range of research (more than is included in this dissertation), and for that I am certainly better off. I could not have had a better advisor, and I have enjoyed working with him.

Glenn Sasagawa has also played an important role in most of my research, particularly in dealing with gravity and gravimeters. Donna Blackman helped my early work significantly. Bob Parker taught me valuable skills in classes and provided computer code that I have used many times. Fred Spiess, has provided insightful feedback throughout. In fact, I would like to thank all of the members of my PhD committee (Mark Zumberge, Glenn Sasagawa, Donna Blackman, Bob Parker, Fred Spiess, and Ahmed-Waeil Elgamal) for their help in formulating and carrying out a research plan.

Bill Chadwick at Oregon State University played a vital role in my work at Axial Seamount. The work on Sleipner could not have been completed without the

help of Ola Eiken at Statoil in Norway, Sjur Mo at SINTEF in Norway, and the SACS consortium. Torkjell Stenvold and Håvard Alnes also contributed. Other important SIO faculty and staff include Yuri Fialko, Dave Sandwell, Duncan Agnew, Cathy Constable, Freeman Gilbert, Peter Shearer, Graham Kent, and Kitty Haak.

My fellow students and peers also played a significant role throughout my time here. Six years ago Jim Behrens, Christine Reif, and Bridgette Smith all started out in the Kellar. Numerous discussions and blackboard sessions helped to illuminate many problems. Jim Behrens, Adrian Borsa, and Kerry Key, all helped through scientific discussions and through non-science activities, from playing music to rock climbing. Dylan McNamara has provided valuable friendship over the years. Fiona Sutherland also provided years of conversation. Derick Hugunin has also been a good friend for many years. I thank Allison Smith for her encouragement and support when I decided to move to San Diego and study geophysics. For all of these friends I am grateful.

This work has been supported by the United States Department of Energy, Statoil, Saline Aquifer CO_2 Store, the National Oceanic and Atmospheric Administration, the National Science Foundation, and the University of California San Diego.

I would also like to thank my family, especially my parents Bruce and Linda Nooner, who have been supportive of everything I've done…ever. Finally, I want to thank Kate Brody, who has given me unending love and encouragement since the day we met.

The material in Chapter 3 is an expanded version of the material as it appears in Chadwick, W. W., Nooner, S. L., Zumberge, M. A., Embley, R. W., and Fox, C. G., Vertical deformation monitoring at Axial Seamount since its 1998 eruption using deep-sea pressure sensors, *Journal of Volcanology and Geothermal Research*, (in press) 2005. I was the primary researcher on the material presented here, and the secondary author on the paper. Mark Zumberge and William Chadwick directed and supervised the research which forms the basis of this chapter, with contributions from the other co-authors.

The material in Chapter 4 is a reprint of the material as it appears in Nooner, S.L, G.S. Sasagawa, D.K. Blackman, and M.A. Zumberge, Structure of oceanic core complexes: Constraints from seafloor gravity measurements made at the Atlantis Massif, *Geophysical Research Letters*, 30(8), 1446-1449, 2003. I was the primary researcher and author on the paper. Mark Zumberge directed and supervised the research which forms the basis of this chapter, with contributions from the other co-authors.

VITA

June 1, 1974	Born, Conway, Arkansas
1996	B.A., Hendrix College
1996-1999	Teaching Assistant, Texas A&M University
1999	M.S., Texas A&M University
1999-2005	Research Assistant, University of California, San Diego
2005	Ph.D., Earth Sciences, University of California, San Diego

PUBLICATIONS

Blackman, D.K., B. Applegate, N. Bacher, G.L. Fruh-Green, J. Gee, H. Hanna, S. Hurst, B. John, S. Lyons, J. Morgan, S. Nooner, P. Rivizzigno, D. Ross, G. Sasagawa, and T. Schroeder, Seafloor mapping and sampling of the MAR 30° N oceanic core complex-MARVEL (Mid-Atlantic Ridge vents in extending lithosphere), *InterRidge News*, *10* (1), 33-36, 2000.

Blackman, D.K., J.A. Karson, D.S. Kelley, J.R. Cann, G.L. Fru-Green, J.S. Gee, S.D. Hurst, B.E. John, J. Morgan, S.L. Nooner, D.K. Ross, T.J. Schroeder, and E.A. Williams, Geology of the Atlantis Massif (Mid-Atlantic Ridge, 30° N): Implications for the evolution of an ultramafic oceanic core complex, *Marine Geophysical Researches*, *23*, 443-469, 2003.

Nooner, S.L., G.S. Sasagawa, D.K. Blackman, and M.A. Zumberge, Structure of oceanic core complexes: Constraints from seafloor gravity measurements made at the Atlantis Massif, *Geophysical Research Letters*, *30* (8), 1446-1449, 2003.

Sasagawa, G.S., W. Crawford, O. Eiken, S. Nooner, T. Stenvold, and M.A. Zumberge, A new sea-floor gravimeter, *Geophysics*, *68* (2), 544-553, 2003.

Zumberge, M.A., J. Berger, M.A. Hedlin, E. Husmann, S. Nooner, R. Hilt, and R. Widmer-Schnidrig, An optical fiber infrasound sensor: A new lower limit on atmospheric pressure noise between 1 and 10 Hz, *Journal of the Acoustical Society of America*, *113* (5), 2474-2479, 2003.

Chadwick, W.W., S.L. Nooner, M.A. Zumberge, R.W. Embley, and C.G. Fox, Vertical deformation monitoring using deep-sea pressure sensors, *Journal of Volcanology and Geothermal Research*, in press, 2005.

ABSTRACT OF THE DISSERTATION

Gravity changes associated with underground injection of CO_2 at the Sleipner storage reservoir in the North Sea, and other marine geodetic studies.

by

Scott L. Nooner
Doctor of Philosophy in Earth Sciences
University of California, San Diego, 2005
Mark Zumberge, Chair

Three studies involving high precision measurements of gravity and water pressure on the seafloor are presented. In the first, baseline gravity and pressure measurements have been made over the Sleipner project in the North Sea. At this site, CO_2 is being separated from recovered natural gas and sequestered by injection into a saline aquifer about 1000 m below the seafloor for environmental reasons. Ultimately, time-lapse gravity and pressure measurements will be used to constrain the density of CO_2 within the reservoir, and improve estimates of captured CO_2 mass to insure the long-term safety of the technique. Modeling of time-lapse 3-D seismic data and reservoir simulation models indicates a maximum expected change in gravity of 2-8 μGal/yr, depending on the reservoir temperature (hence CO_2 density). Data from the baseline gravity survey in 2002 show a repeatability of 4.3 μGal. A repeat survey is expected in the summer of 2005, allowing a three-year signal accumulation.

The second study makes use of high precision water pressure measurements made on seafloor benchmarks as a proxy for seafloor height to monitor volcanic inflation associated with the movement of magma within Axial Seamount since its 1998 eruption. Five years of vertical deformation data obtained from campaign style pressure measurements show inflation of up to 20 cm/yr. Modeling of the deformation data indicates an inflationary source located 1.7 km SSE of the caldera center and located at a depth of 3-5 km. If inflation continues at the current rate, the caldera will fully re-inflate to its pre-eruption level by 2014, suggesting recurrence interval of ~16 years.

The final study is a spatial gravity survey of the Atlantis Massif oceanic-core complex. Modeling of the gravity measurements indicates that the massif has wedge-shaped core of increased density, 3150-3250 kg/m^3 on average, consistent with seismic data suggesting that partially serpentinized to unaltered peridotite exist less than 1 km below the seafloor in this area. The observed wedge-like geometry of the core is consistent with the unroofing of deep-seated rock by extension and rotation along a detachment fault.

Chapter 1

Introduction

1.1 Gravity and water pressure as geodetic tools

The Earth's surface is slowly but constantly changing in response to both natural and human induced phenomena. Natural sources of surface deformation are numerous, however, the primary sources are from the motion of tectonic plates that make up the crust and by heat from the core and mantle. These sources are manifested as surface deformation via motion along faults, seismic and aseismic, and upwelling of molten rock at volcanoes and mid-ocean ridges. However, the strain accumulation caused by plate motion often requires sensitive instruments to detect. Similarly, in volcanic systems, movement of magma below the surface is often unaccompanied by an eruptive event, but precise measurements can enable us to observe surface deformation. Additionally, the gravitational attraction of the moon and the sun stress the Earth as it moves through space, causing periodic solid earth tides that must be accounted for in any high precision geodetic survey. Seasonal subsidence and rebound also occur in many places due to changes in the local water table during wet and dry seasons. Human induced deformation (primarily subsidence) arising from large-scale actions such as subterranean mining and withdrawal of fluids (ground water, petroleum, geothermal) occurs in nearly every state in the United States. In fact, subsidence is one of the most diverse forms of ground failure, ranging from small or local collapses to broad regional lowering of the earth's surface. For example, in the last fifty years subsidence of up to 2 m in the Las Vegas area and up to 1 m in the Houston area has accumulated from the removal of groundwater, gas, and oil [*Galloway et al.*, 1999] (more information can be found at http://water.usgs.gov/).

Many of the events leading to surface deformation are caused by the movement of subsurface mass. The result is often a net change in the local mass over time. For example, in an oil or natural gas field the mass of the liquid hydrocarbon is removed from the reservoir, causing a mass decrease. The rate of mass change provides information about the total recoverable reserves, making this a desirable quantity to measure. In a volcanic system, deformation is typically caused by the subsurface movement of magma, leading directly to changes in the amount or location of mass within the system. Understanding how a volcanic system behaves requires knowledge about the movement of subsurface mass.

Mogi [1958] proposed a simple model that relates the deformation source to observed surface deformation, which does a good job accounting for deformation data in many cases. The model assumes that a spherical inflation source of radius R is buried in a uniform elastic half-space at a depth d. If the pressure change is ΔP, the vertical deformation Δz is given by the equation

$$\Delta z(x) = \frac{3R^3 \Delta P}{4\mu} \frac{d}{(d^2 + x^2)^{3/2}} \qquad 1.1.1$$

where x is the radial distance from the uplift center along the surface, and μ is the shear modulus of the elastic half-space. Poisson's ratio ν is assumed to be 1/4. The formulation is valid only in the point source approximation, when $R/d << 1$. *McTigue* [1987] developed a more complete solution, allowing source depths comparable to the source radius. More complicated deformation models have been proposed for other source geometries such as a penny shaped crack or sill [*Fialko et al.*, 2001], a dipping prolate spheroid [*Yang et al.*, 1988], and an arbitrarily oriented ellipsoidal cavity [*Davis*, 1983]. Differentiation between the models requires high precision data with very good spatial coverage. For this reason, the Mogi model is often all that is required by the data. Studies using only surface deformation to study volcanoes and reservoirs are numerous [e.g. *Amelung et al.*, 1999; *Davis*, 1983; *Dvorak and Dzurisin*, 1997; *Dzurisin*, 2003; *Hoffman et al.*, 2001; *Segall and Davis*, 1997; *Zebker et al.*, 2000]. By applying deformation models such as the Mogi model, surface deformation data can provide estimates of source depth and volume change. However, using only surface deformation measurements, assumptions about the density of the subsurface mass must be made.

Local changes in mass or density can be observed directly by either drilling expensive monitoring wells or by using non-invasive and less expensive gravity measurements with commercially made instruments. For instance, volcanic research combining surface deformation and gravity measurements on land is extensive and can provide additional insight on the density of the deformation source [*Berrino et al.*, 1992; *Jachens and Eaton*, 1980; *Jachens and Roberts*, 1985; *Johnson et al.*, 1980;

McKee et al., 1989; *Rymer*, 1994; *Rymer and Brown*, 1989; *Sasagawa and Zumberge*, 1991; *Williams-Jones and Rymer*, 2002; *Zumberge et al.*, 1986]. Table 1.1, reproduced from *Rymer* , summarizes observations for a selection of highly active volcanoes. The range of observed ratios of gravity change to height change, $\Delta g/\Delta z$, varies from 50% to 200% of the free air gravity gradient (-3 μGal/cm), depending on factors such as density, gas content, and structural changes of the magma conduits. (Note: 1 μGal $\equiv 1\times10^{-8}$ m/s^2.)

For example, observations of $\Delta g/\Delta z$ at Campi Flegri from 1982-1984 indicate mass injection during inflation ($\Delta g/\Delta z$ = -2.15 μGal/cm), but observations from 1985-1990 indicate even greater mass loss per unit deformation ($\Delta g/\Delta z$ = -1.20 μGal/cm). It was proposed that magma drainage with incomplete void collapse was occurring during subsidence. Observations at Krafla, Iceland, indicate mass injection during inflation and even greater mass loss during subsidence, via lateral movement through fissures into dykes (for a summary see *Berrino et al.* [1992]).

Jachens and Roberts [1985] established a network of several dozen stations in and around Long Valley Caldera and completed several surveys there in the early 1980s. The network was surveyed again by *Battaglia et al.* [1999], taking advantage of the long accumulated deformation that occurred in the intervening period (more than 10 years). Atop the resurgent dome, the authors observed a 107 ± 6 μGal decrease in gravity and a 421 ± 34 mm increase in altitude, with an average $\Delta g/\Delta z$ = -2.15 ± 0.11 μGal/cm. They determined that an intrusive material of density 3.3 ± 0.6 g/cm^3 (95% confidence) has been responsible for the deformation.

Table 1.1 Gravity and elevations changes observed at a selection of volcanoes; reproduced from Table 1 of *Rymer* . Maximum observed values are shown for gravity and elevation changes. The $\Delta g/\Delta z$ ratios are typical values computed from all observation sites used by the authors, not simply the maximum values observed.

Volcano	Epoch	Max Δg (μGal)	Max Δz (cm)	$\Delta g/\Delta z$ (μGal/cm)	Reference
Kilauea	11/75 - 12/ 75	234	-131	-1.71	[*Jachens and Eaton*, 1980]
Kilauea	12/75 - 4/77	145	-80	-6.07	[*Dzurisin et al.*, 1980]
Kilauea	4/77 - 10/77	140	-45	-2.80	[*Dzurisin et al.*, 1980]
Yellowstone	1977-1987	-60	12	-1.70	[*Smith et al.*, 1989]
Campi Flegri	1981-1984	-331	161	-2.15	[*Berrino et al.*, 1992]
Rabaul	1971-1985	-410	180	-2.16	[*McKee et al.*, 1989]
Krafla	Jan 1978	150	-90	-1.66	[*Johnson et al.*, 1980]

These same techniques can be applied to reservoir management studies. For example, gravity has been used for monitoring hydrothermal energy fields [e.g. *Allis and Hunt*, 1986; *Andres and Pedersen*, 1993] and Prudhoe Bay oil field where water is being injected into the reservoir to enhance production rates [*Hare et al.*, 1999].

On land, surface deformation can be measured by leveling surveys, the Global Positioning System (GPS), interferometric synthetic aperture radar (InSAR), borehole extensometers, tiltmeters, and other techniques [*Dvorak and Dzurisin*, 1997; *Dzurisin*, 2003; *Segall and Davis*, 1997; *Zebker et al.*, 2000]. Submarine geodetic studies, however, are limited in number, despite the geophysical and industrial benefits such research would provide. For instance, much of the Earth's volcanic activity takes place on the seafloor, at hot spots and mid-ocean ridges, but very few time-evolution studies have been done. Additionally, oil companies are exploiting a large number of offshore reservoirs that would benefit from geodetic monitoring. Additionally, if reservoir geometry is known from 3-D reflection seismic data, measuring surface deformation and gravity together will allow an even more precise quantification of mass changes. However, since neither the land deformation monitoring methods or commercial gravimeters can be readily used underwater, new techniques and instruments have been developed recently to monitor both horizontal and vertical deformation, as well as gravity change on the seafloor.

One of the most promising techniques for measuring vertical seafloor deformation has been the use of bottom pressure recorders (BPRs), instruments that continuously record ambient pressure, as a proxy for seafloor depth [*Fox*, 1999; *Fujimoto et al.*, 2003; *Watanabe et al.*, 2004]. BPRs are good at detecting rapid deformation, however, gauge drift limits their ability to quantify long-term deformation signals. Additional measurements using campaign style mobile pressure recorders (MPRs) are not subject to long-term drift effects, so provide much better constraints on average long-term vertical deformation [*Chadwick et al.*, 2005 (in press); *Sasagawa et al.*, 2003]. MPR measurements, however, are not sensitive to rapid episodic deformation.

Other techniques that have been developed for making geodetic measurements on the seafloor include direct acoustic ranging between pairs of instruments [*Chadwell et al.*, 1999; *Chadwick et al.*, 1999; *Chadwick and Stapp*, 2002; *Nagaya et al.*, 1999] and combined GPS/acoustic positioning of instruments on the bottom from surface ships [*Chadwell et al.*, 1995; *Fujimoto et al.*, 1998; *Fujita et al.*, 2003; *Hildebrand et al.*, 2000; *Osada et al.*, 2003; *Spiess et al.*, 1998]. Simultaneous gravity and pressure measurements have been made on the seafloor with an instrument developed at Scripps Institution of Oceanography, for offshore reservoir monitoring [*Eiken et al.*, 2000; *Sasagawa et al.*, 2003]. This instrument is called the ROVDOG for Remotely Operated Vehicle deployed Deep Ocean Gravimeter.

1.2 Major problems studied

The focus of the work presented in this dissertation is on using both the ROVDOG instrument and MPRs to examine three interesting geophysical problems on the seafloor. The first is a reservoir monitoring case in the North Sea, known as the Sleipner project, where carbon dioxide is being separated from recovered natural gas and then re-injected into a saline aquifer about 1000 m below the sea floor. In the second study, an MPR package is used to quantify vertical deformation over Axial volcano, located along the Juan de Fuca Ridge. The third study uses the ROVDOG instrument to examine the spatial density structure of the Atlantis Massif, an oceanic core complex located on the Mid-Atlantic Ridge (MAR).

The first two studies involve time-lapse measurements of gravity and/or pressure, while the third (on the MAR) does not. This is an important distinction, since the first two are looking at mass or density *changes* within the Earth's crust over a relatively short time and the third is looking at *in situ* spatial density variations to learn about geologic structure. Typically, terrain corrections are a significant source of uncertainty for spatial gravity surveys on the seafloor, due to the large footprint of the available bathymetry. This problem is exacerbated in areas with steep or rough topography. Time-lapse gravity measurements, on the other hand, utilize repeat observations at fixed benchmarks so that any terrain effects are effectively constant over time. Thus, time-lapse gravity measurements are robust against such errors. For both time-lapse and spatial surveys, time variable gravity and pressure signals due to tides are dealt with by tidal modeling or by recording reference pressure data at a fixed location during the survey. The uncertainty introduced from the tides is normally on the order of a few mm in depth and a few μGal in gravity.

The research presented in this dissertation involves relatively new geophysical instruments and techniques. Therefore, improvements in the instruments and survey methodology were made as experience was gained. In addition to addressing some interesting geophysical questions, this work will serve as a partial documentation of some of the important things I learned about making high precision seafloor gravity and pressure measurements over the last six years.

1.3 Instrumentation

The two instrument packages used in the studies presented here are the ROVDOG and a standalone MPR. The ROVDOG instrument is essentially a land gravimeter modified for remote operation on the seafloor. The gravity sensor core from a Scintrex CG-3M was extracted and mounted in a compact leveling mechanism. A microcontroller oversees the leveling platform and controls data collection, and other circuitry provides power, pressure measurements, signal conditioning, and system monitoring. The instrument assembly is mounted in a watertight pressure case, which can be transported and deployed by a number of different vehicles. The ROVDOG is linked to the vehicle by a flexible cable so that it can be placed on the seafloor during measurements, thus decoupling it from vehicle vibrations. A remote operator controls the instrument and can review and record the data in real time.

Multiple sensors can be deployed simultaneously on the same frame. This increases the number of measurements made without incurring additional survey time. More details can be found in *Sasagawa et al*. [2003] and in Appendix 1.

Instrument depth during ROVDOG or MPR surveys is measured with Paroscientific quartz pressure gauges (model 31K for depths from 0-700 m or model 410K for depths from 700-7000 m). The gauges are housed either within the ROVDOG pressure cases or within a stand-alone pressure case for the MPR, and are coupled to seawater through high-pressure ports. The manufacturer specifies an accuracy of 0.01% of full scale. By averaging the results of several gauges, the precision can be improved. The specific gauges used in each survey are given in Appendix 2. More detail on the MPR instrument is given in Chapter 3.

1.4 Organization of the dissertation

Chapter 2 describes the Sleipner project in the North Sea, where carbon dioxide is being injected into an underground saline aquifer for long-term storage. This chapter describes the project in detail, including background, previous work, and the seafloor gravity work I have done. Chapter 3 discusses the inflation of Axial Seamount as measured by water pressure measurements on seafloor benchmarks. Parts of this chapter have been accepted for publication. Chapter 4 describes a spatial gravity study of the Atlantis Massif, located at 30 ºN along the Mid-Atlantic Ridge. This chapter has been previously published. Finally, conclusions and an outline for further research are given in Chapter 5.

1.5 References

Allis, R.G., and T.M. Hunt, Analysis of expoitation-induced gravity changes at Wairakei geothermal field, *Geophysics*, *51*, 1647-1660, 1986.

Andres, R.B., and J.R. Pedersen, Monitoring the Bullalo geothermal reservoir, Philippines, using precision gravity data, *Geothermics*, *22*, 395-402, 1993.

Battaglia, M., C. Roberts, and P. Segall, Magma intrusion beneath Long Valley Caldera confirmed by temporal changes in gravity, *Science*, *285*, 2119-2122, 1999.

Berrino, G., H. Rymer, G.C. Brown, and C. Corado, Gravity-height correlations for unrest at calderas, *Journal of Volcanology and Geothermal Research*, *53*, 11-26, 1992.

Cann, J.R., and M.R. Strens, Modeling periodic megaplume emission by black smoker systems, *Journal of Geophysical Research*, *94*, 12,227-12,237, 1989.

Chadwell, C.D., J.A. Hildebrand, F.N. Spiess, J.L. Morton, W.R. Normark, and C.A. Reiss, No spreading across the southern Juan de Fuca ridge axial cleft during 1994-1996, *Geophysical Research Letters*, *26* (16), 2525-2528, 1999.

Chadwell, C.D., F.N. Spiess, J.A. Hildebrand, L. Prawirodirdjo, L.E. Young, G.H. Purcell, and H. Dragert, The Juan de Fuca Ridge geodesy project: Strain and plate motion measurements using GPS and acoustics, *Eos Transactions American Geophysical Union*, *76* (46, Fall Meeting suppl.), F412, 1995.

Chadwick, W.W., Jr., R.W. Embley, H.B. Milburn, C. Meinig, and M. Stapp, Evidence for deformation associated with the 1998 eruption of Axial Volcano, Juan de Fuca Ridge, from acoustic extensometer measurements, *Geophysical Research Letters*, *26* (23), 3441-3444, 1999.

Chadwick, W.W., Jr., and M. Stapp, A deep-sea observatory experiment using acoustic extensometers: Precise horizontal distance measurements across a mid-ocean ridge, *IEEE Journal of Oceanic Engineering (Special Issue on Ocean Observatories)*, *27* (2), 193-201, 2002.

Chadwick, W.W., S.L. Nooner, M.A. Zumberge, R.W. Embley, and C.G. Fox, Vertical deformation monitoring using deep-sea pressure sensors, *Journal of Volcanology and Geothermal Research*, submitted, 2005 (in press).

Davis, P.M., Surface deformation due to inflation of an arbitrarily oriented triaxial ellipsoidal cavity in an elastic half-space, with reference to Kilauea Volcano, Hawaii, *Journal of Geophysical Research*, *91*, 7429-7438, 1983.

Dvorak, J.J., and D. Dzurisin, Volcano geodesy: The search for magma reservoirs and the formation of eruptive vents, *Reviews of Geophysics*, *35* (3), 343-384, 1997.

Dzurisin, D., A comprehensive approach to monitoring volcano deformation as a window on the eruption cycle, *Reviews of Geophysics*, *41* (1), 1001, doi:10.1029/2001RG000107, 2003.

Dzurisin, D., L.A. Anderson, G.P. Eaton, R.Y. Koyanagi, P.W. Lipman, K.M. Lockwood, R.T. Okamura, G.S. Puniwai, M.K. Sako, and K.M. Yamashita, Geophysical observations of Kilauea volcano, Hawaii, 2. Constraints on the magma supply during November 1975-September 1977., *Journal of Volcanology and Geothermal Research*, *7*, 241-269, 1980.

Eiken, O., M.A. Zumberge, and G. Sasagawa, Gravity monitoring of offshore gas reservoirs, in *Proceedings of the Society for Exploration Geophysics*, Calgary, August 2000, 2000.

Fialko, Y., Y. Khazan, and M. Simons, Deformation due to a pressurized horizontal circular crack in an elastic half-space, with applications to volcano geodesy, *Geophysical Journal International*, *146* (1), 181-190, 2001.

Fofonoff, N.P., Physical properties of seawater: A new salinity scale and equation of state for seawater, *Journal of Geophysical Research*, *90* (C2), 3332-3342, 1985.

Fox, C.G., In situ ground deformation measurements from the summit of Axial Volcano during the 1998 volcanic episode, *Geophysical Research Letters*, *26* (23), 3437-3440, 1999.

Fujimoto, H., K. Koizumi, Y. Osada, and T. Kanazawa, Development of instruments for seafloor geodesy, *Earth, Planets, and Space*, *50*, 905-911, 1998.

Fujimoto, H., M. Mochizuki, K. Mitsuzawa, T. Tamaki, and T. Sato, Ocean bottom pressure variations in the southeastern Pacific following the 1997-98 El Nino event, *Geophysical Research Letters*, *30* (9), 1456, 2003.

Fujita, M., M. Sato, T. Yabuki, M. Mochizuki, and A. Asada, Examination on repeatability of GPS/Acoustic seafloor positioning for the reference points deployed around Japan, *Eos Transactions American Geophysical Union*, *84* (46, Fall Meet. Suppl.), Abstract G21D-0297, 2003.

Galloway, D.L., D.R. Jones, and S.E. Ingebritsen, Land subsidence in the United States, *U.S. Geological Survey Circular*, *1182*, 1999.

Hare, J.L., J.F. Ferguson, C.L.V. Aiken, and J.L. Brady, The 4-D microgravity method for aterflood surveillance: A model study for the Prudhoe Bay reservoir, Alaska, *Geophysics*, *64*, 78-87, 1999.

Hildebrand, J.A., C.D. Chadwell, S.M. Wiggins, and F.N. Spiess, Offshore geodetic monitoring on the southeast flank of Kilauea Volcano (abstract), *Seismological Research Letters*, *71* (2), 232, 2000.

Jachens, R.C., and G.P. Eaton, Geophysical observations of Kilauea volcano, Hawaii, 1. temporal gravity variations related to the 29 November, 1975, M=7.2 earthquake and associated summit collapse, *Journal of Volcanology and Geothermal Research*, *7*, 225-240, 1980.

Jachens, R.C., and C.W. Roberts, Temporal and areal gravity investigations at Long Valley Caldera, California, *Journal of Geophysical Research*, *90*, 11210-11218, 1985.

Johnson, G.V., A. Björnsson, and S. Sigurdsson, Gravity and elevation changes caused by magma movement beneath the Krafla caldera, Northeast Iceland, *Journal of Geophysical Research*, *47*, 132-140, 1980.

McKee, C., J. Mori, and B. Talai, Microgravity changes and ground deformation at Rabaul caldera, 1973-1985, in *Volcanic Hazards: Assessment and Monitoring. IAVCEI Proceedings in Volcanology 1.*, edited by J.H. Latter, pp. 399-428, Springer, Berlin, 1989.

McTigue, D.F., Elastic sress and deformation near a finite spherical magma body: resolution of the point source paradox, *Journal of Geophysical Research*, *92*, 12931-12940, 1987.

Mogi, K., Relations between the eruptions of various volcanoes and the deformation of the ground surfaces around them, *Bulletin of the Earthquake Research Institute, University of Tokyo*, *36*, 99-134, 1958.

Nagaya, Y., T. Urabe, and T. Yabuki, Crustal deformation observation at the crest of the EPR 18.5S with the seafloor acoustic ranging method, *Eos Transactions American Geophysical Union*, *80* (46, Fall Meeting suppl.), F1076, 1999.

Osada, Y., H. Fujimoto, S. Miura, A. Sweeney, T. Kanazawa, S. Nakao, S. Sakai, J.A. Hildebrand, and C.D. Chadwell, Estimation and correction for the effect of sound velocity variation on GPS/Acoustic seafloor positioning: An experiment off Hawaii Island, *Earth, Planets, and Space*, *55*, e17-e20, 2003.

Rymer, H., Microgravity changes as a precursor to volcanic activity, *Journal of Volcanology and Geothermal Research*, *61*, 311-328, 1994.

Rymer, H., and G.C. Brown, Gravity changes as a precursor to volcanic eruptions at Poás volcano, Costa Rica, *Nature*, *342*, 902-905, 1989.

Sasagawa, G., W. Crawford, O. Eiken, S. Nooner, T. Stenvold, and M. Zumberge, A new sea-floor gravimeter, *Geophysics*, *68*, 544-553, 2003.

Sasagawa, G., and M.A. Zumberge, Absolute gravity measurements in California, 1984-1989, *Journal of Geophysical Research*, *96* (B2), 2501-2513, 1991.

Segall, P., and J.L. Davis, GPS applications for geodynamics and earthquake studies, *Annual Reviews of Earth and Planetary Science*, *25*, 301-336, 1997.

Smith, R.B., R.E. Reilinger, C.M. Meertens, J.R. Hollis, S.R. Holdahl, D. Dzurisin, W.K. Gross, and E.E. Klingele, What's moving at Yellowstone? The 1987 crustal deformatioin survey from GPS, levelling, precision gravity, and trilateratioin, *Eos Transactions American Geophysical Union*, *70*, 113-125, 1989.

Spiess, F.N., C.D. Chadwell, J.A. Hildebrand, L.E. Young, G.H. Purcell, Jr., and H. Dragert, Precise GPS/Acoustic positioning of seafloor reference points for tectonic studies, *Physics of the Earth and Planetary Interiors*, *108* (2), 102-112, 1998.

Watanabe, T., H. Matsumoto, H. Sugioka, H. Mikada, and K. Suyehiro, Offshore monitoring system records recent earthquake off Japan's Northernmost island, *Eos Transactions American Geophysical Union*, *85* (2), 14, 2004.

Williams-Jones, G., and H. Rymer, Detecting volcanic eruption precursors: a new method using gravity and deformation measurements, *Journal of Volcanology and Geothermal Research*, *113*, 379-389, 2002.

Yang, X.-M., P.M. Davis, and J.H. Dietrick, Deformation from inflation of a dipping finite prolate spheroid in an elastic half-space as a model for volcanic stressing, *Journal of Geophysical Research*, *93* (B5), 4249-4257, 1988.

Zebker, H.A., F. Amelung, and S. Jonsson, Remote sensing of volcano surface and internal processes using radar interferometry, in *Remote Sensing of Active Volcanism*, edited by P.J. Mouginis-Mark, J.A. Crisp, and J.H. Fink, pp. 179-206, American Geophysical Union, Washington, D.C., 2000.

Zumberge, M.A., G. Sasagawa, and M. Kappus, Absolute gravity measurements in California, *Journal of Geophysical Research*, *91* (B9), 9135-9144, 1986.

Chapter 2

Gravity changes from carbon dioxide injected into a sub-seafloor saline aquifer in the North Sea

2.1 Introduction

2.1.1 Motivation

The beginning of the Industrial Revolution (1700-1800) ushered in a new era in the history of mankind and of the Earth. Advancing technology led to the development of things such as steam engines, sky scrapers, electricity, and the internal combustion engine. As technology has advanced over the past 250 years, the human population of the world has been growing at an increasingly faster rate (Figure 2.1), leading to greater energy consumption. This energy has been generated primarily from burning coal and liquid hydrocarbons, which release CO_2 (carbon dioxide), methane, and nitrous oxide as by-products. These by-product gases are called "greenhouse gases," since they absorb infared radiation emitted from the Earth's surface, effectively warming the atmosphere. Another consequence of rapid population growth is large-scale deforestation as people seek new places to live and land to farm. This is important since plants require CO_2 for photosynthesis, thus serving as natural CO_2 "sinks." Increasing CO_2 sources and decreasing CO_2 sinks has led to elevating levels of carbon dioxide CO_2 in the atmosphere over the past 250 years (Figure 2.1) [e.g., *Keeling and Whorf*, 2005]. In fact, carbon dioxide made up about 83 percent of the greenhouse gases emitted in the United States in 2003. Tied to this, there has been a 0.6 °C increase in the global average temperature in the past century. This has lead scientists to study the potential consequences of increasing atmospheric carbon dioxide in the context of global climate and the carbon cycle.

Climate change is not new for the Earth. Throughout its history, the Earth's climate has varied naturally, as indicated, for example, by global average temperature variations inferred from isotopic fractions of ^{18}O in an ice core from Vostok,

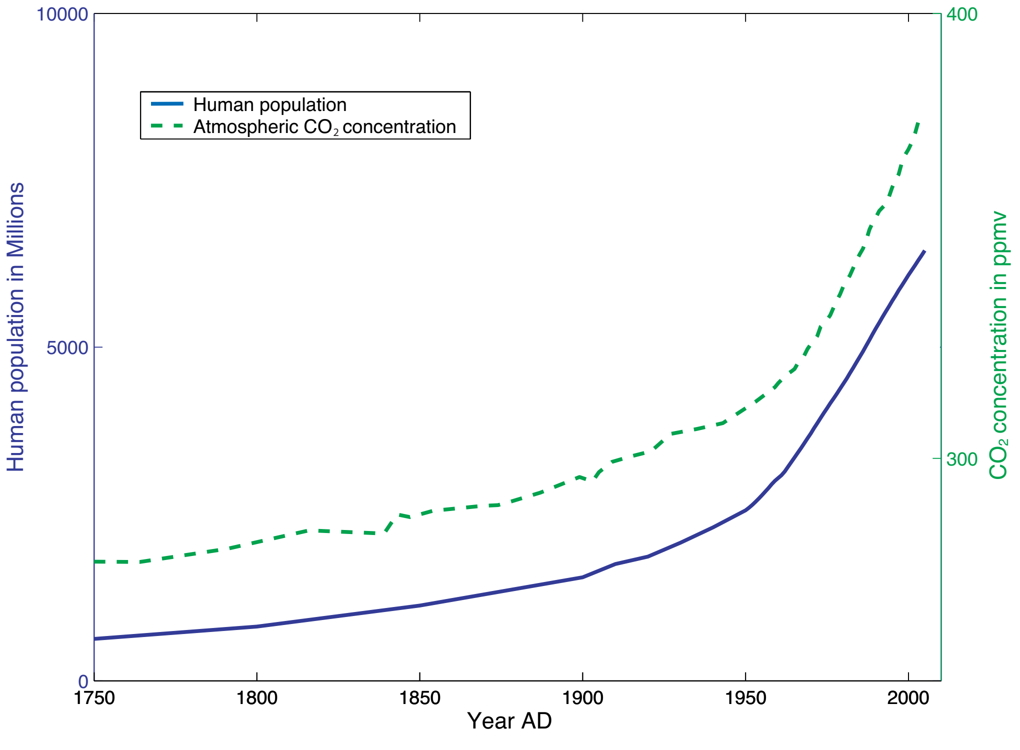

Figure 2.1 This plot shows the increase in human population (blue line) and the increase in atmospheric CO_2 (in parts per million by volume) for the last 250 years. They are both increasing, suggesting a relationship between the two. The data is available at http:\\cdiac.esd.ornl.gov.

Antarctica (Figure 2.2a) [*Petit et al.*, 1999; *Petit et al.*, 2000]. In fact, there seems to be some periodicity to the climate changes (Figure 2.2). Similarly, the levels of atmospheric carbon dioxide have varied over time (Figure 2.2). Entrapped air inclusions in the ice core provide a direct record of past changes in atmospheric gas composition. A comparison between past atmospheric CO_2 content [*Barnola et al.*, 1987; *Barnola et al.*, 2003] and global average temperature (Figure 2.2) indicates that there is a relationship between the two: whenever atmospheric concentration of CO_2 is higher, global average temperatures are generally higher.

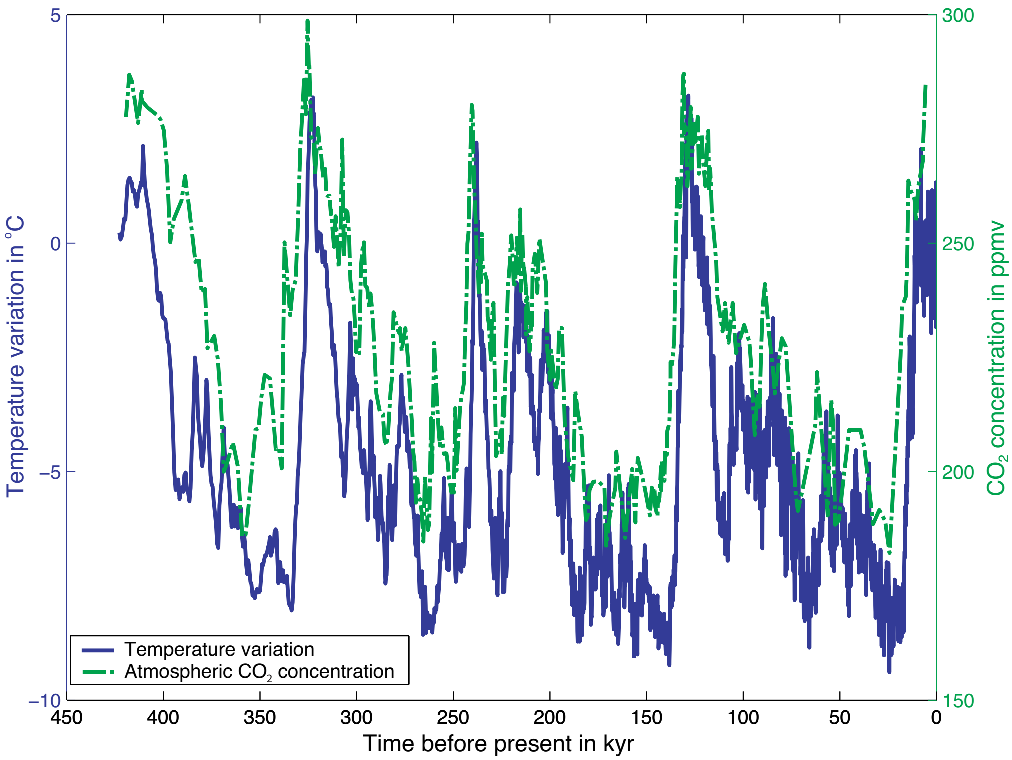

Figure 2.2 This plot shows the relationship between the global temperature variation (blue line) and the atmospheric CO_2 content (in parts per million by volume). Time is given in kyr before present. The data for this plot is inferred from an ice core from Vostok, Antarctica, and is available at http://cdiac.esd.ornl.gov/.

If current trends continue, the atmospheric levels of CO_2 will double the pre-industrial levels this century. Climate models indicate the possibility of a rapid climate change with up to 5.4 °C increase in the global average temperature by the year 2100 [*Murphy et al.*, 2004]. One recent model even suggests the possibility of an 11 °C increase [*Stainforth et al.*, 2005]. Some warming is certain, but how much will be determined by cycles involving melting ice, the ocean, water vapor, clouds and changes to vegetation. The current warming trend is likely to cause extinctions of numerous endangered plants and animals, increasingly severe storms, floods and droughts, as well as a rise in sea-level. In any case, it is clear that an overstressed world with 6.3 billion people is a risky place to carry out uncontrolled experiments with the climate.

In March 1992, the first International Conference on Carbon Dioxide Removal (ICCDR-1) took place in Amsterdam. Since that time, funding agencies such as the U.S. Department of Energy (DOE) have established programs in carbon sequestration. Equally important, industry has been analyzing and developing needed sequestration technologies. Public awareness and concern about human induced climate change has led to the ratification of the Kyoto Protocol in November 2004. This international agreement requires countries to reduce greenhouse gas emissions by about 5% below 1990 levels by 2012. It also lays out framework and incentives for developing and sharing related technologies. Although the Kyoto Protocol is an important first step, and illustrates global awareness of the problem, it is only the beginning of what needs to be done to mitigate anthropogenic climate change. One problem is that four industrialized countries have not yet ratified the agreement: United States of America (the single largest carbon emitter), Australia, Monaco, and Liechtenstein. Together, these countries account for over one-third of the greenhouse gases emitted by the industrialized world. Additionally, underdeveloped countries such as China and India are exempt from the requirements of the protocol. Furthermore, even if there is a 5% reduction in emissions relative to 1990 levels, atmospheric levels of CO_2 will still be increasing.

In addition to increasing energy efficiency and shifting to non-fossil energy sources (renewables and nuclear), removing CO_2 from the atmosphere by enhancing its uptake in soils and vegetation (e.g. afforestation), ocean sequestration (e.g. iron fertilization and CO_2 hydrates), and storage in geologic formations (e.g. depleted oil reservoirs, coal seams, and saline aquifers) are needed in order to minimize human induced climate change. For this study, we are interested in sequestration in geologic formations.

Sequestration of CO_2 in geologic formations builds on nearly a century of technology developed for oil and natural gas production and storage. For example, CO_2 capture and injection for economic benefit, such as for enhanced oil recovery (EOR), has been utilized for a number of years. There are three primary mechanisms for carbon capture in geologic formations: 1. CO_2 can be trapped as a gas or supercritical fluid under a low-permeability caprock. 2. CO_2 can be dissolved in a liquid such as oil or brine. 3. CO_2 can react with minerals and organic matter within the formations to become part of the solid mineral matrix. Generally, all three mechanisms occur simultaneously. The rest of this chapter focuses on a specific case of geologic sequestration of CO_2 in the North Sea, known as the Sleipner Project. Specifically, sections 2.1.1 to 2.1.4 describe the Sleipner Project in more detail and provide a background on work that has been done there by others. Sections 2.2 onward discuss the work that I have done to contribute to the project.

2.1.2 The Sleipner Project

The Sleipner Project is the world's first commercial application of emissions avoidance through the use of carbon capture and sequestration technologies. The Sleipner field is a natural gas production area located about 240 km off the coast of Norway in the North Sea (Figure 2.3) and operated by Statoil. In order for natural gas drawn from the site to meet commercial specifications, its CO_2 content must be reduced from about 9% to 2.5%. In gas fields worldwide, this excess CO_2 is typically vented into the atmosphere, but at Sleipner the CO_2 is compressed and injected into a porous saline aquifer known as the Utsira formation (Figures 2.3 and 2.4). Injection began in 1996 at a gradually increasing rate. Now, about 1 million tons (MT) of CO_2 are being separated from the natural gas and injected into the Utsira formation each year.

Because CO_2 has never been compressed and injected in to an underground formation for environmental sequestration, some method of monitoring the CO_2 is necessary in order to confirm that this is a safe and reliable sequestration option. Additionally, quantification and verification of carbon removal is a key aspect of the Kyoto protocol. In 1999, the European Union (EU), industry, and national governments funded a demonstration project called SACS (Saline Aquifer CO_2 Store) to begin evaluating the geological aspects of the subsurface CO_2 disposal. This involved assessing the capacity, storage properties, and performance of the Utsira reservoir, as well as modeling CO_2 migration within the reservoir, and monitoring the

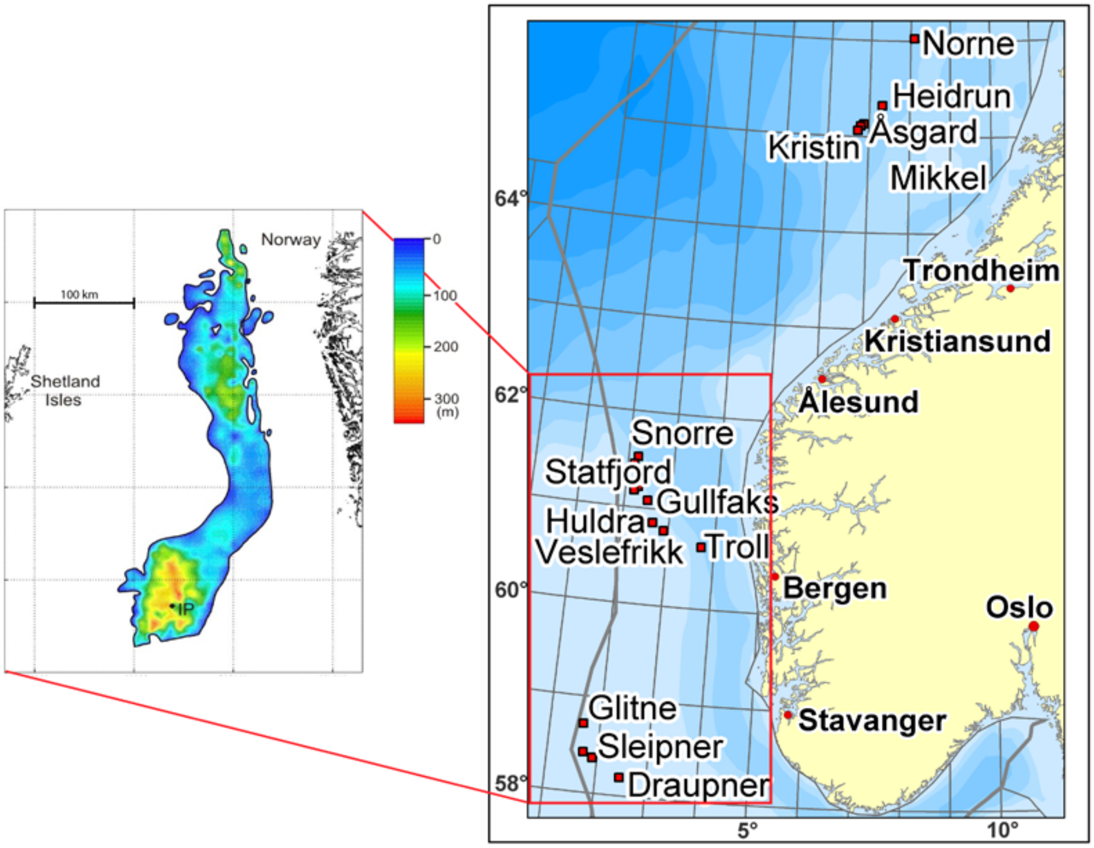

Figure 2.3 The location of the Sleipner platform is indicated in the lower left of the map. The other red squares indicate the location of other gas and oil fields operated by Statoil (taken from http://www.statoil.com). The blow up to the left shows the extent of the Utsira formation. Colors represent thickness of the Utsira sand. The CO_2 injection point is indicated by IP. Tick marks are spaced 100 km apart.

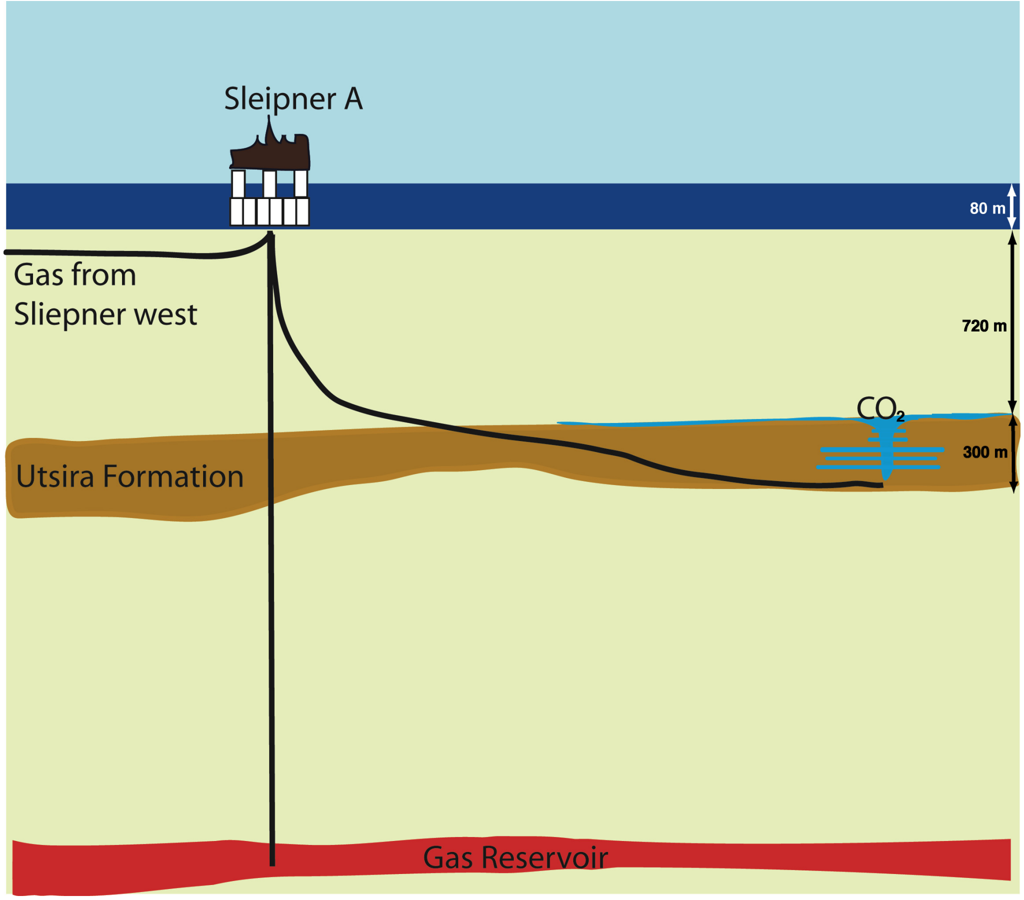

Figure 2.4 Cartoon illustrating the CO_2 injection operation at Sleipner. CO_2 is separated from the incoming gas, then injected into the Utsira formation. Approximate dimensions are given on the right side of the figure.

dispersal of the CO_2 with geophysical techniques. The SACS project ended in 2002, but the work is being carried on in the EU and industry funded CO2STORE project (http://www.co2store.org) in order to firmly establish the long-term safety of geological CO_2 storage.

2.1.3 The Utsira formation

The Utsira formation is a long narrow sand formation, spanning over 400 km north to south and 50-100 km west to east beneath a large portion of the central North

Sea (Figure 2.3). The aquifer extends from a depth of about 1100 m below sea level (bsl) to about 800 m bsl, where it is capped by a 200-300 m thick shale caprock. It consists of fine to medium grained, moderately well sorted sand, cut by intra-reservoir shale layers with an average thickness of about 1 m [*Zweigel et al.*, 2004]. The presence of these thin shale layers is evident from well log data but is below the resolution of the seismic data. Porosity of the sand was determined to range from 35% to 40% [*Holloway et al.*, 2000; *Zweigel et al.*, 2004], and the sand is almost completely unconsolidated. It has been estimated that the Utsira formation is potentially capable of storing 205,000 to 271,000 MT of CO_2 [*Chadwick et al.*, 2000; *Holloway et al.*, 2000]. The Utsira sand is about 300 m thick in the Sleipner area, but the shale layers segment the sand into 30 m thick sections, on average. Although the thin intra-Utsira shale layers may constitute hydrologic barriers, inhibiting vertical flow in the reservoir, they are not believed to be completely sealing [*Zweigel et al.*, 2004].

The Ustira sand is underlain by shaly sediments exhibiting deformations due to the presence of mud diapers and mud volcanoes. The direct overburden consists of clay rich sediments with a thickness of about 250 m in the Sleipner area. This is in turn overlain by several hundreds of meters of coarser grained Quaternary sediments [*Zweigel et al.*, 2004]. *Eidvin et al.* [1999] determined that the age of the Utsira formation a few km south of the CO_2 injection site ranges from late middle Miocene (about 11 Myr) to early late Pliocene (about 3 Myr).

Long-term storage of CO_2 will likely be accommodated by morphological features termed ‘structural traps’ at the top of the Utsira. Therefore, the CO_2 injection site is positioned below a 1.2 km wide dome structure in the top of the Utsira sand. The height of the dome is about 12 m, below which are spillpoints or channels linking the dome with other domal structures in the region. The injection point is at a depth of 1012 m bsl and the water depth is about 80 m.

2.1.4 Time-lapse reflection seismic

In addition to a pre-injection 3-D seismic survey obtained by Statoil in 1996, SACS collected 3-D seismic data over the Sleipner area in October 1999 after 2.35 MT of CO_2 had been injected and again in October 2001 after about 4.26 MT of CO_2 had been injected. Another survey was completed in 2002, but, for the most part, that data set is not included here. The results of the 1999 and 2001 seismic surveys both clearly show a signal from the injected CO_2 (Figure 2.5). By 1999, the CO_2 had reached the top of the Utsira sand and has since been spreading laterally. One slice of the time-lapse results is shown in Figure 2.5. The high amplitude sub-horizontal reflections are caused by accumulation of CO_2 under thin inter-reservoir shale layers [*Arts et al.*, 2002a; *Chadwick et al.*, 2002; *Chadwick et al.*, 2004], which act as temporary barriers to bouyantly driven CO_2 flow. The increased seismic response is due to two factors. First, the seismic impedance contrast between the shale and the sandstone becomes larger in magnitude whenever CO_2 is present. Second, the reflectivity is a result of interference between the top and bottom reflection of the CO_2 layers. The interference is either constructive or destructive depending on the thickness of the CO_2 layer. Maximum constructive interference occurs at a CO_2 thickness of about 8 m, the 'tuning thickness' [*Arts et al.*, 2002a].

Seismic velocity was modeled as a function of CO_2 saturation using Gassmann's relationships, which are valid for low frequencies [e.g., *Han and Batzle*, 2004; *Mavko and Mukerji*, 1998; *Nolen-Hoeksema*, 2000; *Wang et al.*, 1998]:

$$K_{sat} = K_{dry} + \frac{(1 - K_{dry}/K_{min})^2}{\frac{\phi}{K_{fl}} + \frac{1-\phi}{K_{min}} - \frac{K_{dry}}{K_{min}^2}}, \qquad 2.1.1$$

$$\mu_{sat} = \mu_{dry}, \qquad 2.1.2$$

where ϕ is the porosity; K_{min}, K_{sat}, K_{dry}, and K_{fl} are the bulk moduli of the mineral, the saturated rock, the dry rock, and the pore fluid; and μ_{sat} and μ_{dry} are the shear moduli of the saturated and dry rock. These relationships enable the elastic properties of a porous medium saturated with a fluid to be derived from the known properties of the same medium saturated with a different fluid, assuming that the densities and compressibilities of all rock and fluids are known. Seismic velocities are then related to the shear modulus, μ, and bulk modulus, K, by

$$V_p = \sqrt{\frac{K + \frac{4\mu}{3}}{\rho}}, \qquad 2.1.3$$

$$V_s = \sqrt{\frac{\mu}{\rho}}, \qquad 2.1.4$$

where ρ is the bulk density. Because the rock matrix in the Utsira sand is weak, the compressional velocity (equation 2.1.3) is very sensitive to the compressibility of the fluid. Figure 2.6 [*courtesy of Ola Eiken, Andy Chadwick, and Rob Arts*] shows the P-wave velocity versus % CO_2 saturation for the Utsira sand as predicted by Gassmann's relationships for different values of reservoir temperature (compare the uniform saturation curves), which directly affects the bulk moduli through CO_2 density. This figure illustrates that, for a uniform saturation, the P-wave velocity drops from 2050 m/s for water saturated sand and then is relatively constant at less than 1450 m/s for CO_2 saturations of 20-100%. CO_2 densities of 550 kg/m^3 and 700 kg/m^3 are assumed for Figure 2.6 (uncertainty in the density is discussed in the next section, 2.1.4). The decrease in P-wave velocity due to the presence of CO_2 is known as the seismic pushdown effect, as events beneath the CO_2 layers are delayed in travel time, causing the layers to appear pushed down on the record section. This can be seen on the seismic data in Figure 2.5 as an apparent downward dip in the reflective layers, increasing towards the center. The amount of pushdown increased from 1999 to 2001 since more CO_2 was in place.

A vertical chimney of CO_2 can be seen as a more localized sharp V-profile superimposed on the broader pushdown profile (Figure 2.5). This chimney is thought to consist of moderate to high saturation CO_2, causing rapid buildup of pushdown within the chimney itself. The main chimney is located almost directly above the injection point, within the 95% confidence ellipse for the well position, suggesting a relationship between the two. However, it is possible that the location of the chimney is affected by local geology. The large amount of CO_2 and therefore pushdown within the chimney causes the layer geometry and reflections to blur out near the bottom of

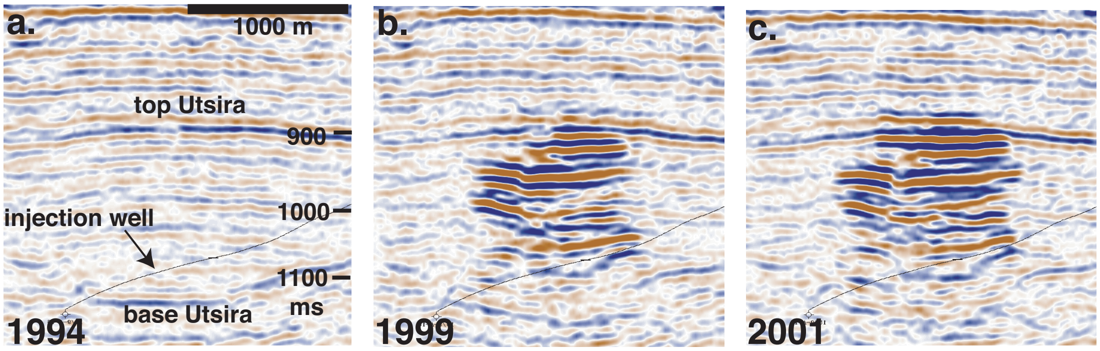

Figure 2.5 This figure shows the time-evolution of an east-west slice through the 3-D seismic reflection data. a.) Seismic profile before CO_2 injection, b.) after three years of injection, and c) after 5 years of injection. Data for this figure were provided by Ola Eiken and the SACS Consortium.

the reservoir. Similar but less prominent features can also be seen in the data and are interpreted as smaller chimneys.

A key element of time-lapse monitoring is its ability to quantify the amount of *in situ* CO_2 and thereby to test the efficacy of the injection operation. *Arts et al.* [2002b] and *Chadwick et al*. [2002] made estimates of the CO_2 mass within the Utsira sand in 1999 using the seismically imaged volume (from the high amplitude reflections) and the velocity pushdown. *Chadwick et al*. [2002] calculated the CO_2 mass in the following way: 1. They first calculated the mass within the highly reflective, thin-layers of CO_2. To do this, the thickness of the layers at each point had to be estimated. This was done by deriving a relationship between reflection amplitude and layer thickness based on synthetic seismic calculations and verified by actual data. The maximum layer thickness was taken as the tuning thickness of 8 m. The CO_2 saturation within the layers was determined from a capillary pressure - saturation relationship, which was obtained from laboratory experiments on the Utsira

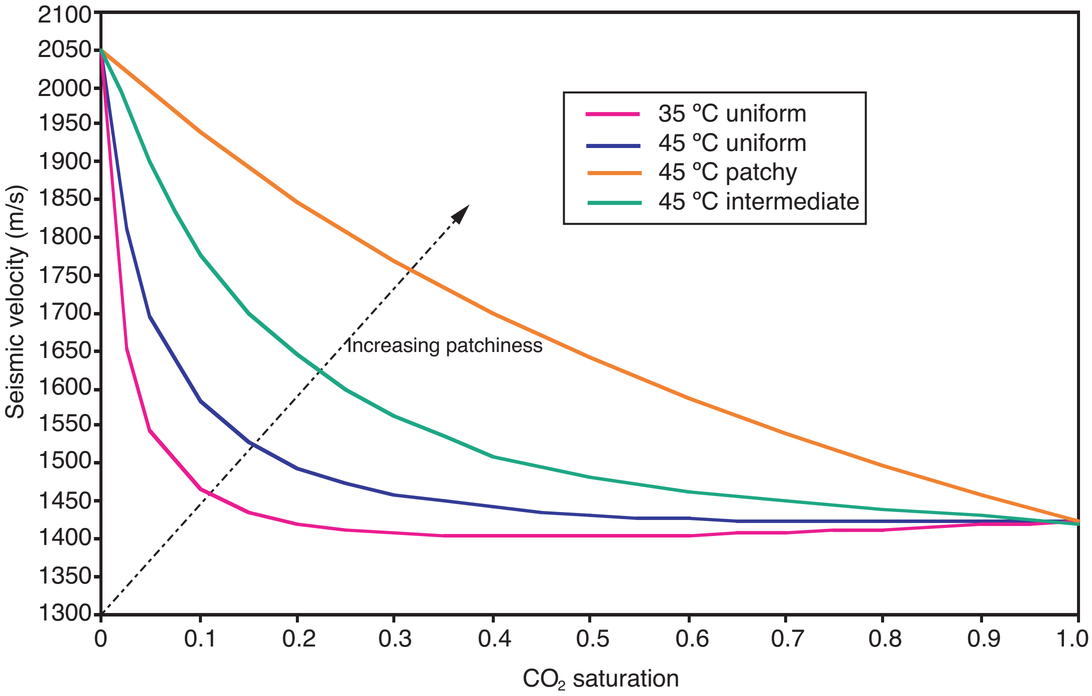

Figure 2.6 Velocity versus CO_2 saturation curves derived from Gassman's relationships for the Utsira formation. The pink curve is for a uniform saturation with the reservoir temperature of 35 ºC and ρ_{CO_2} = 700 kg/m^3. The blue curve is for a uniform saturation at 45 ºC and ρ_{CO_2} = 550 kg/m^3. The orange curve is for a patchy saturation at 45 ºC and ρ_{CO_2} = 550 kg/m^3, and the green curve is for the same reservoir temperature but with an intermediately patchy distribution of CO_2. The two temperatures represent the expected end member scenarios for the reservoir. This figure is courtesy of Ola Eiken, Andy Chadwick, and Rob Arts.

sand. It relates distance from the base of the layer in meters, *h*, to CO_2 saturation, S_{CO2} in the following way:

$$\Delta\rho g h = p_c = 810.35(1 - S_{CO2})^{-0.948} \qquad 2.1.5$$

where p_c is the capillary pressure in Pa, $\Delta\rho$ is the difference in density between water and carbon dioxide, and g is gravity in m/s^2 [*Chadwick et al.*, 2002; *Chadwick et al.*, 2004]. Finally, using the layer thickness, CO_2 saturation, a porosity of 0.37, and assuming a CO_2 density of 700 kg/m^3, the total mass of CO_2 in the layers was computed. 2. The theoretical velocity pushdown was then calculated from the velocity versus saturation curves (Figure 2.6) derived from Gassmann's relationships (Equations 2.1.1 and 2.1.2) then subtracted from the total observed pushdown to obtain a residual pushdown. 3. The residual pushdown was then inverted for the remaining unaccounted for CO_2 mass. This mass was required to be in a diffuse, low-saturation volume since it did not contribute any noticeable change in seismic reflection amplitude. 4. Finally, the mass calculated from the layers was added to mass calculated from the residual pushdown to obtain the total estimated mass of CO_2. Assuming the density of CO_2 within the reservoir to be 700 kg/m^3 *Chadwick et al.* [2002] estimated 2.01 MT compared to the known injected mass of 2.35 MT for 1999.

This model assumes that the CO_2 within the reservoir is partitioned between high saturation thin layers and a low saturation volume existing in a diffuse form between the layers. Evidence supporting the existence of diffuse CO_2 is given by *Chadwick et al.* [2004]. They showed that the ratio of velocity pushdown to reflection amplitude is much higher in the central portion of the plume than at its edges, consistent with the presence of diffuse CO_2. *Arts et al.* [2002b] showed that the outer parts of the CO_2 plume obey a thin-bed tuning relationship, whereas the central parts don't, requiring the presence of low saturation CO_2 near the central chimney. The diffuse CO_2 is presumably a consequence of CO_2 percolating upwards from the layers through the overlying shales. However, reservoir flow simulation models indicate that extensive clouds of diffuse CO_2 are difficult to produce physically.

Differences between the estimated CO_2 mass and the real injected mass can be accounted for by a number of different mechanisms. Dissolution of some CO_2 into the formation water is one fundamental process of the injection. Simulations by *Johnson and Nitao* [2003] show that between 15% and 20% of the CO_2 will have dissolved after ten years. Dissolution amounts after three years, however, would have been much smaller. Also, incomplete ability to resolve the pushdown associated with the main chimney causes the mass estimation to be low. Additionally, the diffuse mass was assumed to have a vertically uniform distribution, yielding a minimum value for the CO_2 mass required to fit the data. Non-uniform CO_2 distributions could require more mass. It has been shown [e.g., *Mavko and Mukerji*, 1998] that for fluid filled rock, pore pressures can equilibrate over spatial scales of $L_c \approx \sqrt{kK_{fl}/f\eta}$, where f is the seismic frequency, k is the permeability, η is viscosity, and K_{fl} is the bulk modulus of the fluid. Heterogeneous saturations with length scales greater than L_c are referred to as patchy saturations, and have wave-induced pore pressure gradients that cannot equilibrate. Furthermore, patchy saturations always lead to higher seismic velocities than uniform saturations (saturations with length scales less than L_c). This means that for a given seismic pushdown, more CO_2 mass is required by a patchy saturation than by a uniform saturation. Examples of two velocity versus average CO_2 saturation curves for patchy saturation models are shown in Figure 2.6. For the seismic surveys at Sleipner, L_c is on the order of a few tens of cm, which is much smaller than a seismic wavelength. Therefore, any distribution of CO_2 with length scales on the order of L_c, whether patchy or uniform, would have no observable reflectivity. This makes it impossible to determine the mass of contained CO_2 without first determining the patchiness and density. In fact, two of the three quantities must be known in order to determine the third.

Arts et al. [2002b] estimated the mass within the CO_2 bubble using only the pushdown and the seismically imaged volume for a lower value of CO_2 density. He found simple models that fit the data just as well with densities of 600-650 kg/m^3. Additionally, *Andy Chadwick et al.* [personal communication, 2004] have done studies showing that models can be constructed such that CO_2 with a density of 350 kg/m^3 match the injected mass by varying the distribution and saturation (increasing the patchiness) of the diffuse CO_2.

2.1.5 Refining the density estimate

One of the largest sources of uncertainty in seismic estimates of CO_2 mass comes from uncertainty in the density of CO_2 within the Utsira formation. The density of CO_2 depends on temperature, pressure, and the amount of trace impurities. The carbon dioxide injected at Sleipner contains methane, which tends to lower the density, and BTX (butanes, toluenes, and xylenes), which tend to increase the density. These two effects cancel each other out at Sleipner [*Zweigel et al.*, 2004], meaning the thermodynamics and equation of state (EOS) for pure CO_2 can be used [e.g. *Span and Wagner*, 1996].

The temperature profile through the formation is based on a single downhole measurement of 37 °C at a depth of 1058 m bsl. For a water depth of 80 m and assuming 4.8 °C on the seafloor, this gives a linear temperature gradient of 33 °C/km

[*Lindeberg et al.*, 2000; *Zweigel et al.*, 2004]. Temperatures in the Utsira formation are therefore expected to range from 28 °C at the top of the reservoir to 41 °C at the bottom of the reservoir.

However, this single measurement is subject to an uncertainty of at least 2-5 °C [*Williamson et al.*, 2001]. This is because temperature measurements made in boreholes are costly, and are usually made long before the fluids in the borehole reach equilibrium. This can take several months, since cutting fluids pumped into the borehole during the drilling contaminate the hole, making the temperature of the fluids within the hole cooler than in the surrounding rock. The measurement in the Utsira formation was made at the time of drilling, and although corrections were applied to account for the artificially lowered temperature, a large uncertainty remains.

Near the predicted reservoir temperature and pressure conditions, CO_2 goes through a critical phase transition in which the density changes from 200 kg/m^3 to over 700 kg/m^3 [*Span and Wagner*, 1996] (Figure 2.7). Thus a slightly higher temperature could result in a much lower CO_2 density. In fact, typical geothermal gradients in the area are 35-40 °C/km [e.g., *Glennie*, 1998; *Rider*, 1986], suggesting that the temperature at the measurement location is 42-50 °C. A temperature of 96 °C has been measured below the Utsira formation at a depth of 2385 m bsl [*Ola Eiken*, personal communication, 2004]. Linear interpolation to the seafloor gives a temperature of 45 °C at the Sleipner measurement point (1058 m bsl). This means that the CO_2 could be in a completely low-density state (300-550 kg/m^3). Most of the work

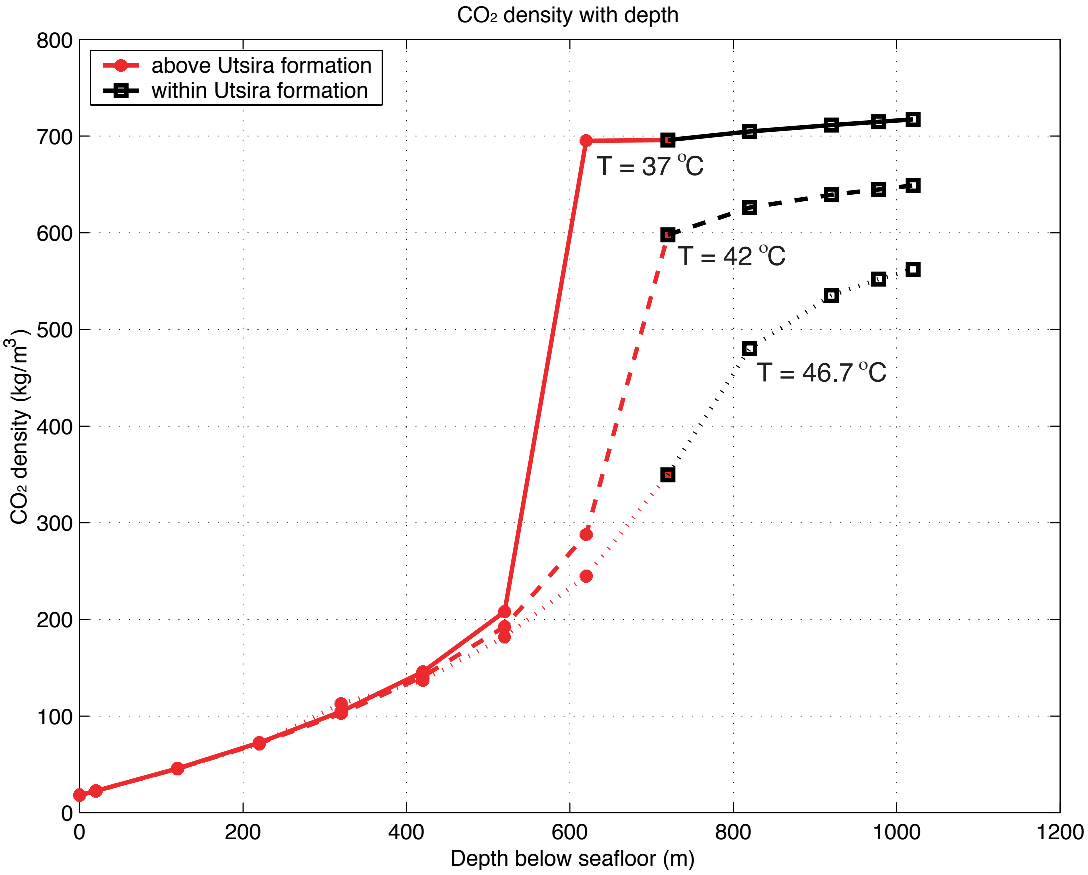

Figure 2.7 CO_2 density versus depth for three possible temperature profiles in the Utsira formation. The CO_2 goes through a critical phase transition and the resulting density is highly dependent on temperature. Thus an uncertainty in temperature of 5-10 °C indicates a corresponding uncertainty in the density of the CO_2.

that has been done in reservoir simulations and in estimating the *in situ* CO_2 mass has assumed that the 37 °C measurement is correct, and that the CO_2 density is 650-700 kg/m^3. However, recent studies indicate that models with lower CO_2 densities can adequately account for the injected mass [*Andy Chadwick et al.*, personal communication, 2004].

One reservoir monitoring technique sensitive to changes in density is time-lapse gravity. As CO_2 is injected into the Utsira sand, it displaces the water from the pore space in the sand, causing an effective density change within the formation. Because the density of CO_2 is less than that of water, the effective density contrast is always negative. Thus, a higher CO_2 density results in a smaller, but still negative, change in the local gravity.

Williamson et al. [2001] completed a feasibility study to determine whether gravity measurements could be used to put constraints on the density of CO_2 within the reservoir. Their model was built by enclosing the seismically imaged CO_2 reflective horizons with a continuous surface and assuming all of the injected CO_2 was enclosed in this volume at a uniform saturation. They computed the gravity signals from both a high and a low density model. The low density model (350 kg/m^3) shows a peak gravity change of -15 μGal/yr and the high density model (700 kg/m^3) shows a peak gravity change of less than -5 μGal/yr.

Shipborne gravimeters typically have an accuracy of 300-1000 μGal, making the estimated gravity anomalies from the CO_2 injection undetectable. However, seafloor gravity measurements made with an ROV carried instrument have been shown to be capable of measurement accuracies of 18 μGal or less [*Sasagawa et al.*, 2003], comparable to land surveys. *Sasagawa et al.* [2003] simultaneously measured depth using relative pressure gauges, with an accuracy of 0.78 cm, leading to an additional uncertainty in time-lapse gravity of about 1.7 μGal. Based on this, *Williamson et al.* [*Williamson et al.*, 2001] recommended using the ROVDOG (Remotely Operated Vehicle deployable Deep Ocean Gravimeter) [*Sasagawa et al.*, 2003] to obtain a time series of seafloor gravity measurements over the CO_2 bubble in order to put constraints on its density within the reservoir.

2.2 2002 gravity and pressure data acquisition

2.2.1 Method

Time-lapse gravity studies have been used onshore for monitoring hydrothermal energy reservoirs [e.g. *Allis and Hunt*, 1986; *Andres and Pedersen*, 1993] and magma chambers on active volcanoes [e.g. *Rymer and Brown*, 1986]. For off-shore reservoir monitoring, the collection of seafloor gravity data is more desirable than sea surface gravity data, primarily because the seafloor instrument is much closer to the source bodies than a sea surface gravimeter, improving the signal-to-noise ratio. Past seafloor gravimeter systems have been lowered from ships [e.g. *Hildebrand et al.*, 1990; *LaCoste*, 1967], however, precise repositioning is required for time dependent work. Gravimeters have also been operated inside manned submersibles resting on the seafloor [*Ballu et al.*, 1998; *Cochran et al.*, 1994; *Evans*, 1996; *Holmes and Johnson*, 1993], but vehicle motion during the measurements has been problematic. Because of these limitations, *Sasagawa et al.* [2003] built a new instrument meant to be deployed with an ROV or a manned submersible (Figure 2.8). This instrument, the ROVDOG, is placed directly on a concrete benchmark resting on the seafloor and is connected to the deployment vehicle by only a loose tether, thereby eliminating all accelerations caused by the ship and ROV. By deploying the instrument with an ROV onto permanent seafloor benchmarks, positioning uncertainties related to site reoccupation are virtually eliminated. Simultaneous pressure measurements with the ROVDOG can be converted to depth for monitoring seafloor deformation. Three separate ROVDOG instruments can be packaged together on a single frame (Figure 2.8a) in order to increase the number of measurements made, thus improving the statistical precision.

Gravity and pressure were measured on the seafloor above the Sleipner CO_2 injection site from the16th to the 21st of August, 2002, on top of 30 concrete benchmarks, which were permanently deployed on the seafloor immediately prior to the survey. Funding for the work came from the U.S. Department of Energy (DOE), SACS, and Statoil. The water depth in the survey area ranges from 80 to 85 m, and seafloor is flat and featureless, covered with fine pelagic sediment.

The survey procedure followed the straightforward but patented method of *Eiken et al.* [2004] which is described by *Sasagawa et al.* [2003]. First, the vessel transited to the first benchmark location and established dynamic positioning using global positioning system (GPS). The ROV was then launched with ROVDOG held in place by the manipulator arm and a mounting bracket. The pilot guided the ROV to the benchmark, locating it with sonar and video cameras. Short baseline acoustic navigation of the ROV usually enabled benchmark location within 5 to 10 m of its expected location.

Upon benchmark location, the pilot maneuvered the ROV into position, placed the ROVDOG on top of the benchmark and released it from the manipulator. The ROVDOG operators then initiated an automatic leveling routine and began the measurement. During the measurement, the ROV sat motionless on the bottom 1-2 m from the benchmark. The only link between the ROV and the sensors during the measurement was a cable, which was weighted to lie on the seafloor, thereby mechanically decoupling the sensors from the ROV. Each observation lasted for about 20 minutes. At the end of the measurement, data logging was terminated and the ROV pilot retrieved the ROVDOG with the manipulator arm. The ship and ROV then began an under-water transit to the next site at ~1.25 m/s (2.4 knots). The ROV and gravimeters remained underwater most of the survey in order to minimize temperature variation. The system was brought onboard once for about two hours to fix a loose connector. The second gravity survey, which will provide the first evidence of a change in gravity due to the CO_2 injection, is scheduled for the summer of 2005.

2.2.2 Benchmarks

Seafloor benchmarks serve as stable platforms to place the instruments in exact registration on the seafloor. The benchmarks are 35 cm tall and are frustum in shape, with a lower diameter of 160 cm and an upper diameter of 80 cm (Figure 2.9). This shape was chosen to minimize disturbance from trawl fishing. Each benchmark has a mass of about 650 kg. Similar benchmarks have been used in sedimented areas by *Segawa and Fujimoto* [1988]. They are quite stable, owing to the temperature stability of the environment. Based on analysis of sediment stability in the central North Sea, the benchmarks are expected to sink less than a few centimeters into the sediments [*Sasagawa et al.*, 2003], with most of this occurring within the first few months of installation. The gravity gradient on the seafloor is approximately 2 μGal/cm,

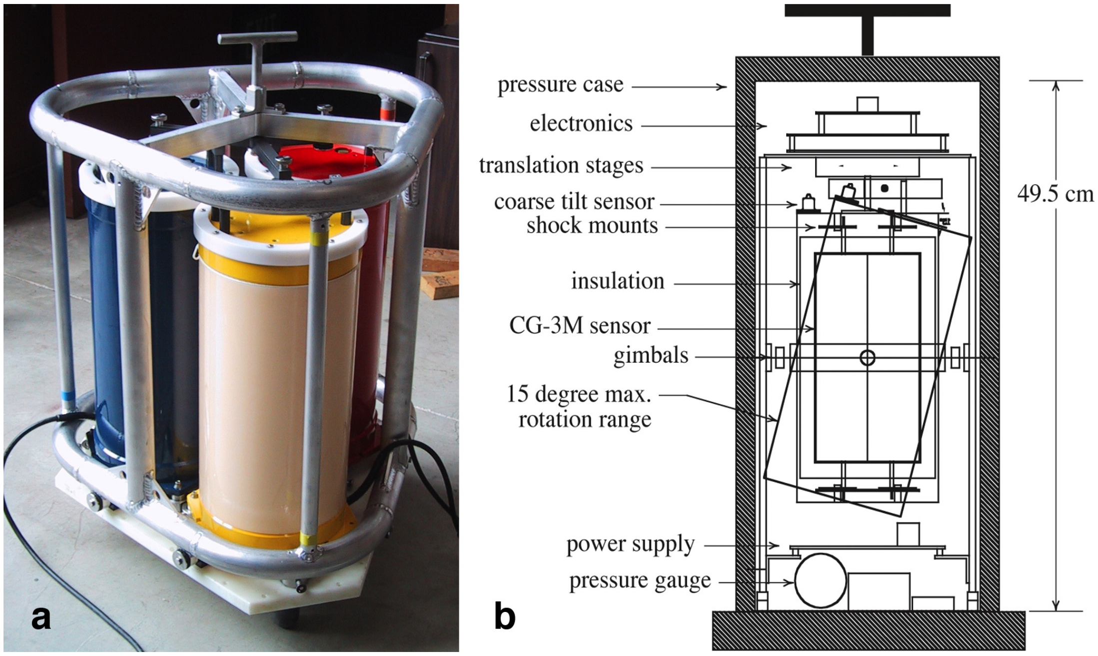

Figure 2.8 a.) Photograph of the ROVDOG instrument package used in the Sliepner gravity survey in 2002. Three instruments are affixed to one frame to increase the number of measurements at each site. b.) Diagram from *Sasagawa et al*. [2003] illustrating the internal schematics of the ROVDOG.

meaning that benchmark settling of a few centimeters could cause a gravity increase of 2-4 μGal.

Twenty of the benchmarks were placed in a 7.3 km long WNW-ESE profile across the injection point (Figure 2.10). The distance between stations increases from about 300 m near the injection point up to 500 m toward the ends. The end points are far from the injection point and are perpendicular to the maximum spreading direction observed from the 1999, 2001, and 2002 seismic surveys. This geometry was chosen to minimize the change in gravity over time on the endpoints, which will serve as temporally stable references in our relative surveys. Another 10 locations span the

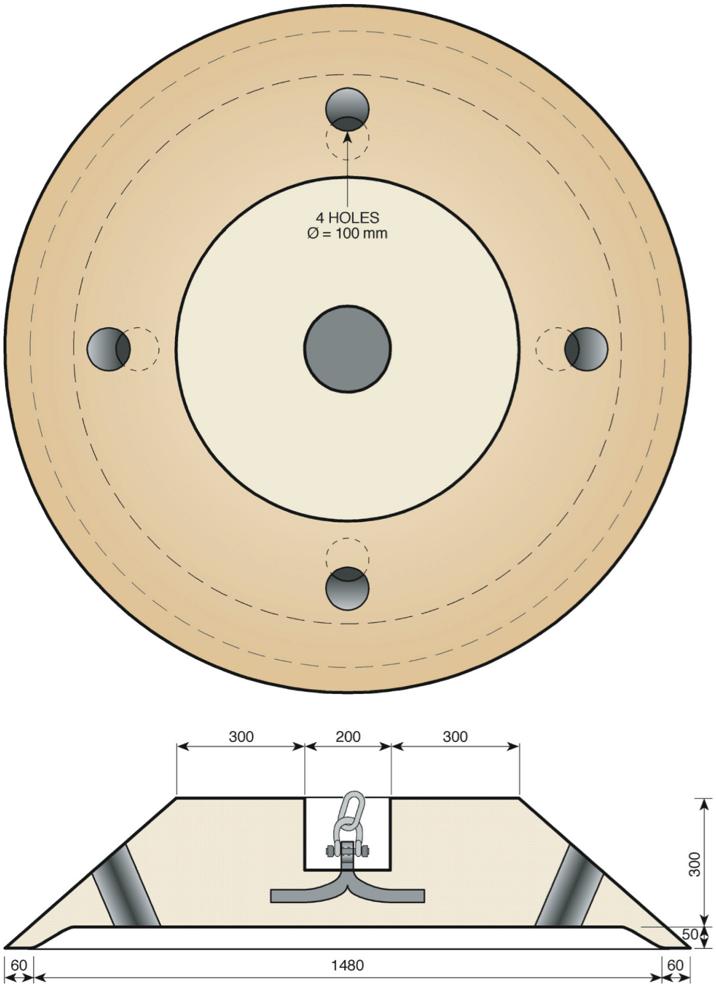

Figure 2.9 Illustration of the concrete frustum shaped benchmarks used at Sleipner to provide stable and precise platforms for time-lapse gravity measurements. Dimensions are given in mm. Diagram provided by Ola Eiken.

orthogonal dimension and cover the extent of the CO_2 accumulation in 2002. The benchmarks were lowered to the seafloor with a wire line and acoustic release hooked onto a small chain, which fell into the central hole after release. The deployment operation lasted 10 hours for all 30 benchmarks, and was done just before surveying, on 16th August 2002.

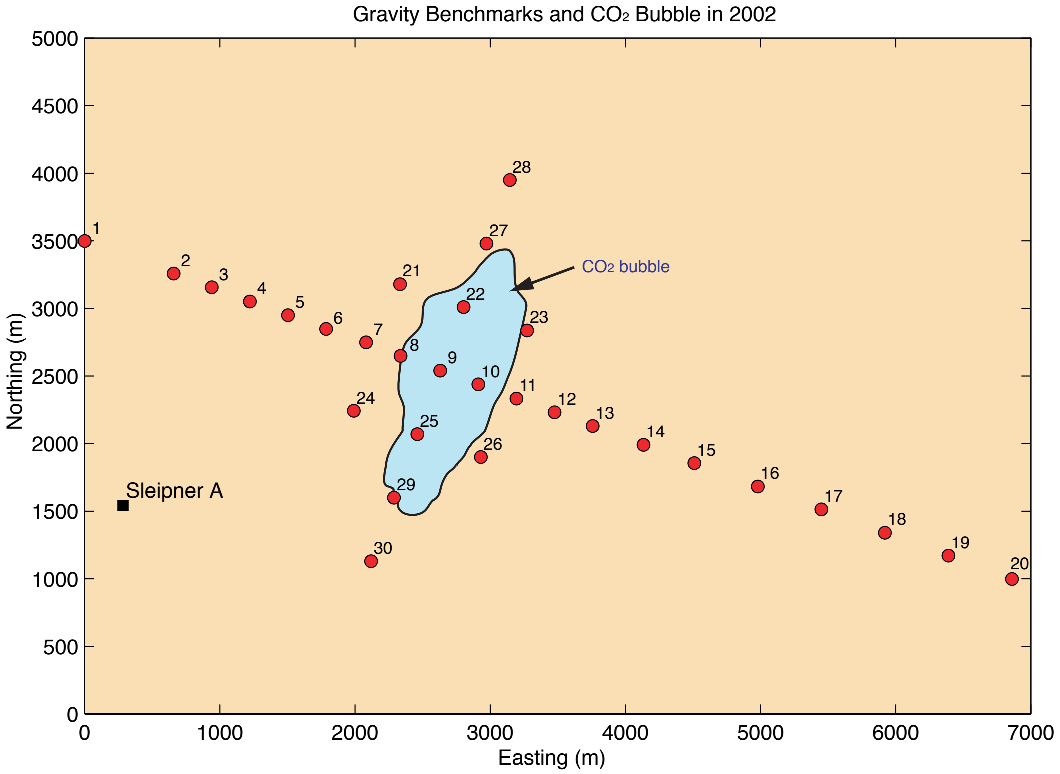

Figure 2.10 This shows the location of the benchmarks over the injected CO_2 bubble. The outline of the CO_2 comes from 2003 seismically imaged horizons. Maximum gravity change is expected to occur on benchmark SP09. SP20 is expected to see almost no gravity change and will serve as the reference for time-lapse monitoring. For the figure, the prefix SP is left off of the benchmark names.

2.2.3 Marine operations

The ship used for the survey was the *Edda Freya*, a supply vessel which has been converted for ROV/Subsea operations (Figure 2.11). It has a length of 87.1 m, breadth of 17.5 m and tonnage of 3476 tons dry weight. The vessel carries a HIROV 3000 Mk II (Figure 2.12), a work class ROV equipped with a 5-function arm and a 7-function manipulator arm. The ROV is launched and recovered with an A-frame on the side of the ship. In addition to differential GPS and the standard navigation system showing the ROV position relative to the ship, the NaviPac navigation software was rented for this work, to secure an effective transit from site to site.

Gravity measurements were carried out in the period from the 16th of August 2002 (Julian day 228) at 18:00 (UTC) until the 20th of August (Julian day 232) at 15:00 hours. 115 measurements were made during this time, at a rate of about 30 per day. Each station was visited at least 3 times, to give adequate control on drift and survey accuracy. Survey loops were made with benchmark SP09 as the central location (Figure 2.10). This site was visited 15 times during the four days for a loop duration of about 7 hours. More details are given in Appendix 3. The sequence of stations within each loop was alternated in order to separate temporally correlated errors from spatially correlated errors. The six stations with largest scatter (based on onboard processing) received a fourth visit, and the easternmost station (SP20), which is likely to be well outside the area of CO_2 influence and hence serve as a reference location for future gravity changes, received five visits. At the end of the survey, five closely spaced locations without benchmarks (22 m, 22 m, 20 m, 44 m and 105 m separation) were measured (named SP31-SP35), to investigate short-wavelength variations in gravity.

Weather was good during benchmark deployment and at the beginning of the survey but increasingly worsened. This can be observed in the noise level (RMS sample scatter) of the gravity time series (Figure 2.13). Significant wave heights were about 3 meters towards the end of the survey.

Figure 2.11 The supply vessel *Edda Freya* was used as the survey ship during the operation.

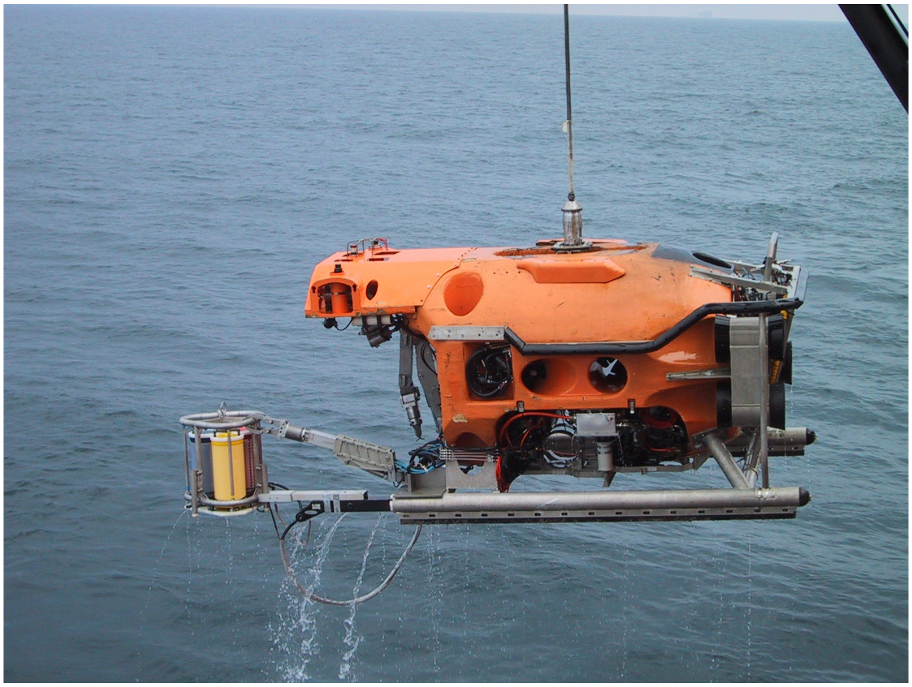

Figure 2.12 HIROV 3000 Mk II ROV used to deploy the ROVDOG meters.

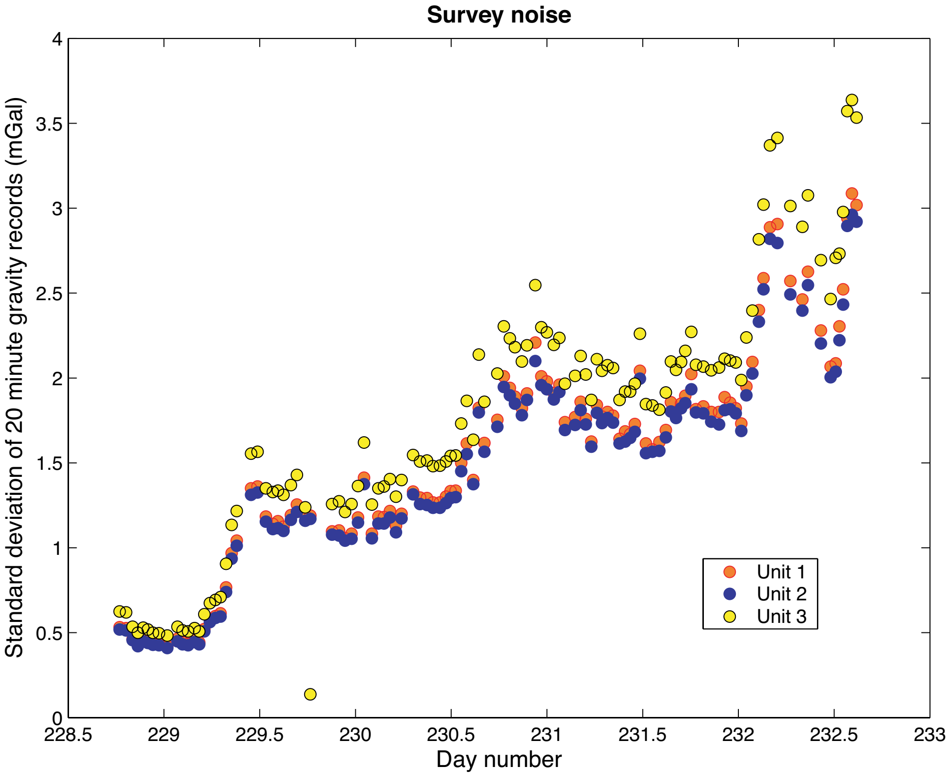

Figure 2.13 As the survey progressed, wind and wave height increased. This is reflected in the RMS scatter of 20 minute gravity records.

Power failure on Unit 3 caused a halt in the operation for repair after 31 measurements had been made. The instrument was brought on deck, the pressure caseopened, a loose connector was repaired and it was put in the water again within two hours. The instrument worked well for the rest of the survey.

2.2.4 Reference environmental data

To aid with tide corrections, pressure was continuously recorded over the duration of the survey using portable seafloor instruments (made by the Norwegian company Aanderaa) located at the center of the survey area (at benchmark SP09). Altogether, four reference gauges were deployed (Table 2.1), strapped together in pairs. Figure 2.14a shows the mean pressure from the two WLR7 (Water Level Recorder) gauges, and Figure 2.14b shows the difference between each sensor pair. The two WLR7 pressure gauges show good agreement, but the WLR8 gauges deviated by about 20% from each other. The WLR7 gauges are rated to a depth of 340 m and the WLR8 gauges are rated to 1370 meters. The larger dynamic range of the WLR8 gauges leads to a decrease in precision. Therefore, the data from the WLR8 gauges were not used in further analysis. The two WLR7 gauges agree to within 36 Pa (standard deviation), corresponding to a depth uncertainty of 3.6 mm.

A CTD attached to the ROV measured density profiles through the water column at every launch and recovery, for a total of four measurements, all at benchmark SP09. The last measurement was obtained after the ROV had been in the water for some time, therefore, this value may be less susceptible to transient temperature effects, as the sensor had time to equilibrate to seawater temperature (Figure 2.15).

Table 2.1 Reference pressure gauge information.

Gauge Type	WLR 7	WLR 7	WLR 8 (1497)	WLR 8 (1687)
Owner	Statoil	Sintef	Geoconsult	Geoconsult
Depth range (m)	0-340	0-290	0-1370	0-1370
Deployment span in day number	228.22 to 232.72	228.22 to 232.72	228.22 to 232.72	228.22 to 232.72
Sampling interval	2 min.	2 min.	5 min.	5 min.

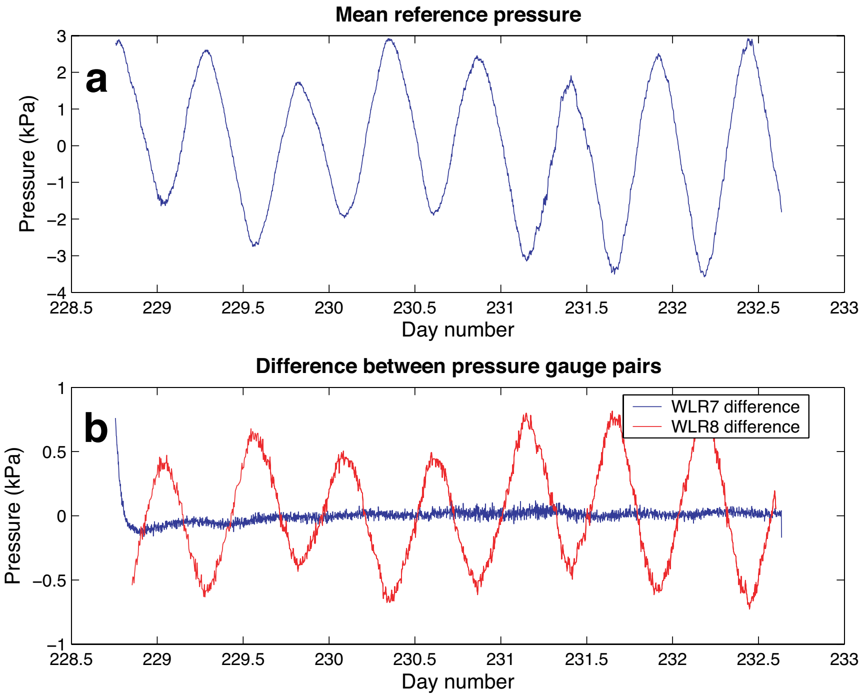

Mean reference pressure

Difference between pressure gauge pairs

Figure 2.14 Plots showing reference pressure data used for tide corrections. a.) This plot shows the average of the two WLR7 gauges. This was used to correct the pressure gauges on ROVDOG. b.) Plot showing the difference between gauge pairs deployed at benchmark SP09. The data from the WLR8 gauges were not used because of the large disagreement seen here. Note that 1 kPa corresponds to approximately a 10 cm change in water height.

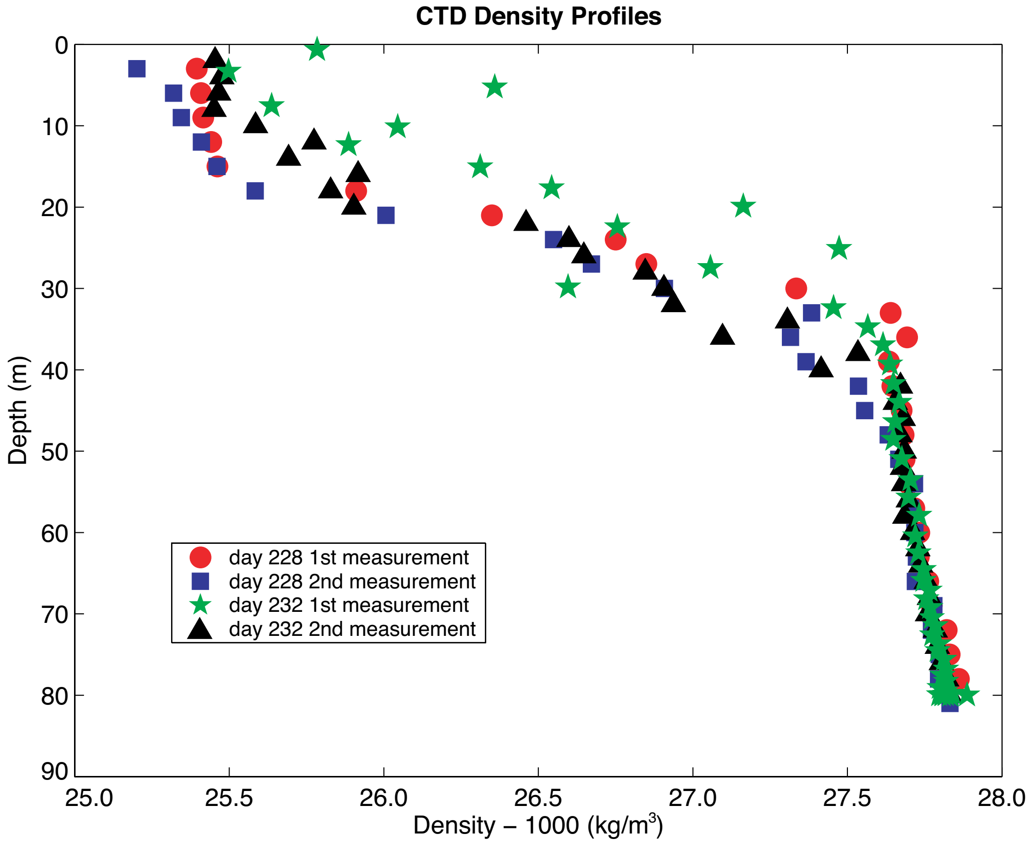

Figure 2.15 Plot showing the change in seawater density with depth from four CTD casts made at Sleipner. The legend gives the measurements in chronological order, with the final CTD measurement as the ROV was being recovered to the ship.

2.3 Data Processing

Much of the gravity and pressure data processing was done onboard the ship during the survey for quality control purposes. Statoil provided Torkjell Stenvold and Håvard Alnes as data processors. After a measurement was made on a benchmark, the raw data were sent to a separate processing computer, where it was quickly run through an SIO in-house Matlab processing routine to examine data quality. This code converts the raw data in periods to physical units and applies corrections to the gravity data for tilt and temperature. After verifying the data quality, transit to the next site began. The resulting processed data were then put into a spreadsheet where drift and tide corrections were made. Instrument drift was computed based on repeat site measurements.

2.3.1 Pressure

The ROVDOG raw pressure data were initially processed on the ship using theoretical tides. However, at the end of the survey the WLR reference pressure gauges deployed at benchmark SP09 were recovered. These provide a direct measurement of effects of the ocean tide, changes in air pressure, changing wind conditions, and any other time-varying environmental pressure signal that might contaminate the ROVDOG data. Therefore, the ROVDOG raw pressure data were reprocessed on shore using the WLR data to make corrections rather than theoretical models. The averages of each 20 minute time series were then computed and compared for the three units. Short-term gauge drift was calculated by fitting a line to all repeat measurements. Drift corrections were then made by subtracting the calculated drift from all measurements. Pressure was then converted to depth using a model with a constant water density of 1028 kg/m^3 (the average water density determined from the CTD measurements), gravity of 9.82 m/s^2, and air pressure of 101 kPa. The resulting absolute depths vary from 79.5 m to 83.6 m. More details on the processing of the pressure data can be found in *Stenvold et al.* [2005].

The position of the pressure gauges, near the bottom of the pressure case, is about 20 cm above the top of the benchmark, which again is 30 cm above the seafloor. Approximately one half meter could therefore be added to get seafloor depths. The uncertainty in absolute depth is probably well above 10 cm. However, for monitoring relative changes, depths are referenced to locations outside the area of gas injection, such as station SP20. The repeatability of the measurements gives the best indication of the uncertainty in the relative depth values. Figure 2.16 shows the residuals after the mean value of a station is subtracted from each measurement at that station. The standard deviation is 0.37 cm, which we adopt as the uncertainty in the relative depth estimates. Apart from three outliers, all values repeat to within ± 0.8 cm. The small depth range of 4.1 m contributes significantly to the repeatability, as gauge precision scales with the range of operation.

2.3.2 Gravity

The quality of the relative gravity data is also evident in the repeatability of the measurements. Quality control was thus done by comparing repeated observations in three ways: 1. Multiple measurements made at each benchmark were compared. 2. Agreement among the three meters was examined for each measurement. 3. Stability

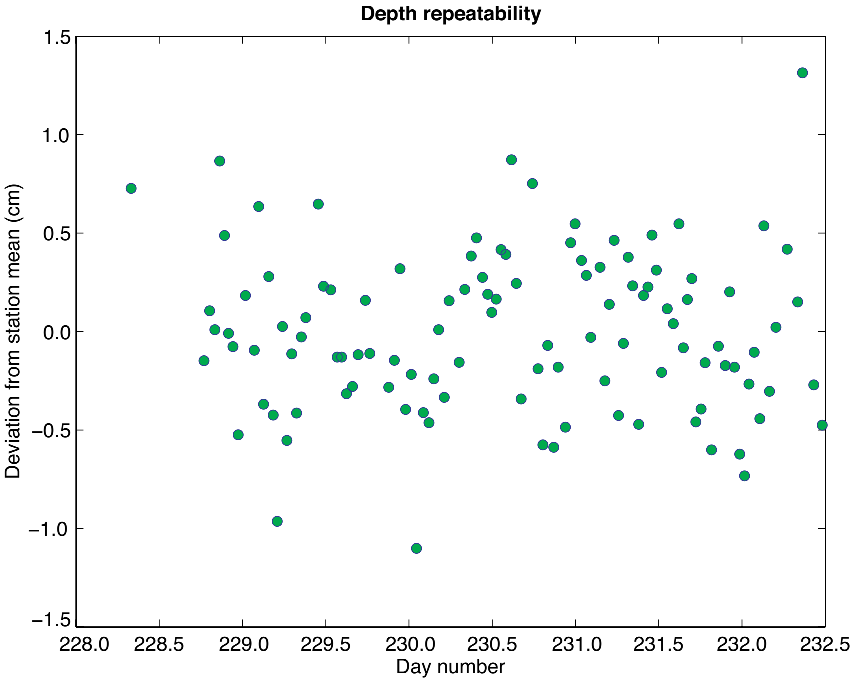

Figure 2.16 Plot showing the scatter of repeat pressure measurements after the mean for each station has been subtracted. The standard deviation of the data points is 0.37 cm.

of each measurement was examined by comparing the first and second half of each 20 minute gravity record.

For each 20 minute long gravity record, noisy samples were eliminated and the time range of good data selected, prior to calculating the average. Figure 2.17 shows an example of a 20-minute gravity time series for all three ROVDOG gravimeters, collected on August 8, 2002, at site SP12. The data were sampled at 1 Hz. Narrow-band seafloor accelerations (mostly at 2-3 s period) originate as an interference phenomenon between ocean waves from different directions [*Babcock et al.*, 1994; *Longuet-Higgins*, 1950]. Noise amplitudes in this band were up to 3.5 mGal near the end of the survey (Figure 2.18), but due to the periodic nature a 20 minute average effectively reduced the noise to acceptable levels. During transit from site to site, the ROVDOG package is subject to ROV motions and vibrations. When a meter is tilted by more than about five degrees, the quartz spring of the gravimeter becomes shorter. During the time the spring has been shortened, visco-elastic deformation of the spring takes place and some time is required for the spring to "recover" from this altered state. This behavior, called the recovery, can last up to 10 minutes (see Appendix 1 for more details). The size of such effects is indicated by comparing the mean of the first half and second half of a 20 minutes record (Figure 2.19). The recovery phenomenon is smallest on Unit 3, and for some records only the second half of Unit 1 was used.

Gravity values were corrected for solid earth tides and the ocean loading term by using the world-wide model SPOTL [*Agnew*, 1996]. The varying gravity attraction from water tide was compensated using sea level height estimates based on reference pressures and the average water density based on CTD measurements.

Instrument drift was estimated individually for each gravity meter by least squares fitting all repeat measurements to a polynomial in time. A change in drift rate occurred for Unit 2 and Unit 3 at the time when Unit 3 was recovered to the surface to replace a faulty connector (Julian day 229.7). Therefore, separate drift polynomials are used before and after the incident (Table 2.2) for Units 2 and 3. Laboratory tests have indicated that instrument drift is sensitive to changes in external temperature [*Glenn Sasagawa*, personal communication].

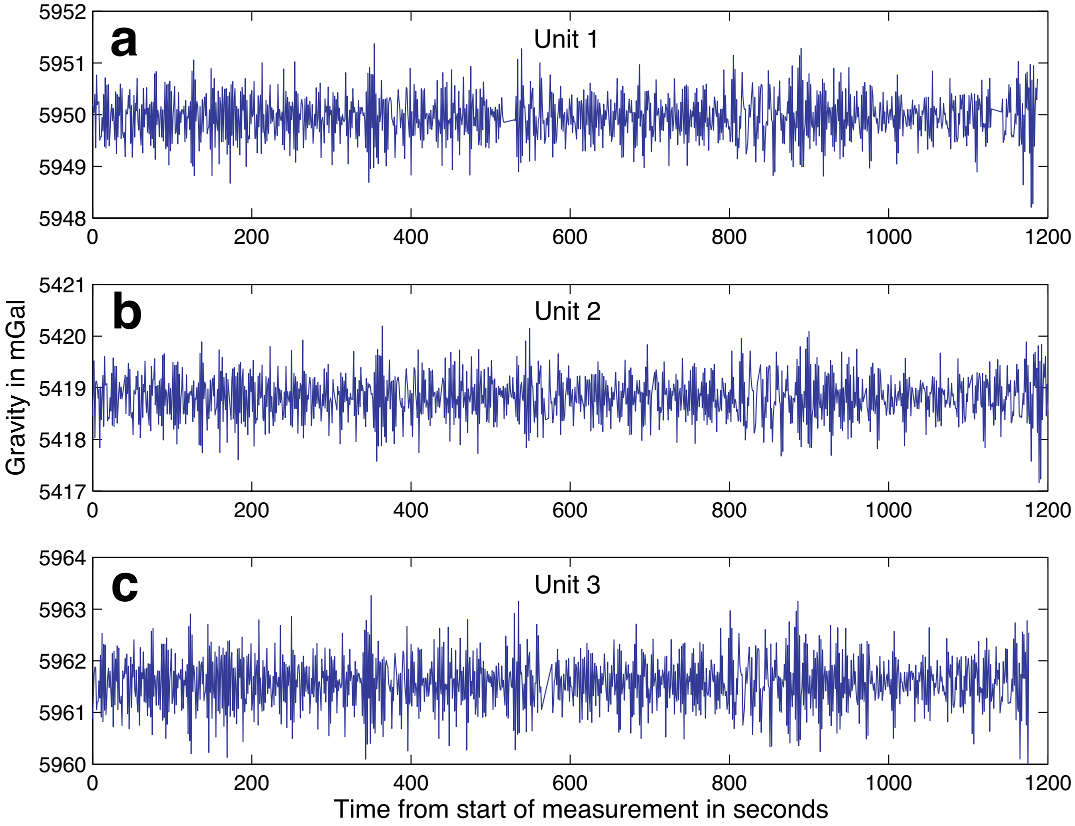

Figure 2.17 Examples of 20-minute gravity time series obtained on August 8, 2002, at site SP12 for a.) Unit 1, b.) Unit 2, and c.) Unit 3. The data have been corrected for tilt, temperature, and tides.

Table 2.2 Gravimeter drift rates; the values for Units 2 and 3 changed mid-survey when the instruments were recovered to the surface to replace a faulty connector (at decimal day 229.7).

	Linear term [μGal/day]		**2nd Order term [μGal/day^2]**		**Split time (day)**
	1st Half	2nd Half	1st Half	2nd Half	
Unit 1	556.5		-1.7		
Unit 2	362.8	442.4	0	-0.1	229.7
Unit 3	177.9	192.7	-30.6	0.6	229.8

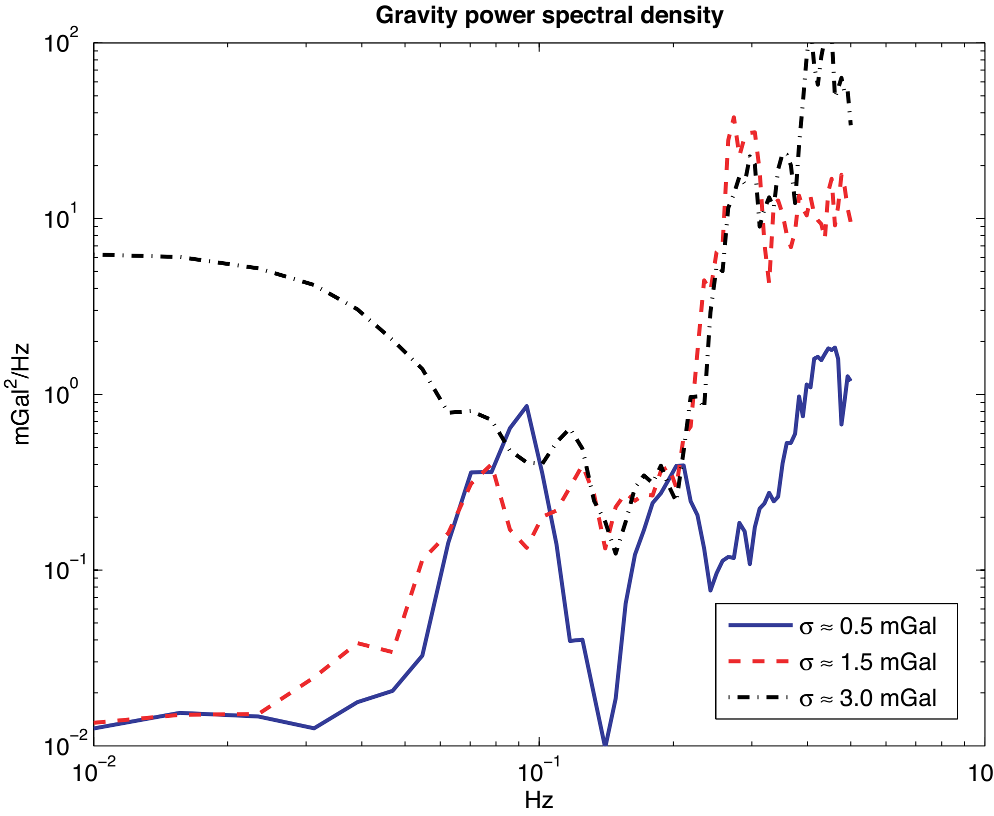

Figure 2.18 Plot showing the power spectrum for three 20 minute gravity records for Unit 3 at different noise conditions (shown in Figure 2.13). The sampling frequency of the gravimeters was 1 Hz.

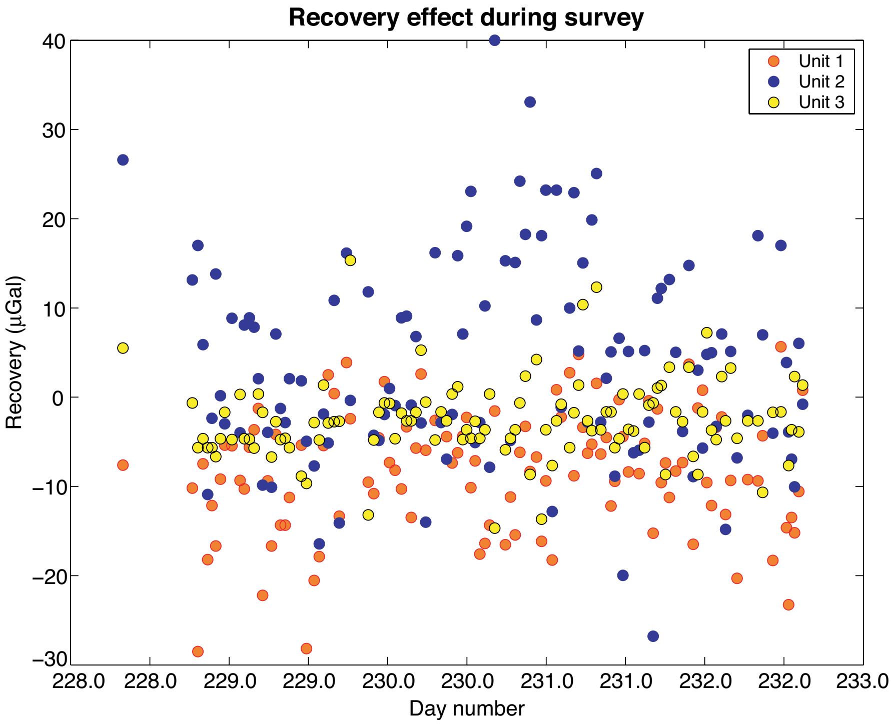

Figure 2.19 Plot showing the recovery effect for each of the three ROVDOG gravimeters. The plot shows the mean of the first half minus the mean of the second half of each 20 minute gravity record.

The drift correction can be quality controlled by plotting unit differences as a function of survey time (Figure 2.20). There are no apparent trends left in the plot, which suggests the drift has been removed (drift values are given in Table 2.2).

The repeatability of the units are 8.8 µGal for Unit 1, 9.9 µGal for Unit 2, and 4.7 µGal for Unit 3. Because of the much better performance of Unit 3, it was heavily weighted in the average calculation. After weights of 0.396, 0.264, and 2.261 were given to Units 1, 2, and 3, respectively, the repeatability is 4.3 µGal (Figure 2.21).

For time-lapse changes, additional uncertainty is related to determining the reference zero-level, by using stations outside the area of influence from the gas injection. The southeastern most station (SP20) has with its five visits a standard deviation of 1.9 μGal, and if more stations are used for defining the reference zero-level, this uncertainty will be further reduced. This error will add to all stations.

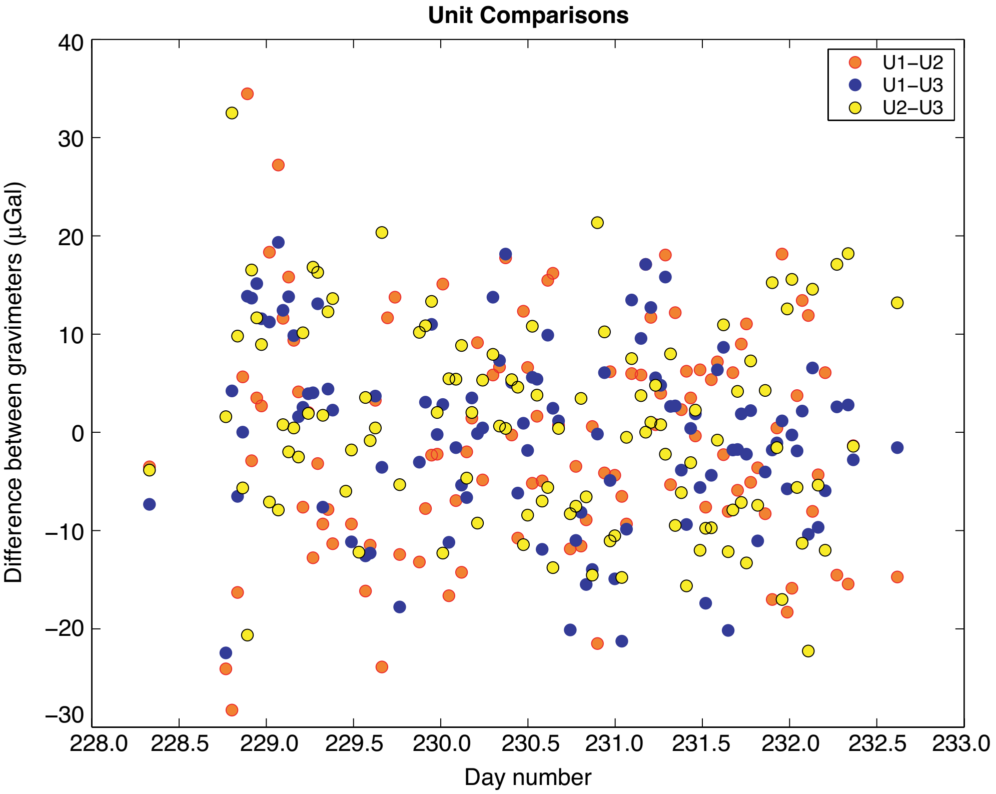

Figure 2.20 Plot showing the differences among the three ROVDOG gravimeters at each site. No apparent trend shows up in the plot, indicating that the drift correction is good.

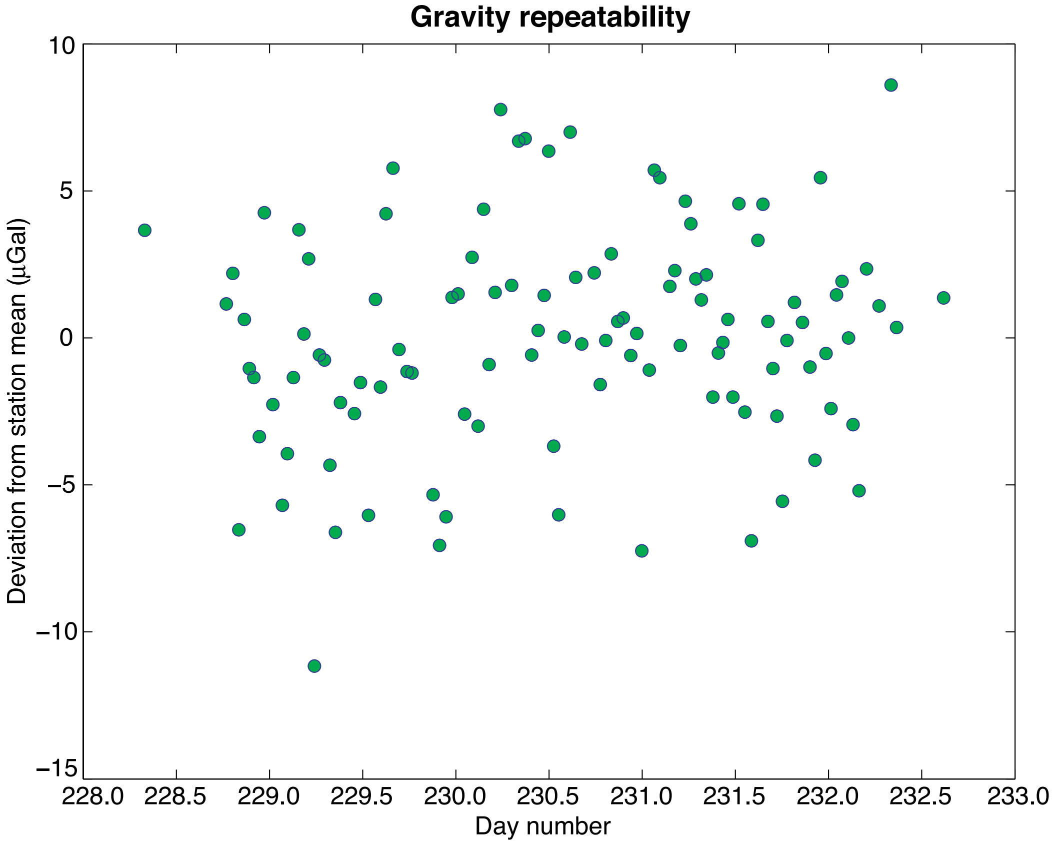

Figure 2.21 Plot showing the scatter of repeated gravity measurements after the mean of each station has been subtracted from each measurement. The standard deviation of the results (4.3 μGal) indicates the precision of the gravity values for the stations.

2.3.3 Discussion

The baseline gravity and pressure survey of the Sleipner site was a great success. There were no major problems with the weather, ship, or instruments and the quality of the data exceeded our expectations. This was vital for establishing confidence that the technique is viable, as well as providing a high quality baseline upon which subsequent interpretation will depend. A second survey is planned for the summer of 2005, which will allow the gravity signal to accumulate for a three-year time period.

In the rest of Chapter 2 the focus of the dissertation shifts from instrumentation, data acquisition, and data reduction to modeling time-lapse gravity and pressure changes due to various scenarios of CO_2 flow. This modeling will provide insight on the size of expected signals as well as provide a foundation for interpreting future time-lapse results.

2.4 Modeling surface deformation

Time-lapse seawater pressure measurements made with the ROVDOG on seafloor benchmarks can be converted to seafloor depth and used to monitor deformation of the seafloor. This is important for two reasons: 1. Gravity is sensitive to vertical height changes; measured changes in seafloor depth can allow us to correct the measured gravity for this effect. 2. Measured surface deformation could provide an independent way to put constraints on the density and mass of the sequestered CO_2.

Mechanical modeling of the CO_2 bubble to predict seafloor deformation was done using two techniques that place upper and lower bounds on the expected uplift due to CO_2 injection. The first method approximates the CO_2 within the reservoir as a horizontal penny shaped pressurized crack with a radius of 1500 m. This approximation is a reasonable one, considering the CO_2 bubble is located at a depth of about 800 m, has a maximum thickness of approximately 200 m, and has a horizontal extent of 1000 to 2000 m (Figure 2.10). Calculations for this were based on a semi-analytical solution from *Fialko et al*. [2001]. Matlab code for this calculation was provided by Yuri Fialko. The shear modulus was taken to be that of shale, $\mu = 0.14 \times 10^{11}$ Pa, and Poisson's ratio ν was assumed to be 1/4. The pressure within the crack was taken as the buoyancy force of the total injected amount of CO_2 distributed over a circle of radius 1500 m. The buoyancy force was calculated using Archimedes Principle, which states that the buoyancy force is equal to the weight of the mass that is displaced; thus, the pressure depends only the density of CO_2 (ρ_{CO_2}), the total mass of the injected CO_2 (M_{CO_2}), and the area, A, over which the force acts (taken to be a circle with a radius of 1500 m in this case).

$$P = \frac{F}{A} = \frac{\Delta\rho M_{CO_2} g}{\rho_{CO_2} A} \qquad 2.4.1$$

In equation 2.4.1 $\Delta\rho$ is the water density minus the CO_2 density and g is the acceleration of gravity.

The uplift at the seafloor was calculated for three CO_2 densities, ρ_{co_2} = 700 kg/m^3, ρ_{co_2} = 550 kg/m^3, and ρ_{co_2} = 350 kg/m^3. The maximum uplift rate comes from the low-density case and is 0.006 mm/year. Over the three-year span between surveys, this amounts to about 0.02 mm of uplift, which is below the resolution of our pressure measurements. For the high-density case the maximum uplift is 0.0015 mm/yr. These results are given in Table 2.3.

A lower bound on the deformation was estimated by treating the seismically imaged CO_2 layers as a collection of distributed point inflations sources, with each grid point in each seismic layer representing a point inflation source, which can be modeled by the following function:

$$\Delta z(x) = \frac{3R^3\Delta P}{4\mu}\frac{d}{(d^2 + x^2)^{3/2}} \qquad 2.4.2$$

x is the radial distance from the uplift center along the surface, μ is the shear modulus of the elastic half-space, R is the radius of the spherical pressure source with a pressure change of ΔP, and d is the depth of the source [*Mogi*, 1958]. Equation 2.4.2 assumes that Poisson's ratio ν is equal to 1/4 and is valid only in the point source approximation, when $R/d << 1$. The pressure of each point inflation source (ΔP) is calculated from the buoyancy force, which is determined individually for each grid point from equation 2.4.1. The CO_2 mass at each grid point is calculated using the empirical capillary pressure – saturation relationship [*Chadwick et al.*, 2004] given in equation 2.1.5. This is described in more detail in section 2.5.2. The area, A, for each grid point is $A = dx \cdot dy$, where dx and dy are the horizontal grid spacings ($dx = dy = 12.5$ m). The shear modulus was taken to be that of shale, $\mu = 0.14 \times 10^{11}$ Pa. The inflation is then computed by summing the results from each individual point source. This model gives an estimate of the minimum deformation, since it assumes that the CO_2 that is not accounted for in the seismic layers does not contribute to the buoyancy force. This would be the case if, for example, a large amount of CO_2 dissolves in the brine or is captured by mineralization within the rock matrix. In fact, only 31% of the mass was accounted for in the low density scenario for 1999 and 65% of the mass was accounted for in the high density scenario for 1999. The results for 2001 are similar, and are given in Table 2.3. The results of this modeling show maximum uplift of 3×10^{-4} mm/yr for the low-density case and 1.5×10^{-4} mm/yr for the high-density case. This amount of deformation is far below our capabilities to resolve.

Table 2.3 Summary of modeling results for seismic horizon models, for both gravity and deformation. The magnitude of the maximum signals are given.

Year	**1999**	**1999**	**1999**	**2001**	**2001**	**2001**
CO_2 density (kg/m^3)	350	550	700	350	550	700
Total injected mass (MT)	2.35	2.35	2.35	4.26	4.26	4.26
Horizon mass (MT)	0.82	1.28	1.56	1.52	2.25	2.73
Horizon g (μGal)	13.4	8.9	5.9	21.8	14.6	9.7
Diffuse mass (MT)	0.10	0.15	0.38	0.18	0.28	0.75
Diffuse g (μGal)	1.7	1.2	1.6	2.9	2.1	3.0
Total g (μGal)	15.1	10.1	7.5	24.7	16.7	12.7
Total mass (MT)	0.97	1.43	1.94	1.70	2.53	3.49
% of total mass	41.12	60.94	82.75	39.88	59.36	81.85
Uz (mm) from distributed point mass	0.0007	0.0005	0.0003	0.0013	0.0009	0.0006
Uz (mm) from penny shaped crack	0.0072	0.0032	0.0017	0.0131	0.0059	0.0032

2.5 Modeling gravity change scenarios

The time-lapse gravity signal was estimated from two types of models. The first type uses the seismically imaged CO_2 horizons and velocity pushdown for 1999 and 2001 (Figure 2.22). The second type of model was based on reservoir simulation models done by SINTEF (Figure 2.23). The seismic data provide the only way, currently, to measure *in situ* CO_2 mass at Sleipner. However, there are discrepancies between the reservoir characteristics that seem to be required by the seismic data and the physics of the reservoir flow models. If geologic sequestration of CO_2 is to become a widely used method for carbon capture, the behavior of CO_2 within reservoirs such as the Utsira formation must be well understood. Part of this is simply in understanding the physical characteristics, such as temperature and density, of CO_2 within the reservoir. The primary goal of this study is to put constraints on CO_2

density and temperature within the reservoir. A secondary goal is to provide an independent technique for quantifying the CO_2 mass within the reservoir.

2.5.1 3-D Gravity modeling code

After looking at commercially available 3-D gravity modeling software, we determined that to accomplish the objectives of this project, we needed to write our own modeling software. We were guided by the need to calculate gravity for an arbitrary shape with a horizontally and vertically varying density. The software needed to be capable of importing regularly spaced 3-D saturation grids from reservoir simulation models, as well as irregularly spaced horizon grids from seismic data. We also needed to be able to build 3-D volumes enclosing the seismically imaged horizons, and compute from them gravity, total volume and mass, and seismic velocity pushdown.

In general, the vertical component of gravity is given by the following equation:

$$g = -G\int_V \frac{\rho z}{r^3} dV \qquad 2.5.1$$

G is the gravitational constant, ρ and z are the density and depth of the body, and r is the distance from the body to the observation point. There are a number of ways to calculate gravity from three-dimensional bodies using equation 2.5.1. These include the stacking of right rectangular prisms [*Nagy*, 1966; *Plouff*, 1976; *Sorokin*, 1951], the stacking of polygonal prisms or laminas [*Plouff*, 1976; *Talwani and Ewing*, 1960], formation of polyhedron [*Götze and Lahmeyer*, 1988; *Holstein and Ketteridge*, 1996; *Okabe*, 1979; *Pohánka*, 1988], and fast Fourier transform techniques [*Parker*, 1973;

Parker, 1995; *Parker*, 1996]. Polygonal prisms require a horizontally uniform density. Formation of a polyhedral body from a three-dimensional grid is quite difficult and the gravity calculation technique requires a uniform density within the body. Multiple bodies could be constructed, but for rapidly varying density this becomes tedious and time consuming. Fast Fourier techniques work well for terrain, but complicated three-dimensional bodies are more difficult to deal with. Therefore, we chose two possible methods for our three-dimensional gravity modeling software: building the mass out of a collection of either cuboids or point masses. These can be easily stacked together to construct complicated three-dimensional bodies, provided that the block sizes are small enough. The gravitational attraction from a cuboid can be calculated analytically. Several researchers have derived the solution in slightly different ways. We use the derivation of *Plouff* [1976]. The resulting gravity due to a single cuboid is as follows:

$$g_z = G\rho \sum_{i=1}^{2}\sum_{j=1}^{2}\sum_{k=1}^{2}\mu_{ijk}\left[z_k \arctan\frac{x_i y_i}{z_k R_{ijk}} - x_i \log(R_{ijk} + y_i) - y_j \log(R_{ijk} + x_i)\right], \qquad 2.5.2$$

where

$$R_{ijk} = \sqrt{x_i^2 + y_j^2 + z_k^2},$$

$$\mu_{ijk} = (-1)^i(-1)^j(-1)^k .$$

G is the gravitational constant, ρ is the density of the cuboid, and x, y, z are coordinates for the cuboid vertices with respect to the observer. The use of arctangents rather than arcsines as in the derivation of *Nagy* [1966] was chosen because with arcsines the block directly below the observation point must be split into four smaller cuboids, otherwise there are singularities in the calculation. With a large number of observation points, this becomes cumbersome. As it is, the calculation from 2.5.2 is still computationally intensive, as it requires the calculation of 24 terms involving arctangents and logarithms.

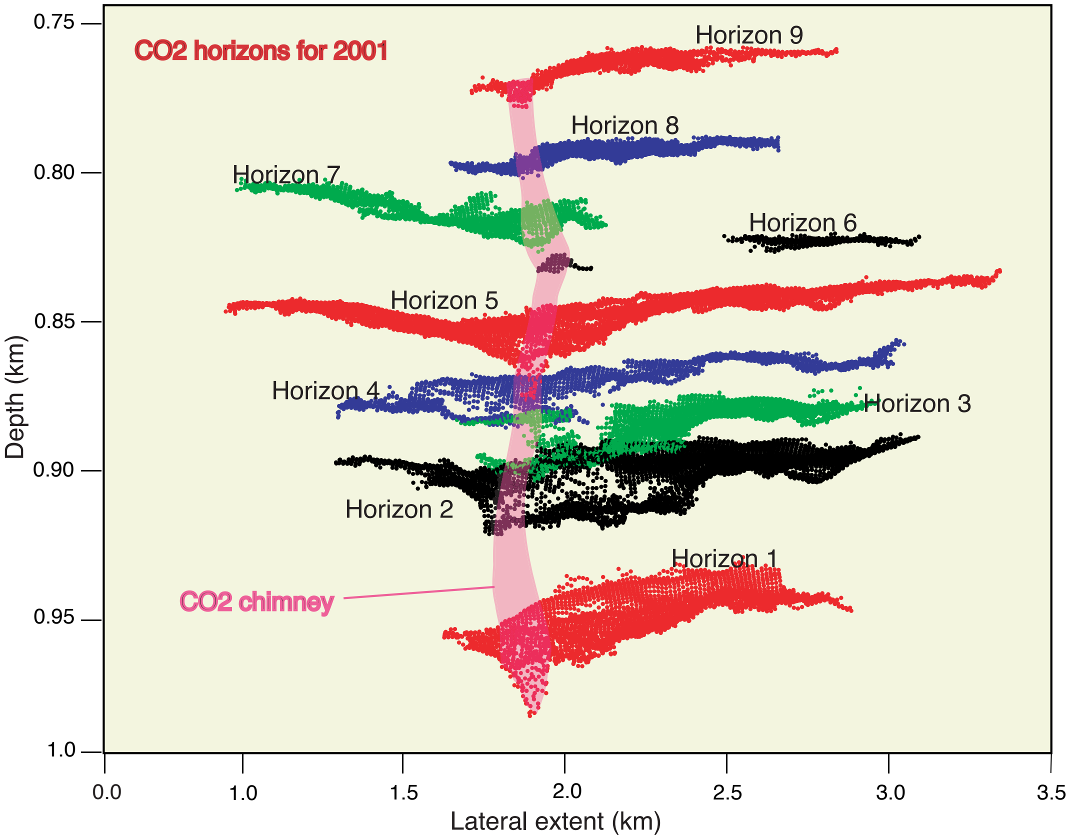

Figure 2.22 Diagram illustrating the model made from the seismic horizons, which are labeled 1-9. The chimney is drawn in to highlight the areas of large pushdown seen in the seismic data.

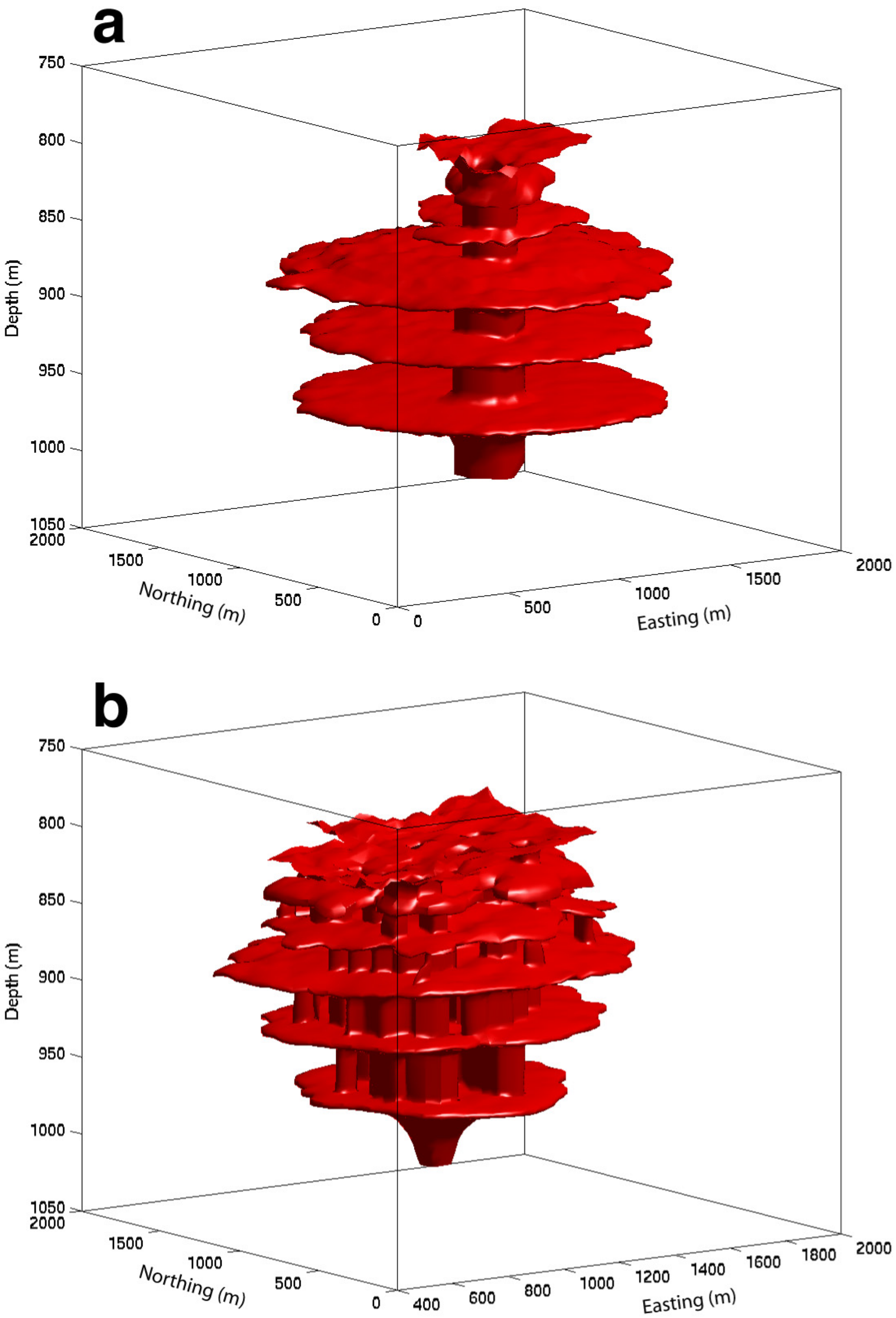

Figure 2.23 Plots showing the reservoir simulation models. a.) The central chimney model, Model I. b.) The random holes model, Models IIa and IIb.

The point mass approximation speeds up the calculation dramatically. The formulation for calculating the gravitational attraction of a point mass is as follows:

$$g_z = \frac{GM}{r^2}\cos\theta = \frac{GMz}{r^3}, \qquad 2.5.3$$

which is a much faster calculation. (Note: in the above equation, M is the mass of the point mass, r is the distance from the point mass to the observer, z is the vertical height above the point mass, and θ is the angle shown in Figure 2.24.) Using point masses results in computation times that are less than 1/6 of computation times using the cuboid code. However, this formulation introduces errors into the calculation because the mass in each cubical element is treated as if it were concentrated at a point in the center. It can be shown that these errors fall off as $e^{-2\pi z/\lambda}$, where z is the distance above the mass and λ is the horizontal grid spacing. For the seismic horizons $z \approx 700$ m and $\lambda \approx 12.5$ m, making the error fall of by a factor of about 1.5×10^{-153}. For the reservoir simulation models $z \approx 700$ m and $\lambda \approx 35$ m, making the error fall of by a factor of about 2.7×10^{-55}. Therefore, there is very little loss of precision in calculating the gravity from reservoir simulation models using the point mass approximation.

To test this, both methods were used to compute the vertical component of the gravitational attraction of a mass in the shape of a thin sheet and a mass in the shape of a frustum of a cone. For the case of a thin sheet, if the sheet is made large enough, it approximates an infinite sheet. The analytic solution for an infinite sheet of mass is $g = 2\pi G\rho h$, where h is the thickness of the sheet. This was compared to the values

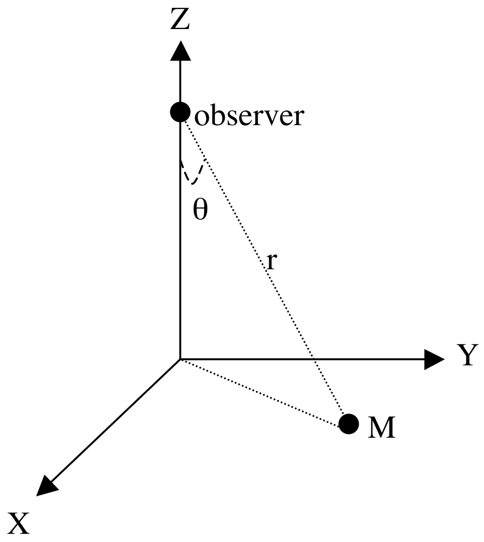

Figure 2.24 The coordinate system used for the gravity calculations.

obtained using cuboids and point masses. As expected, the cuboid code yielded results that duplicated the analytical solution when the horizontal extent of the sheet was made large enough. The point mass code also yielded results close to the analytic solution, however large discrepancies were seen whenever the observation point was close to the surface. (In this case, close to the surface means $z/\lambda < 1$.)

Additional testing was done comparing the two codes to the analytic solution of the gravitational attraction of a frustum,

$$g_z = 2\pi G\rho h[1 - \cos\theta] \tag{2.5.4}$$

where h is the thickness of the frustum and θ is the maximum angle shown in Figure 2.24. This analytic solution is valid only at the apex of the frustum where $z = r\tan\theta$, if r is the radius of the frustum base (Figure 2.25). This geometry provides a way to look at a complex shape at a point arbitrarily far from the surface (depending on the geometry chosen). Figure 2.26a shows the actual frustum shape overlaying the same frustum composed of cuboids. Figure 2.26b shows the same with point masses. As the grid size decreases, the results of each code approach the analytic solution (Figure 2.27) at the same rate. (Note: The geometry was chosen so that the size of the frustum and the height of the observation points are similar to the situation we have at Sleipner.)

The computer floating point precision influences the numerical calculation of analytical formulas. It has been noted by *Holstein and Ketteridge* [1996] and Li and *Chouteau* [1998] that analytical formula for the gravity anomaly of a polyhedral body or a right rectangular prism are subject to numerical error that increases with distance from the source, while at the same time the anomaly decreases. This leads to a limited range of target distances in which the formulas are operational, beyond which the calculations are dominated by rounding error. *Holstein and Ketteridge* defined λ as the typical dimension of the source, δ as the typical distance from an observation point, and the ratio $\gamma = \lambda/\delta$ as the target body aspect ratio. The floating point precision is called ε. Typical values for ε are 10^{-7} for single precision and 10^{-16} for double precision. *Holstein and Ketteridge* [1996] found that to minimize numerical error, an aspect ratio of $\gamma >> \varepsilon^{1/4}$ should be maintained for the calculation of a right rectangular prism. Our code uses double precision (the default for Matlab), so $\varepsilon^{1/4} = 10^{-4}$. Typical source dimensions are λ = 12.5 m for both the gridded data from the seismic horizons and from the Sintef reservoir flow models. The depth of the CO_2 within the Utsira sand ranges from 1020 m to 720 m below the seafloor, and has a lateral extent of up to 3000 m, meaning $\delta = 3200$ m maximum. These numbers give a target body aspect ratio of at least $\gamma = 4 \times 10^{-3}$, satisfying the requirement that $\gamma >> \varepsilon^{1/4}$.

Based on these results, we can safely conclude the following: 1. Our in-house developed code based on cuboids or point masses are working correctly. 2. With the grid sizes and geometry at Sleipner, we expect the numerical error in the modeling code to be much less than the observable gravity signal. 3. Also, due to the geometry at Sleipner and the close grid spacing of the seismic horizons and reservoir simulation models ($z/\lambda > 1$), we can use the faster point mass code for time-lapse gravity modeling without any loss in precision.

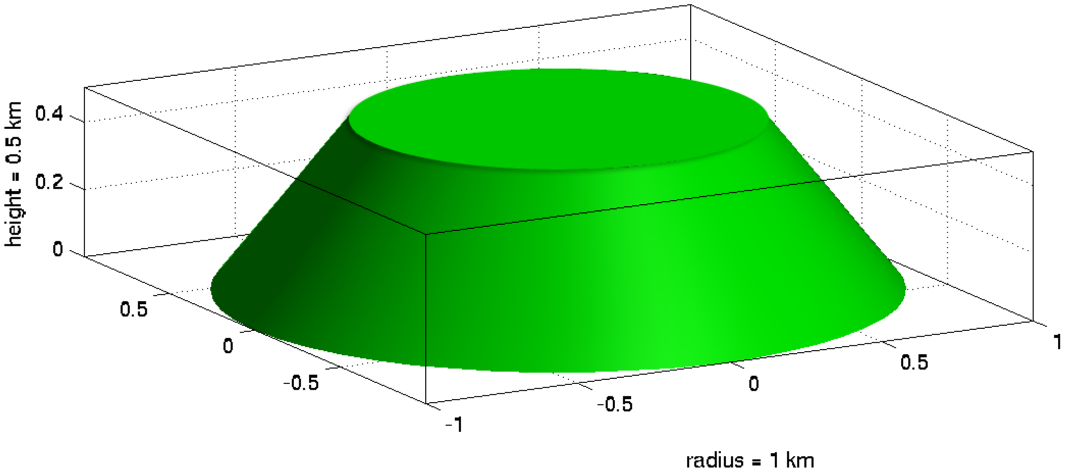

Figure 2.25 Frustum body of mass used to test the gravity code (also shown in Figure 2.26).

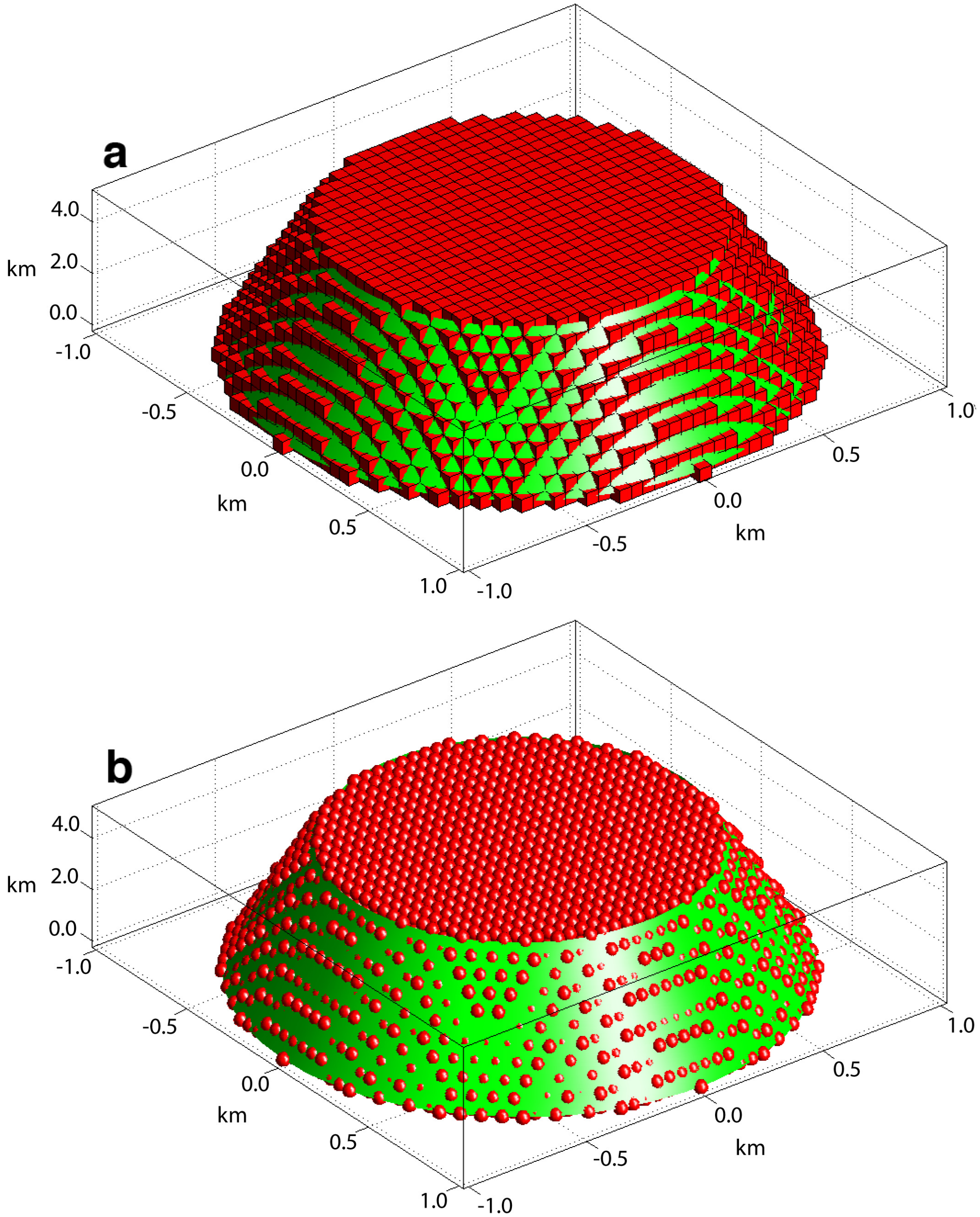

Figure 2.26 The gravity code approximations to a ‘real’ frustum. The real frustum, shown in green, is shown slicing through a.) a frustum approximated by cuboids, and b.) a frustum approximated by spheres or point masses. It is clear from this figure that as the grid size increases, the approximation to the real mass body worsens.

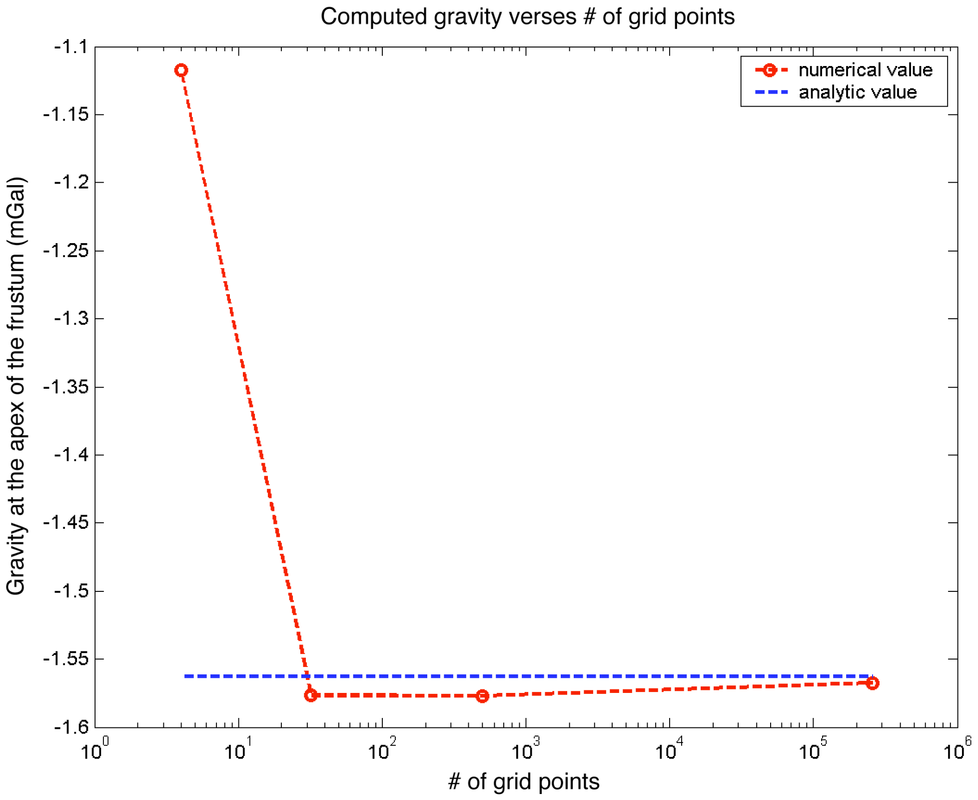

Figure 2.27 This plot shows that as the grid spacing decreases (number of grid points increases), the gravity computed from the frustum (red curve) approaches the analytic value (shown in blue)

2.5.2 Modeling time-lapse gravity changes using seismically imaged CO_2

Chadwick et al. [2002] modeled the *in situ* CO_2 using the 1999 reflection seismic data. They observed that any viable plume saturation model must satisfy three conditions: 1. It must reproduce observed reflectivity. 2. It must produce the observed velocity pushdown. 3. The volume of CO_2 in the model must match the known injected volume. We are adding to this two more requirements: 4. The model must produce the observed gravity change. 5. It must produce the observed seafloor deformation.

The seismic data from 1999 and 2001 were used to build models of injected CO_2 for two scenarios. The first is for an average CO_2 density within the reservoir of 700 kg/m^3, and the second is for an average CO_2 density of 550 kg/m^3. These correspond to low reservoir temperature (35 ºC) and high reservoir temperature (45 ºC) scenarios, respectively. These models contain supercritical CO_2 in two distinct parts. The first is CO_2 residing in thin high saturation layers, which have ponded beneath thin inter-reservoir shale layers. These can be seen as layers of increased reflectivity in the time-lapse seismic data (Figure 2.5). The second volume of CO_2 is a low saturation diffuse volume occupying the space between the high saturation layers. This diffuse volume of CO_2 does not cause increased reflectivity, but its existence is indicated by a larger observed seismic pushdown than is expected from the high saturation layers alone. The amount of diffuse CO_2 is uncertain, and depends upon the CO_2 density and upon the details of its distribution. The modeling approach is similar to *Chadwick et al.* [2002] and is summarized below:

1. Calculate a thin-layer model for the high saturation CO_2 layers.
2. Calculate the gravity from this model.
3. Calculate the velocity pushdown from this model.
4. Subtract the calculated pushdown from the observed pushdown to obtain the residual pushdown.
5. Use the residual pushdown to calculate the average vertical saturation for the diffuse volume.

6. Calculate the gravity from the diffuse CO_2 model and combine with the gravity calculated from the layers.
7. Compute the total mass and volume of CO_2 in the combined model.

The reflection amplitude of the seismic horizons was provided as xyz data by Ola Eiken and the SACS consortium. To work with the data, each horizon was first converted into to a regularly spaced grid. For the thin layer model, the reflection amplitudes of the horizons were then linearly related to layer thickness with the maximum reflection amplitude being set equal to 8 m, corresponding to the tuning thickness of the seismic wavelet [*Arts et al.*, 2002b]. The mass of CO_2 at each grid point can be calculated by

$$m = \rho_{CO_2} S_{CO_2} \phi \cdot dx \cdot dy \cdot dz\,, \qquad 2.5.5$$

where *dx* and *dy* are the grid spacings, *dz* is the layer thickness, ρ_{CO_2} is the density of CO_2, ϕ is the porosity, and S_{CO_2} is the saturation of CO_2. The only unknown is the saturation of CO_2, which varies with height, *h*, in each CO_2 layer due to capillary pressure, p_c, between the formation brine and injected CO_2. This relationship in SI units was determined by centrifuge experiments on core material from the Utsira Sand [*Chadwick et al.*, 2002; *Chadwick et al.*, 2004]:

$$p_c = \Delta\rho g h = 810.35(1 - S_{CO_2})^{-0.948}\,. \qquad 2.5.6$$

In the above equation $\Delta\rho$ is the density difference between sea water and CO_2 within the reservoir. Figure 2.28 shows the CO_2 saturation as a function of height, *h*, and the average layer saturation as a function of layer thickness, *dz*. The average saturation was obtained by solving equation 2.5.6 for S_{CO_2} and substituting into the following:

$$S_{ave} = \frac{1}{dz}\int_0^{dz} S_{CO_2}\, dh. \qquad 2.5.7$$

The mass of CO_2 at each grid point can then be calculated from equation 2.5.5 using the layer thickness, *dz*, and the average CO_2 saturation, S_{ave}.

The thin layer mass calculated for the low-density (high reservoir temperature) case is 0.853 MT in 1999 (36.3% of the injected amount) and 1.5 MT in 2001 (34.0% of the injected amount). For the high-density (high reservoir temperature) case, the mass is 1.53 MT in 1999 (65.1% of the injected amount) and 2.69 MT in 2001 (61.2%

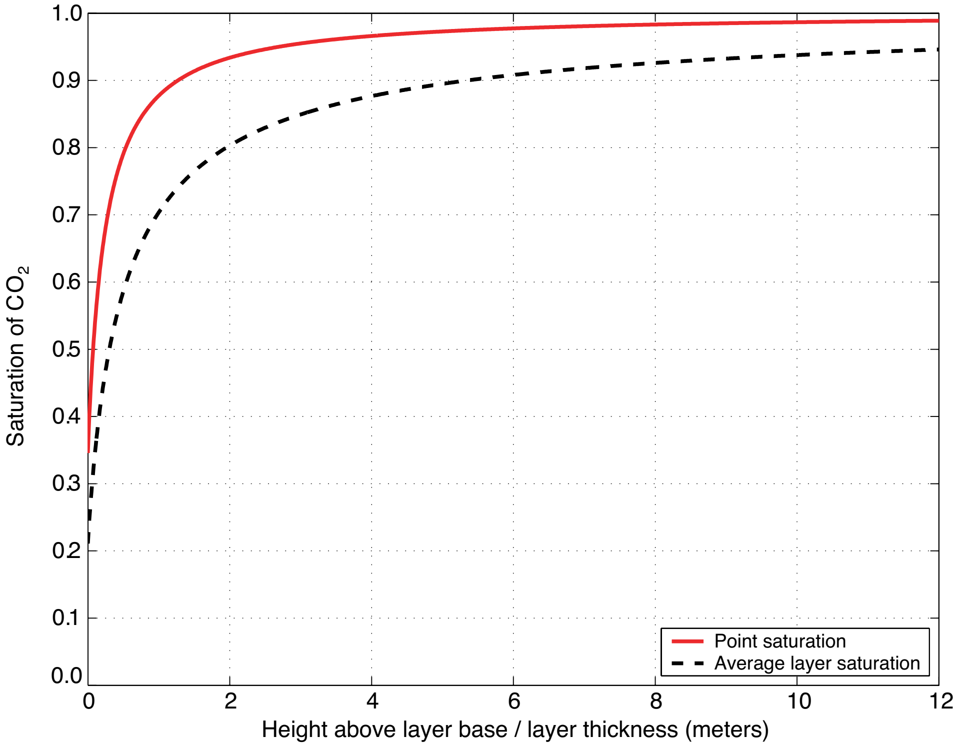

Figure 2.28 Plot showing both point saturation as a function of height above layer base (solid curve) and average layer saturation as a function of layer thickness (dashed curve). Both are calculated from the capillary pressure – saturation relationship given in equation 2.5.6.

of the injected amount). Uncertainty in these figures comes from uncertainty in the interpretation of the seismic horizons, errors in the simple amplitude to thickness conversion, and reflectivity attenuation in the deeper parts of the plume which are difficult to quantify [*Chadwick et al.*, 2002]. The 3-D gravity modeling code was then used to compute the gravity signal from the thin CO_2 layers. These results are shown in Table 2.3.

The seismic pushdown from the layers is the difference in two-way travel-time (twtt) caused by the presence of the CO_2. This can be found from the change in seismic velocity, which can be determined using Gassmann's relationships (Equations 2.1.1 and 2.1.2) and Equation 2.1.3. Figure 2.6 shows the seismic velocity versus CO_2 saturation for both high temperature (low density) and low temperature (high density) cases. The velocity changes rapidly for low saturations, but for saturations larger than about 0.2 it changes very little, particularly for homogeneous distributions. The pushdown for each density scenario for both years was then calculated and subtracted from the total observed pushdown to give the residual pushdown (Figure 2.29). This residual pushdown is caused by CO_2 that is not present in the thin layers, and requires the presence of additional CO_2 within the reservoir.

Using only the thin, high saturation CO_2 layers does not account for either the total injected mass or the total observed pushdown for either density scenario. The residual pushdown is concentrated in the central region of the plume, near the central

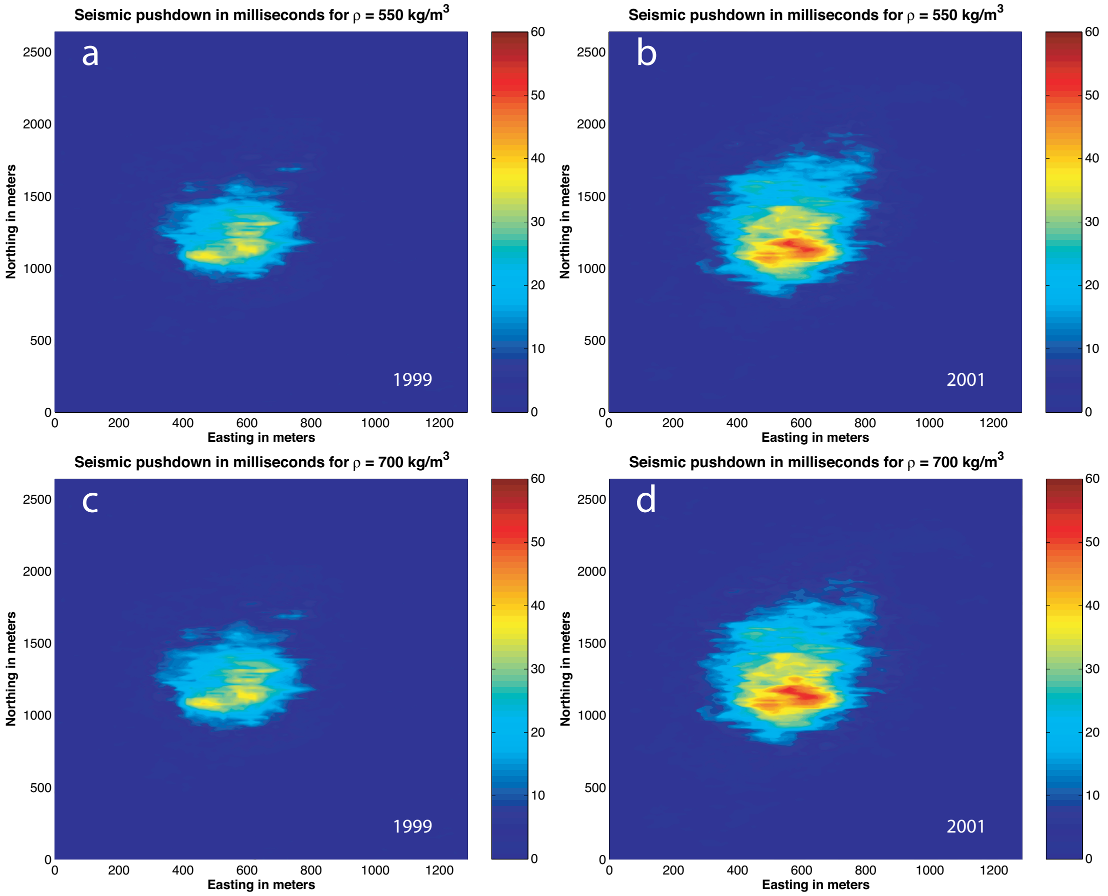

Figure 2.29 Residual pushdown in milliseconds is calculated by subtracting the theoretical pushdown of the CO_2 horizons from the observed pushdown. Pushdown for a.) 1999 low-density model, b.) 2001 low-density model, c.) 1999 high-density model, and d.) 2001 high-density model. There is very little difference in the residual pushdown for the two density cases.

chimney, consistent with the presence of diffuse CO_2 in the axial region. *Arts et al.* [2002b] plotted seismic amplitudes against velocity pushdown in various parts of the plume. Outer parts of the plume obey the thin-bed tuning relationship, whereas in axial parts of the plume, pushdown values are much higher for a given seismic amplitude. This indicates the presence of lower saturation CO_2. *Chadwick et al.* [2004] showed that the ratio of velocity pushdown to plume reflectivity is much higher in the axial parts of the plume than at its edges, also consistent with the presence of diffuse CO_2.

The next step, then, is to use the residual pushdown to estimate the saturation and mass of the diffuse CO_2 volume using the velocity versus saturation curves shown in Figure 2.6. The pushdown, ΔT, is defined as follows:

$$\Delta T = 2\left(\frac{1}{V_{S_{CO_2}}} - \frac{1}{V}\right)dz, \qquad 2.5.8$$

where $V_{S_{CO_2}}$ is the seismic velocity with CO_2 present, V is the velocity without the presence of CO_2, and dz is the vertical thickness of the CO_2. Equation 2.5.8 can be rearranged to solve for $V_{S_{CO_2}}$ from the pushdown:

$$V_{S_{CO_2}} = \left(\frac{\Delta T}{2dz} + \frac{1}{V}\right)^{-1}. \qquad 2.5.9$$

To solve for $V_{S_{CO_2}}$ from equation 2.5.9, an estimate must be made for the vertical thickness, *dz*. This introduces a non-unique element into the problem. An infinite number of distributions of diffuse CO_2 can be made to satisfy the residual pushdown. To estimate *dz* in a meaningful way, we first defined a volume enclosing the diffuse CO_2. A reasonable assumption is that the diffuse CO_2 resides near the higher saturation volumes (the thin layers and the chimney), but is not found some characteristic distance away, which we chose to be 25 m. This value is two times the grid spacing and is close to the average distance between shale layers, which is 30 m. Therefore, an algorithm stepped through the seismic horizons and every grid point within the characteristic distance from a high saturation grid point was included in the volume. Points that were within 1.75 m of a seismic horizon (corresponding to the average CO_2 layer thickness) were excluded from the volume. This created the gridded 3-D volume enclosing the horizons shown in Figure 2.30. The vertical thickness, *dz,* was then calculated by summing the number of grid points in each vertical column included in the volume and multiplying each resulting number by the vertical grid spacing (12.5 m). The residual pushdown, ΔT, and the vertical thickness, *dz*, were then used together to solve for the average velocity, $V_{S_{CO_2}}$, through the diffuse CO_2.

A density of CO_2 was then chosen and $V_{S_{CO_2}}$ was then used to determine an average CO_2 value at each point using the appropriate velocity versus saturation curve from Figure 2.6 (which we digitized). Because the seismic velocity changes very little for saturation values greater than 0.2, small errors in the calculation of $V_{S_{CO_2}}$ can lead to large uncertainty in the resulting saturation estimate. These uncertainties are difficult to quantify. Nevertheless, the resulting model for the diffuse volume is a CO_2 distribution in which the CO_2 saturation varies laterally, but is constant vertically. This is obviously not likely to be the real distribution, but it probably provides a good estimate of the gravity field, since the vertical variation will have little effect on gravity.

The mass in the diffuse volume can then be calculated from equation 2.5.5. For the low-density case, the diffuse CO_2 contains 0.15 MT for 1999 and 0.28 MT for 2001. Adding this to the thin layer mass gives 1.43 MT for 1999 (60.94 % of the known injected mass) and 2.53 MT for 2001 (59.36 % of the known injected mass).

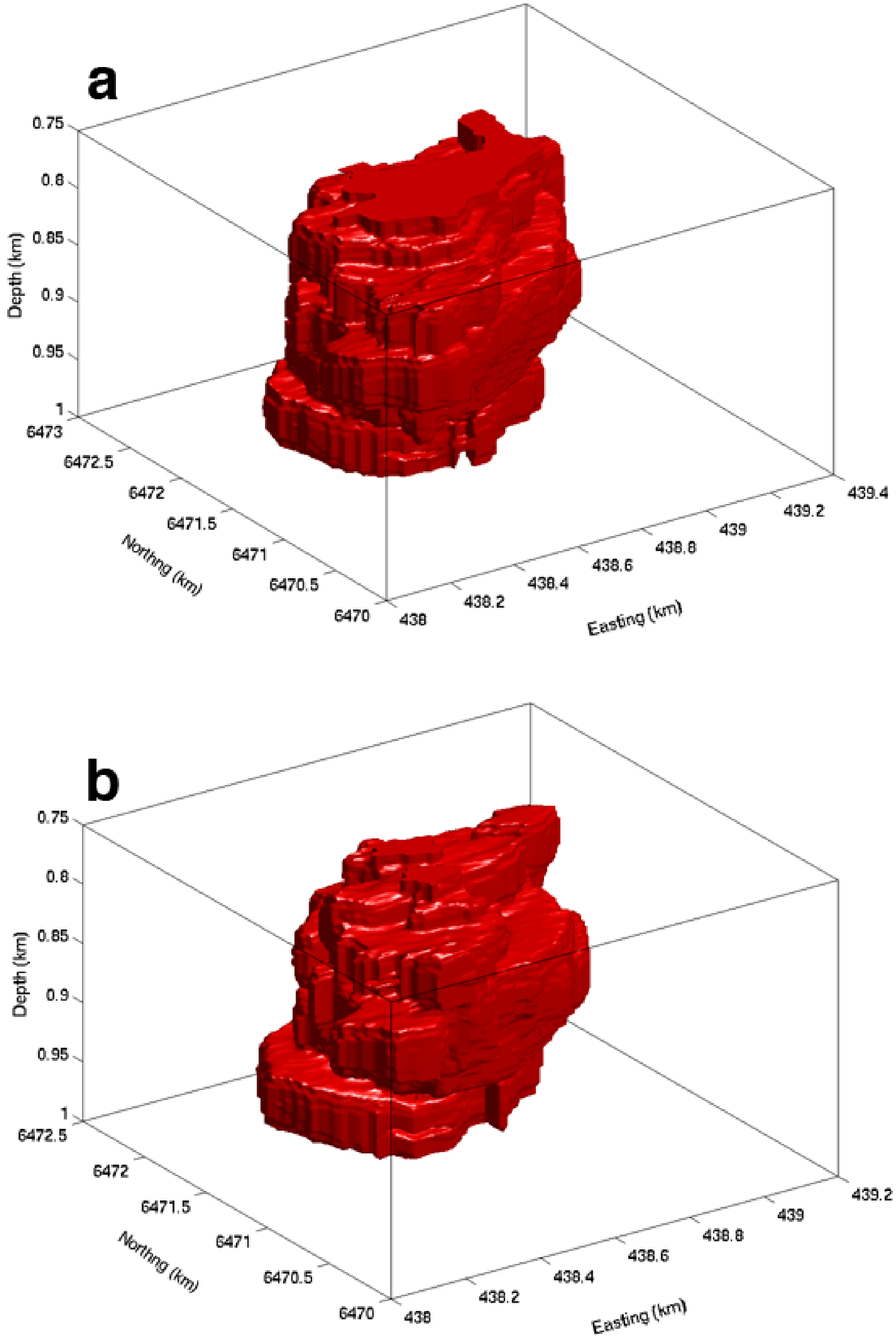

Figure 2.30 The volume enclosing the diffuse, low-saturation CO_2 in the models based on the time-lapse 3-D seismic data for a.) 1999 and b.) 2001.

For the high-density case, the diffuse CO_2 contains 0.384 MT for 1999 and 0.752 MT for 2001. Adding this to the thin layer mass gives 1.94 MT for 1999 (82.75 % of the known injected mass) and 3.49 MT for 2001 (81.85 % of the known injected mass). The contribution of the diffuse volume to the gravity signal is then calculated with our 3-D code. Table 2.3 shows the contribution of each part of the model to the maximum gravity signal for each density scenario. Combining the layer contribution with the diffuse volume contribution indicates that the high-density scenario would cause maximum change of about 2.7 μGal/year, while the low-density scenario would cause a maximum change of about 3.5 μGal/year (Figure 2.31). The ramifications of this will be discussed in section 2.6.

2.5.3 Modeling time-lapse gravity changes using reservoir simulation models

Reservoir simulation models provide insight into the behavior of the injected CO_2. However, these flow models are highly dependent on reservoir characteristics such as temperature. Calculating the expected gravity change on the seafloor from reservoir flow models provides a way, independent of seismic data, to use time-lapse gravity to put constraints on the density (hence temperature) of CO_2 within the Utsira formation. Reservoir modeling at Sleipner has been done by the Norwegian company SINTEF, Scandinavia's largest independent research organization (http://www.sintef.no). SINTEF produced 3-D saturation grids from CO_2 flow simulations, which were created using the commercial reservoir modeling software Eclipse. The models were for a three-dimensional volume with a permeability of 2 darcy and a porosity of 0.38, cut laterally by five impermeable layers (representing

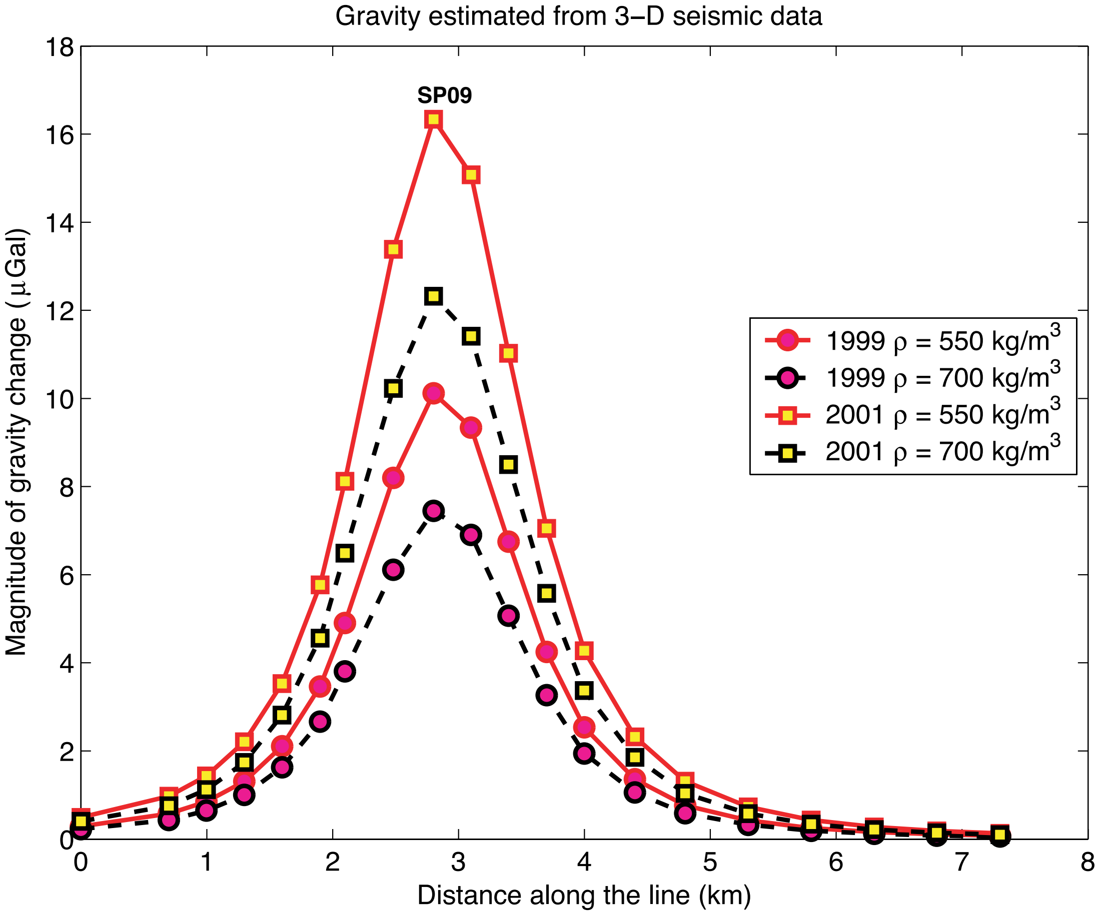

Figure 2.31 This plot shows the magnitude of the gravity change calculated from the both the 1999 and 2001 seismic data. The points along the line represent the seafloor benchmarks along the NW-SE line shown in Figure 2.10 (benchmark SP09 is indicated above). Calculations were made using two different densities, as indicated in the figure.

shale). The shape of these layers was guided by the geometry of the seismically imaged CO_2 horizons. The boundaries of the model volume were kept at a constant pressure, simulating an infinite reservoir [*Sjur Mo*, personal communication, 2003]. Two types of simulation models were examined. The first type, model I, has a central chimney and horizontal CO_2 layers like the seismic model; however, it has no low saturation volume (Figure 2.23). The engineers at SINTEF have not been able to produce a CO_2 flow scenario resulting in a low saturation volume as suggested by the seismic pushdown. Therefore, a second model was examined, model II, composed of several micro-chimneys, which, if small enough, might look like a diffuse volume of CO_2 to seismic energy (Figure 2.23). This was created by randomly distributing 640 holes within the impermeable shale layers. Each hole has an increased permeability. Simulations for model II spanning 20 years were computed by SINTEF for average reservoir temperatures of both 37 ºC and 45 ºC, corresponding to CO_2 densities of ρ_{co_2} = 750 kg/m^3 and ρ_{co_2} = 550 kg/m^3 (call them models IIa and IIb, respectively). The CO_2 injection rate plotted against year for the simulations is shown in Figure 2.32. The reservoir simulations also predict the amount of CO_2 that dissolves in the brine over time (Figure 2.32). Therefore, the mass contributing to the gravity signal will be the total injected amount of CO_2 minus the dissolved CO_2.

The output of each flow model is a volumetric CO_2 saturation grid containing 428,400 grid points ($70 \times 85 \times 72$). The thickness of the grid blocks varies from 15.2 m to 0.2 m with depth, as the grid is refined below the shale layers (where most of the CO_2 resides). The horizontal grid spacing is constant at dx = 34.4 m and dy = 36.1 m.

The results of these reservoir models were used in the current study to calculate the expected seafloor gravity caused by the CO_2 injection. Saturation, S_{CO_2}, was converted to a change in mass at each grid point using a reservoir porosity of ϕ = 0.37, a shale fraction of ν_{sh} = 0.01, a cell volume of $V = dx \cdot dy \cdot dz$, and a CO_2 density ρ_{CO_2} dependent on the flow model:

$$\Delta M = \Delta\rho V\phi(1-\nu_{sh})S_{CO_2}, \qquad 2.5.10$$

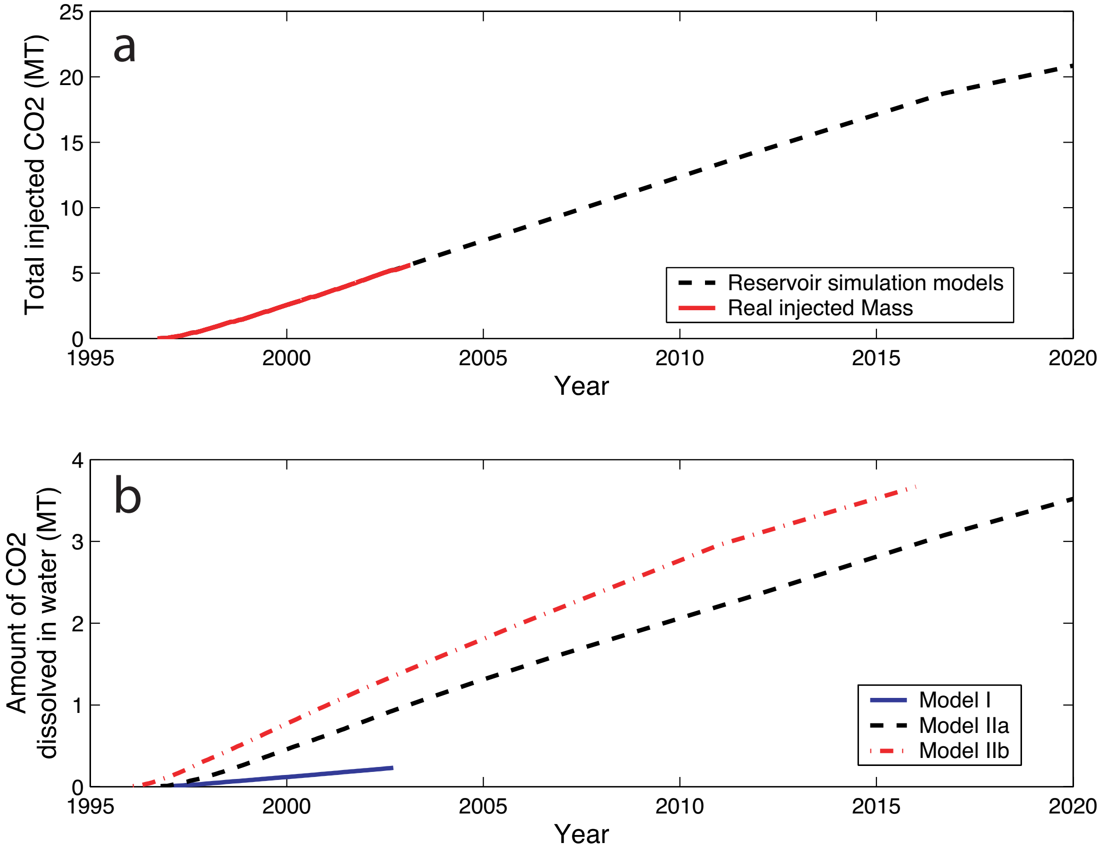

Figure 2.32 a.) The total injected CO_2 mass in MT is plotted in red. The injected mass used in the reservoir simulation models follows the real injected mass until 2004 and continues along the black dashed line. b.) The expected amount of dissolved CO_2 in MT is shown for the different reservoir simulation models. Dissolution rates are approximately 4% for Model I, 17% for Model IIa, and 23% for Model IIb.

where $\Delta M = M_{CO_2} - M_{H_2O}$ and $\Delta\rho = \rho_{CO_2} - \rho_{H_2O}$. Gravity was then calculated using either equation 2.5.2 or 2.5.3 by treating each mass ΔM as a point mass. Later, a new computer (Power Mac G5, dual 2.5 GHz) allowed us to recalculate gravity for each simulation model, treating each grid block as a cuboid. The results are indistinguishable from the point mass approximation.

The time varying gravity spanning 1996 to 2002 computed on the seafloor benchmarks from model I is shown in Figure 2.33, indicating a maximum gravity change of about 2.2 μGal/year. Model IIa (Figure 2.33) spans the years 1996 to 2016 and predicts a maximum change of about 2.4 μGal/year. A comparison of these two models is shown in Figure 2.34 for 2001. Interestingly, the results are almost identical, in spite of the fact that the models have different dissolution rates for CO_2 into the aquifer brine. Model I is composed of a horizontal layers central chimney, while model IIa is composed of horizontal layers and multiple vertical chimneys. This means that model IIa has a larger surface area of CO_2 in contact with the brine, allowing more dissolution to take place (~4.5 % in model I and ~17.5% in model IIa, Figure 2.32b). Therefore, for the same amount of injected mass, model I has more undissolved CO_2.

Figure 2.33c shows the time varying gravity for model IIb, which predicts a maximum gravity change of 4.7 μGal/year. The higher temperature of model IIb causes the CO_2 density to decrease, creating a larger density difference between the CO_2 and formation water. The lower density CO_2 also occupies more volume within the reservoir, increasing surface area in contact with the brine. The dissolution into water in this case is more than 23% (Figure 2.32b). The lower density CO_2 is also more buoyant, which tends to increase the gravity driven vertical flow. Therefore, compared to model IIa, more mass in model IIb is located in the shallow layers. By the year 2011, 6% of the injected CO_2 is flowing out of the model boundaries. There is more than 20% outflow by 2016, so the results for this year are an underestimate.

It is interesting to calculate the theoretical pushdown for the three models using velocity versus saturation relations shown in Figure 2.6. The saturation in each

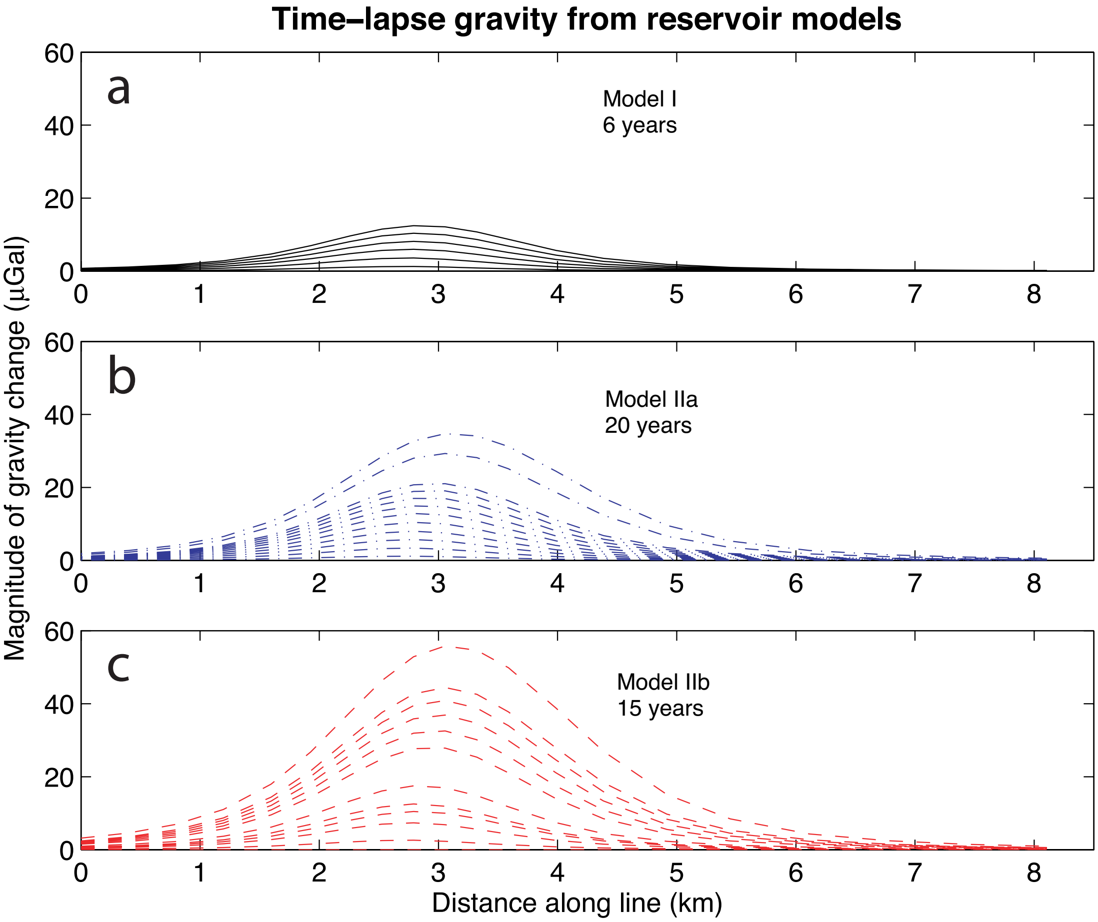

Figure 2.33 This figure shows the time varying gravity signals calculated from the reservoir simulation models. All models begin in 1996 and step forward by one year at a time. Model I stops in 2002 and Models IIa and IIb continue until 2006. These two models then jump to 2011 then Model IIa jumps to 2016. The results are shown above for a.) Model I, b.) Model IIa, and c.) Model IIb.

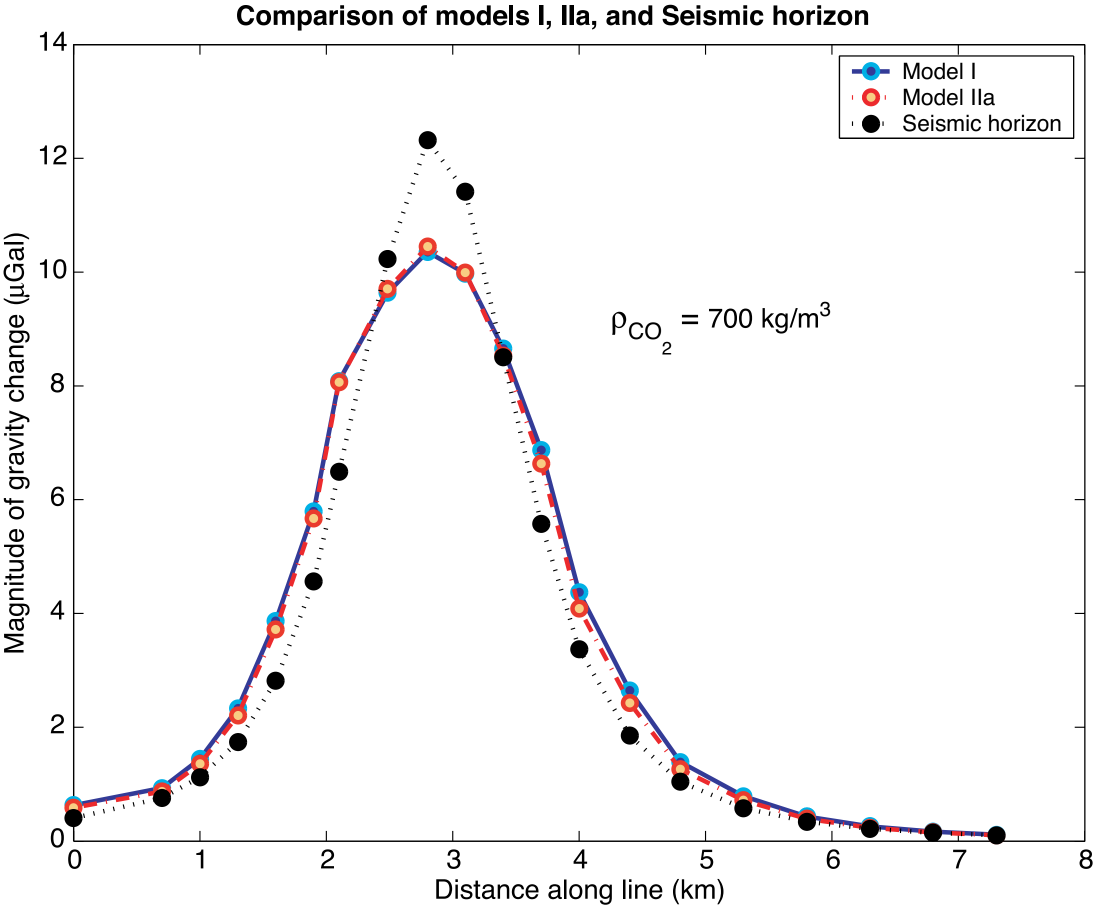

Figure 2.34 A comparison of the gravity calculated from models I and IIa, and from the seismic horizons in 2001. The injected mass is the same for both models (4.26 MT) and the density of CO_2 is 700 kg/m^3. The detailed geometry of the CO_2 distribution makes very little difference in the two reservoir models, but the seismic model differs in shape and maximum signal. However the maximum gravity change from 1999 is almost the same for all three models.

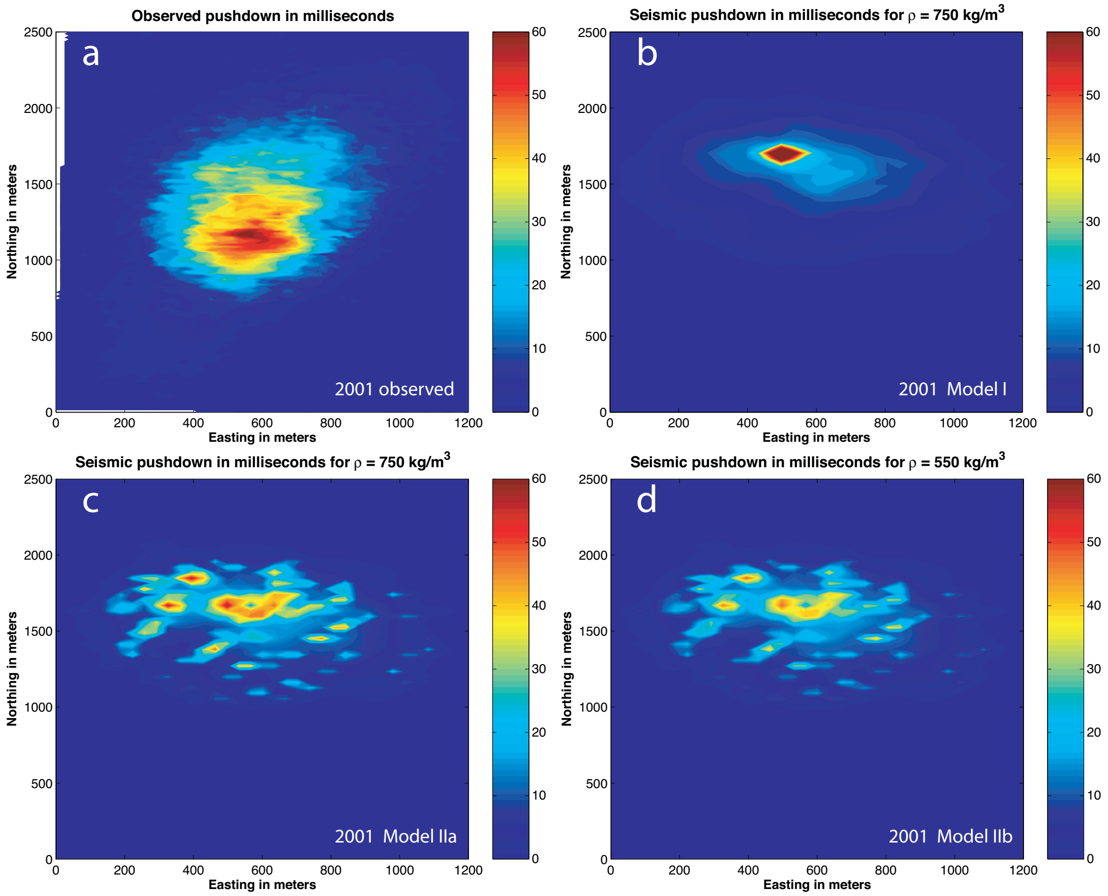

Figure 2.35 The pushdown estimated from the reservoir simulation models in comparison with the observed pushdown for 2001. a.) The observed pushdown, b.) Model I, c.) Model IIa, d.) Model IIb.

grid cell is an average saturation value for the volume enclosed. The residual pushdown for the three models is shown in Figure 2.35. None fits the observed pushdown that well, most likely due to the lack of a low saturation diffuse volume of CO_2, which causes a large amount of pushdown for a relatively small mass. In fact, the pushdown from the reservoir simulation models show distinct points of large pushdown rather than the observed smooth distribution of pushdown. It seems possible that the seismically observed values contain some amount of horizontal averaging, although this possibility has not been reported.

2.6 Discussion

By modeling the seismically imaged horizons in 1999 and 2001 as thin, high saturation layers and the residual seismic velocity pushdown as a low saturation non-reflective diffuse volume of CO_2, estimates for in situ CO_2 mass can be made. However, not all of the known injected amount of CO_2 is accounted for in these models. The high-density model, ρ_{co_2} = 750 kg/m^3, was able to account for almost 82% of the known injected mass. From the reservoir simulation models, we expect about 17% dissolution into aquifer water for the high-density case, suggesting that 99 % of the injected mass is contained. However, if the CO_2 in the aquifer is in the low-density state, with ρ_{co_2} = 550 kg/m^3, the seismic model accounts for only about 60% of the injected mass, assuming a uniform distribution for the diffuse CO_2. Reservoir simulations indicate that just less than 23% dissolution of CO_2 into water would occur, thus accounting for only about 83% of the injected mass. This leaves 17% of the mass missing in both 1999 and 2001.

As discussed in section 2.4.1, for fluid filled rock, pore pressures can equilibrate over spatial scales of $L_c \approx \sqrt{kK_{fl}/f\eta}$, where f is the seismic frequency, k is the permeability, η is viscosity, and K_{fl} is the bulk modulus of the fluid [e.g., *Mavko and Mukerji*, 1998]. Heterogeneous saturations with length scales greater than L_c (referred to as patchy saturation) have wave-induced pore pressure gradients that cannot equilibrate, and patchy saturations always lead to higher seismic velocities than uniform saturations (saturations with length scales less than L_c). *Arts et al.* [2002b] showed that a patchy diffuse volume consisting of small patches of high saturation CO_2 could be constructed that would match both the observed pushdown and the injected mass for low-density CO_2. The reservoir simulation models seem to support the idea of heterogeneous saturation over a low saturation diffuse volume of CO_2 in that it is difficult to create large areas of uniform low saturation CO_2 from the physical flow models. This becomes obvious when comparing the predicted pushdown from the reservoir models to the observed pushdown (Figure 2.35). Heterogeneous saturations, however, can easily be caused by fingering of pore fluids and spatial variation in wettability, permeability, shaliness and etc.

It is useful to revisit the low-density gravity model calculated from the seismic data in terms of a patchy CO_2 volume. It is a straightforward exercise to imagine putting the missing 17% back into the diffuse volume and redistributing the volume in such a way that the pushdown constraint is satisfied. From Table 2.4 it is apparent that (looking at the maximum gravity predicted) the diffuse volume of CO_2 accounts for 8.0 μGal/MT in 1999 and about 7.6 μGal/MT in 2001. Putting the missing 17 % of the injected CO_2 mass back into the model each year at the rates above adds 3.2 μGal to the maximum gravity in 1999 and 5.5 μGal in 2001. This means that the expected change in the maximum gravity increases from 3.3 μGal/yr to 4.5 μGal/yr.

Using this value means that the maximum gravity value predicted by the two types of models (seismic and reservoir simulation) have good agreement (Table 2.4).

This indicates that the detailed geometry of the CO_2 bubble will not have a large effect on the observed gravity. This insensitivity to detailed flow geometry suggests that magnitude of the maximum time-lapse gravity signal we observe will be due to primarily CO_2 density, insuring that this technique will provide a robust estimate of CO_2 density. However, the gravity changes expected are small, meaning it may take some time to determine the CO_2 density. The difference between the two scenarios presented here (550 kg/m^3 and 750 kg/m^3) is about 2 μGal/yr, so after 5 or 6 years of measurements it should be possible to distinguish between the two with some confidence (our expected detection threshold is ~5 μGal). If the actual CO_2 density is between those two values, however, it will take more time to be able to make a confident statement about the density, perhaps up to 10 years or more. Finally, if the CO_2 density is lower than 550 kg/m^3, less time will be needed to determine the density.

The shape of the gravity curves (Figure 2.34) reflect the geometry of the CO_2 bubble to some extent, especially in the shape of the reservoir models versus the seismic model. The wider peak in the reservoir models results from the CO_2 flow in the reservoir model going more east-west than the real flow. Over time, we may also be able to examine details of CO_2 flow using the shape of the gravity profile, but this will probably be beyond the resolution of the technique for a three year time period. Note that although the peak in the seismic model in Figure 2.34 is larger, the maximum change in gravity from 1999 is almost identical to the reservoir simulation models.

The first repeat gravity survey is scheduled for late summer of 2005, for a time span of three years. Therefore, we expect to see a maximum decrease in the observed gravity between 7 and 14 μGal, depending on the density of CO_2 within the reservoir (Table 2.4). Assuming the repeatability is similar to that of the first survey, it might just be possible to begin to distinguish between the two scenarios.

As a final exercise, we can examine an extreme case in which the reservoir temperature is warmer than 45 ºC. As the temperature increases, the average density of CO_2 within the reservoir decreases rapidly. Taking the average density of CO_2 as ρ_{co_2} = 350 kg/m^3 (caused by only a few degree increase), we can go through the procedure outlined in section 2.5.2 to calculate the expected gravity from the seismically imaged horizons. The pushdown can be estimated using the velocity versus saturation from the 45 ºC curve shown in Figure 2.6. This is obviously not completely accurate and will tend to under predict the mass of CO_2 by a few percent. However, this will give us a good feel for what to expect for an extreme scenario. Table 2.3 shows the results of this calculation. The total mass estimated from the model is only 40% of the total injected mass. The contribution of the diffuse volume to gravity is about 17.8 μGal/MT in 1999 and 16.5 μGal/MT in 2001. Assuming a dissolution of 40% (a very large amount) and distributing the missing 20% of the injected mass into patchy saturation volume, the expected gravity change is to 7.4 μGal/yr. For a three year time span, the maximum gravity change would be 22.2 μGal. With less dissolution of CO_2 the change in gravity could be even larger. This signal would be clearly discernable in the gravity data. In fact, assuming no dissolution gives a change of ~13 μGal/yr applying the same logic. Comparing this to the feasibility study of *Williamson et al.* [2001], which predicted 15 μGal/yr for $\rho_{\mathrm{co}_2} = 350$ kg/m^3 and no dissolution, we again see that the detailed flow geometry will have minimal effect on the estimate of CO_2 density from gravity.

To date, no reservoir simulation models have been calculated for temperatures higher than 45 °C, although heat flow data in the area are consistent with reservoir temperatures of 45 °C and higher. Therefore, the amount of CO_2 dissolution is speculation at this point. However, it should be clear from the repeat gravity measurements which end of the temperature range the reservoir is in.

The results of this study indicate that time lapse gravimetric reservoir monitoring may play a role in future CO_2 sequestration efforts. This detection technique relies on the density contrast between injected CO_2 and the aquifer fluids, limiting its applicability to fluid filled reservoirs and excluding formations such as depleted coal beds. The best results will be obtained when monitoring shallow reservoirs less than 1000 m deep, where the density of CO_2 is much less than that of the reservoir fluids. In order to halt CO_2 emissions, as is needed to mitigate anthropogenic climate change, hundreds of sites such as Sleipner will be needed along with many other carbon reduction strategies. Undoubtedly, gravity will be a useful tool for monitoring injected CO_2 for a number of these sites.

Table 2.4 Summary of the maximum magnitude of the gravity change expected per year for each of the different models. The values given for the seismic horizon models with and ρ_{co_2} = 550 kg/m^3 are an estimate of the result of redistributing the diffuse CO_2 to match the pushdown and injected mass (see the text).

Model	**ρ_{CO2} (kg/m^3)**	**Maximum change (μGal/yr)**
Seismic horizon	350	~7.4
Seismic horizon	550	4.5
Seismic horizon	700	2.7
Model I	700	2.2
Model IIa	700	2.4
Model IIb	550	4.7

2.7 References

Agnew, D.C., SPOTL: Some programs for Ocean-Tide Loading, *Scripps Institution of Oceanography Reference Series*, 96-98, 1996.

Allis, R.G., and T.M. Hunt, Analysis of expoitation-induced gravity changes at Wairakei geothermal field, *Geophysics*, *51*, 1647-1660, 1986.

Andres, R.B., and J.R. Pedersen, Monitoring the Bullalo geothermal reservoir, Philippines, using precision gravity data, *Geothermics*, *22*, 395-402, 1993.

Arts, R., O. Eiken, A. Chadwick, P. Zweigel, L. van der Meer, and B. Zinszner, Monitoring of CO_2 Injected at Sleipner using time lapse seismic data, in *Abstracts of the 6th International Conference on Greenhous Gas Control Technology (GHGT-6)*, Kyoto, Japan, 2002a.

Arts, R., R. Elsayed, L. van der Meer, O. Eiken, S. Østmo, A. Chadwick, G. Kirby, and B. Zinszner, Estimation of the mass of injected CO_2 at Sleipner using time-lapse seismic data, in *EAGE, Annual meeting*, Florence, Italy, 2002b.

Babcock, J.M., B.A. Kirkendall, and J.A. Orcutt, Relationships between ocean bottom noise and the environment, *Bulletin of the Seismollogical Society of America*, *84* (6), 1991-2007, 1994.

Ballu, V., J. Dubois, G.C. Deplus, M. Diament, and S. Bonvalot, Crustal structure of the Mid-Atlantic Ridge south of the Kane fracture zone from seafloor and sea surface gravity data, *Journal of Geophysical Research*, *103*, 2615-2631, 1998.

Barnola, J.M., D. Raynaud, Y.S. Korotkevich, and C. Lorius, Vostok ice core provides 160,000-year record of atmospheric CO_2, *Nature*, *329*, 408-414, 1987.

Barnola, J.M., D. Raynaud, C. Lorius, and N.I. Barkov, Historical CO_2 record from the Vostok ice core, in *In Trends: A Compendium of Data on Global Change*, Carbon Dioxide Information Analysis Center, Oak Ridge National Laboratory, U.S. Department of Energy, Oak Ridge, TN, 2003.

Chadwick, R.A., R. Arts, and O. Eiken, 4D seismic quantification of a growing CO_2 plume at Sleipner, North Sea, *unpublished*, 2002.

Chadwick, R.A., R. Arts, O. Eiken, G.A. Kirby, E. Lindeberge, and P. Zweigel, 4D seismic imaging of an injected CO_2 plume at the Sleipner Field, central North Sea, in *3D Seismic Technology*, edited by R.J. Davies, J.A. Cartwright, S.A. Stewart, M. Lappin, and J.R. Underhill, Geological Society of London, London, 2004.

Chadwick, R.A., S. Holloway, G.A. Kirby, U. Gregersen, and P.N. Johannessen, The Utsira Sand, Central North Sea--An assessment of its potential for regional desposal, in *The 5th International Conference on Greenhouse Gas Control Technologies*, Cairns, Australia, 2000.

Cochran, J.R., B.J. Coakley, D.J. Fornari, and R.E. Herr, Continuous underway near-bottom gravity measurements from a submersible, *EOS, Transactions of the American Geophysical Union*, *75*, 579, 1994.

Eidvin, T., F. Riis, and Y. Rundberge, Upper Cainozoic stratigraphy in the central North Sea (Ekofisk and Sleipner fields), *Norsk Geologisk Tidsskrift*, *79*, 97-128, 1999.

Eiken, O., M. Zumberge, and J. Hildebrand, Method for monitoring seafloor subsidence and for gravity monitoring an underground hydrocarbon reservoir, Den Norske Stats Oljeselskap A.S.; The Regents of the University of California, United States, 2004.

Evans, R.L., A seafloor gravity profile across the TAG hydrothermal mound, *Geophysical Research Letters*, *23*, 3477-3450, 1996.

Fialko, Y., Y. Khazan, and M. Simons, Deformation due to a pressurized horizontal circular crack in an elastic half-space, with applications to volcano geodesy, *Geophysical Journal International*, *146* (1), 181-190, 2001.

Glennie, K.W., *Petroleum geology of the North Sea: basic concepts and recent advances*, Blackwell Science Ltd, London, 1998.

Götze, H.J., and B. Lahmeyer, Application of three-dimensional interactive modeling in gravity and magnetics, *Geophysics*, *53*, 1096-1108, 1988.

Han, D., and M.L. Batzle, Gassmann's equation and fluid-saturation effects on seismic velocities, *Geophysics*, *69* (2), 398-405, 2004.

Hildebrand, J.A., J.M. Stevenson, P.T.C. Hammer, M.A. Zumberge, R.L. Parker, C.G. Fox, and P.J. Meis, A seafloor and sea surface gravity survey of Axial Volcano, *Journal of Geophysical Research*, *95*, 12751-12763, 1990.

Holloway, S., R.A. Chadwick, G.A. Kirby, J.M. Pearce, U. Gregersen, P.N. Johannessen, L. Kristensen, P. Zweigel, and R. Arts, Work Area 1 (Geology), in *Saline Aquifer CO2 Storage (SACS)--Final report*, 2000.

Holmes, M.L., and H.P. Johnson, Upper crustal densities derived from sea floor gravity measurements: norther Juan de Fuca Ridge, *Geophysical Research Letters*, *20*, 1871-1874, 1993.

Holstein, H., and B. Ketteridge, Gravimetric analysis of uniform polyhedra, *Geophysics*, *61*, 357-364, 1996.

Johnson, J.W., and J.J. Nitao, Reactive transport modelling of geologic CO_2 sequestration at Sleipner, in *Greenhouse Gas Control Technologies*, edited by J. Gale, and Y. Kaya, pp. 327-332, Elsevier Science Ltd., Oxford, 2003.

Keeling, C.D., and T.P. Whorf, Atmostpheric CO_2 records from sites in the SIO air sampling network, in *In Trends: A Compendium of Data on Global Change*, Carbon Dioxide Information Analysis Center, Oak Ridge National Laboratory, U.S. Department of Energy, Oak Ridge, TN, U.S.A., 2005.

LaCoste, L., Measurement of gravity at sea and in the air, *Reviews of Geophysics*, *5*, 477-526, 1967.

Li, X., and M. Chouteau, Three-dimensional gravity modeling in all space, *Surveys in Geophysics*, *19*, 339-368, 1998.

Lindeberg, E., B. van der Meer, A. Moen, D. Wessel-Berg, and A. Ghaderi, Work Area 2 (Reservoir), in *Saline Aquifer CO2 Storage (SACS)--Final report*, 2000.

Longuet-Higgins, M.S., A theory of the origin of microseisms, *Philisophical Transactions of the Royal Society of London*, *A234*, 1-35, 1950.

Mavko, G., and T. Mukerji, Bounds on low-frequency seismic velocities in partially saturated rocks, *Geophysics*, *63* (3), 918-924, 1998.

Mogi, K., Relations between the eruptions of various volcanoes and the deformation of the ground surfaces around them, *Bulletin of the Earthquake Research Institute, University of Tokyo*, *36*, 99-134, 1958.

Murphy, J., M., D. Sexton, M. H., D. Barnett, N., G. Jones, S., M. Web, J., M. Collins, and D. Stainforth, A., Quantification of modelling uncertainties in a large ensemble of climate change simulations, *Nature*, *430*, 768-772, 2004.

Nagy, D., The gravitational attraction of a right rectangular prism, *Geophysics*, *31* (362-371), 1966.

Nolen-Hoeksema, R.C., Modulus-porosity relations, Gassmann's equations, and the low-frequency elastic-wave response to fluids, *Geophysics*, *65* (5), 1355-1363, 2000.

Okabe, M., Analytical expressions for gravity anomalies due to homogeneous polyhedral bodies and translations into magnetic anomalies, *Geophysics*, *31*, 362-371, 1979.

Parker, R.L., The rapid calculation of potential anomalies, *Geophysical Journal of the Royal Astronomical Society*, *31*, 447-455, 1973.

Parker, R.L., Improved Fourier terrain correction, Part I, *Geophysics*, *60* (4), 1007-1017, 1995.

Parker, R.L., Improved Fourier terrain correction, Part II, *Geophysics*, *61* (2), 365-372, 1996.

Petit, J.R., J. Jouzel, D. Raynaud, N.I. Barkov, J.M. Barnola, I. Basile, M. Bender, J. Chappellaz, M. Davis, G. Delayque, M. Delmotte, V.M. Kotlyakov, M. Legrand, V.Y. Lipenkov, C. Lorius, L. Pépin, C. Ritz, E. Saltzman, and M. Stievenard, Climate and atmospheric history of the past 420,000 years from the Vostok ice core, Antarctica, *Nature*, *399*, 429-436, 1999.

Petit, J.R., D. Raynaud, C. Lorius, J. Jouzel, G. Delaygue, N.I. Barkov, and V.M. Kotlyakov, Historical isotopic temperature record from the Vostok ice core, in *In Trends: A Compendium of Data on Global Change.*, Carbon Dioxide Information Analysis Center, Oak Ridge National Laboratory, U.S. Department of Energy, Oak Ridge, TN, 2000.

Plouff, D., Gravity and magnetic fields of polygonal prisms and application to magnetic terrain corrections, *Geophysics*, *41*, 727-741, 1976.

Pohánka, V., Optimum expression for computation of the gravity field of a homogeneous polyhedral body, *Geophysical Prospecting*, *36*, 733-751, 1988.

Rider, M.H., *The Geological interpretation of Well Logs*, 175 pp., Blackie and Son Limited, Glasgow, 1986.

Rymer, H., and G.C. Brown, Gravity fields and the interpretation of volcanic structures; geological discrimination and temporal evolution, *Journal of Volcanology and Geothermal Research*, *27* (229-254), 1986.

Sasagawa, G.S., W. Crawford, O. Eiken, S. Nooner, T. Stenvold, and M.A. Zumberge, A new sea-floor gravimeter, *Geophysics*, *68* (2), 544-553, 2003.

Segawa, J., and H. Fujimoto, Observatioin of an ocean bottom station installed in the Sagami Bay and replacement of the acoustic transponder attached to it: JAMSTECTR, *Deep Sea Research*, *256*, 251-257, 1988.

Sorokin, L.V., *Gravimetry and Gravimetrical Prospecting*, State Technology Publishing, Moscow, 1951.

Span, R., and W. Wagner, A new equation of state for carbon dioxide covering the fluid region from the triple-point to 1100 K at pressures up to 800 MPa, *Journal of Physical and Chemical Reference Data*, *25* (6), 1996.

Stainforth, D., A., T. Aina, C. Christensen, M. Collins, N. Faull, D.J. Frame, J.A. Kettleborough, S. Knight, A. Martin, J. Murphy, M., C. Piani, D. Sexton, L.A. Smith, R.A. Spicer, A.J. Thorpe, and M.R. Allen, Uncertainty in predictions of the climate response to rising levels of greenhouse gases, *Nature*, *433*, 403-406, 2005.

Stenvold, T., O. Eiken, M.A. Zumberge, G. Sasagawa, and S. Nooner, High-precision depth and subsidence mapping from seafloor water pressure measurements, in preparation, 2005.

Talwani, M., and M. Ewing, Rapid computation of gravitational attraction of three-dimensional bodies of arbitrary shape, *Geophysics*, *25*, 203-225, 1960.

Wang, Z., M.E. Cates, and R.T. Langan, Seismic monitoring of a CO_2 flood in a carbonate reservoir: A rock physics study, *Geophysics*, *63* (5), 1604-1617, 1998.

Williamson, J.P., R.A. Chadwick, W.J. Rowley, and O. Eiken, Work Area 5 (Geophysics) - Gravity monitoring of the CO_2 bubble, in *SACS-Saline Aquifer CO_2 Storage Phase 2 (SACS2)*, British Geological Survey, Natural Environment Research Council, 2001.

Zweigel, P., R. Arts, A. Lothe, E., and E. Lindeberg, B.G., Reservoir geology of the Utsira Formation at the first industrial-scale underground CO_2 storage site (Sleipner area, North Sea), in *Geological Storage of Carbon Dioxide*, edited by S.J. Baines, and R.H. Worden, Geological Society of London, London, 2004.

Chapter 3

Measuring inflation at Axial Seamount using time-lapse seafloor pressure

3.1 Introduction

Volcanoes are important in the study of the solid Earth because they often exhibit easily observable changes over both short and long time-periods. For example, earthquake swarms associated with the movement of magma within the crust are usually observed in the days and weeks leading up to an eruption. Inflation of the volcano surface can increase dramatically in the days preceding an eruption, due to pressurized magma forcing its way up into the volcano, and an eruption event is often followed by rapid surface subsidence due to the removal of this pressure. Between eruptions, long-term surface deformation signals can provide information about the movement of stored magma within the crust. Geochemical studies can give information regarding the source of an erupted lava. In a sense, active volcanoes provide a window into the crust and mantle of the planet.

Out of over 600 active sub-aerial volcanoes, surface displacement measurements have been made at only several dozen worldwide; furthermore, only about a half dozen of these have been studied for more than a few decades. Only a few of these have eruptive cycles on the scale of our lifetime. It is at this small number of volcanoes that the most has been learned. In order to better understand the evolution of magmatic systems, hundreds of active volcanoes need to be intensely studied during and between eruptive events. Almost all monitoring efforts have been on sub-aerial volcanoes, however an additional resource is the extensive system of volcanoes that are below sea level. In fact, over 75% of the Earth's volcanoes are located on the seafloor, with most of these at mid-ocean ridges. Conventional land-based geodetic observation techniques such as the Global Positioning System (GPS), interferometric synthetic aperture radar (INSAR), and leveling [*Dvorak and Dzurisin*, 1997; *Dzurisin*, 2003; *Segall and Davis*, 1997; *Zebker et al.*, 2000] cannot be used to monitor vertical deformation on submarine volcanoes. Hence, new instruments and techniques need to be developed. The most successful technique to date has been the use of bottom pressure recorders (BPRs), which continuously record ambient pressure as a proxy for seafloor depth [*Chadwick et al.*, 2005 (in press); *Fox*, 1999; *Fujimoto et al.*, 2003; *Watanabe et al.*, 2004]. These measurements use sea level as a datum so that any uplift or subsidence causes a corresponding decrease or increase in measured pressure. Other promising geodetic techniques that have been developed for the seafloor include direct acoustic ranging between pairs of instruments [*Chadwell et al.*, 1999; *Chadwick et al.*, 2002; *Chadwick et al.*, 1999; *Nagaya et al.*, 1999], combined GPS/acoustic positioning of instruments on the bottom from surface ships [*Chadwell et al.*, 1995; *Fujimoto et al.*, 1998; *Fujita et al.*, 2003; *Hildebrand et al.*, 2000; *Osada et al.*, 2003; *Spiess et al.*, 1998], and seafloor gravity measurements with simultaneous pressure measurements [*Eiken et al.*, 2000; *Sasagawa et al.*, 2003]. However, since long-term studies on the seafloor are difficult and expensive, very few submarine volcanoes have been studied intensively. Sections 3.1.2 to 3.1.4 review the research that has been done by others at Axial Seamount and section 3.2 onward describes new work (partly published).

3.1.1 Axial Seamount

Axial Seamount is a volcanic edifice 20-30 km in diameter located on the Juan de Fuca Ridge (JdFR) about 270 miles off the Oregon coast (Figure 3.1). It rises 700 m above the mean elevation of the adjacent JdFR. It is primarily distinguishable by a 3 × 8 km horseshoe shaped caldera trending northwest. The caldera walls rise about 100 m except in the southeast where they gradually shoal, obscuring expression of the caldera wall. Prominent rift zones extend 50 km to the northeast and to the southwest. Dike extrusions on the south rift zone are responsible for burying the south caldera wall [*Embley et al.*, 1990].

The JdFR is spreading at an intermediate rate of 5-6 cm/yr, and has been migrating northwest for at least 10 Myr. A chain of seamounts known as the Cobb-Eikelberg seamount chain extends 450 km from Axial to the northwest on the Pacific plate. K-Ar dating shows that the age of the chain increases in the same direction [*Morgan*, 1972], with the oldest being 8-9 Mya [*Desonie and Duncan*, 1990]. This is consistent with motion of the Pacific plate over a fixed source of increased melt in the upper mantle [*Karsten and Delaney*, 1989].

At Axial Seamount, the seamount and ridge morphology have merged. The volcano appears to lie 15-20 km to the west of the ridge axis, however no clear ridge morphology can be distinguished. It has been speculated that Axial accommodates much of the spreading across the JdFR [*Applegate*, 1990; *Hammond and Delaney*, 1985], however, adjacent JdFR segments (CoAxial to the north and Vance to the south) may still have active spreading. In fact, volcanic activity on the CoAxial segment in 1993 [*Fox*, 1995] suggests that spreading is still occurring there.

Axial Seamount is arguably the most extensively studied seafloor volcano. It has been the focus of intense research since 1987. This is due in part to its proximity to the northwest coast of the United States; however, it is also the most active volcanic site on the Juan de Fuca Ridge. Another key factor is that in 1991 the US Navy allowed NOAA's Pacific Marine Environmental Laboratory (PMEL) access to its SOund SUrveillence System (SOSUS) hydrophone arrays in the northeast Pacific Ocean, enabling scientists to observe earthquakes in the region of Axial as small as magnitude 1.8 [*Dziak and Fox*, 1999a]. The system detects tertiary (T-) wave arrivals, which are seismically generated acoustic waves that can propagate long distances in the ocean sound channel. NOAA/PMEL has maintained a real-time acoustic monitoring system for the SOSUS arrays since 1993. Since that time, most of the earthquake swarm activity along the JdFR has been located at Axial Seamount.

The NOAA Vents program has also maintained seafloor instrumentation to monitor ground deformation within the caldera since 1987. Due to lack of geophysical data at Axial Seamount, the central caldera was chosen by the NOAA

Vents program as the site for long-term monitoring [*Fox*, 1990]. From 1987 to 1992, a Bottom Pressure Recorder (BPR), measuring both water pressure and temperature, was deployed each year within the central caldera [*Fox*, 1993]. During this time, five subsidence events were recorded, lasting from days to weeks with amplitudes of 10 cm or less [*Fox*, 1990; *Fox*, 1993]. However, in 1988, a survey using both seafloor and sea surface gravity data identified the southeastern part of the caldera as the area with the largest negative density contrast [*Hildebrand et al.*, 1990]. This low-density region was interpreted as an indication of the presence of a subsurface magma body. Subsequently, in 1992, Volcanic System Monitors (VSM), which incorporated BPRs, short-baseline tilt meters, current meters, and integrating vertical seismometers, were deployed in the central and southeastern portions of the caldera (Figure 3.1). This allowed surface deformation to be monitored with both pressure and tilt, while simultaneously monitoring effects on the water column. From May 1999 to July 2000, no pressure data were recorded at Axial. In July 2000, BPR monitoring resumed with NeMO2000, which was replaced in 2002 by NeMO2002 (Figure 3.1). NeMO2002 was equipped with an acoustic modem, which was used to transmit data to shore hourly via a buoy-based communication system called NeMO Net [*Chadwick and Stapp*, 2002; see also http://www.pmel.noaa.gov/vents/nemo/realtime/*Stalin et al.*, 2001]. Acoustic extensometer instruments were deployed across the north rift zone in 1996. These instruments measure the round-trip travel time of acoustic pulses between pairs of instruments spaced 100-200 m apart in order to make precise horizontal distance measurements.

Additionally, Axial Seamount was chosen as the location for the New Millennium Observatory (NeMO) [*Embley and Baker*, 1999]. The goal of NeMO is to make multiple types of observations at one location over decadal time periods in order to document changes in interrelated systems. This will increase understanding about the relationships between the movement of magma, eruptions, hydrothermal venting systems, and biological communities at seafloor volcanoes.

The NEPTUNE project [*Delaney and Chave*, 2000] aims to establish a real-time, long-term ocean observatory in the northeast Pacific Ocean by encircling the Juan de Fuca plate with fiber optic and power cables. Node points will allow scientific instrumentation to be connected all along the network. Portions of the network are expected to be operational by 2007. This has the potential to significantly increase data coverage on Axial Seamount as well as the entire JdFR volcanic system.

3.1.2 1998 eruption of Axial Seamount

In January 1998, the most intense swarm of earthquakes observed to date was detected within the summit caldera of Axial Seamount. The swarm lasted 11 days with over 8000 detected earthquakes [*Dziak and Fox*, 1999a]. The activity began in the caldera, then migrated along the south rift zone over the next two days, indicating a lateral magma dike injection.

Pressure records from VSM1 in the central caldera (Figure 3.1) showed coincident subsidence of 3.2 m, suggesting that deflation was due to a decrease in pressure as magma was injected into the southeast rift zone and erupted [*Fox*, 1999]. VSM2, located near the eruption site about 3 km southeast of the caldera center

(Figure 3.1), measured 1.4 m of subsidence. Acoustic extensometer measurements across the northeast rift zone recorded a gradual 9-cm extension beginning in June 1996 (when the instruments were deployed), followed by an abrupt 4-cm contraction at the time of the eruption [*Chadwick et al.*, 1999]. Mechanical modeling of these geodetic data sets indicates that the observed surface deformation can be explained by the removal of 207 × 10^6 m^3 of magma from a point source reservoir located 3.8 km beneath the center of the caldera [*Chadwick et al.*, 1999; *Fox et al.*, 2001]. Additionally, VSM2 was caught in the lava flow from the eruption and measured ~3 meters of rapid inflation followed by subsequent lava drainout [*Chadwick*, 2003; *Fox et al.*, 2001].

A multibeam bathymetric survey was done in May 1998. *Embley et al.* [1999] identified lava flows by differencing this post-eruption bathymetric data with pre-eruption data sets. The detection limit of this technique was 5-15 m in depth change [*Fox et al.*, 1992]. The edges of the 1998 flow were mapped by submersible and ROV in July-September 1998 (Figure 3.1). *Embley et al.* [1999] found a sheet flow more than 3 km in length and 500-800 m wide in the northern part of the south rift zone, and a much smaller flow to the south. The estimated volume of the extrusion from the 1998 eruption is 18-76 × 10^6 m^3 [*Embley et al.*, 1999]. The volume of the dike injection in the southeast rift zone was estimated to be 100-150 × 10^6 m^3, using the length of 50 km (the length of the T-wave swarm migration), a thickness of 1.0 m, and a height of 1-3 km [*Chadwick et al.*, 1999]. This puts the total volume at

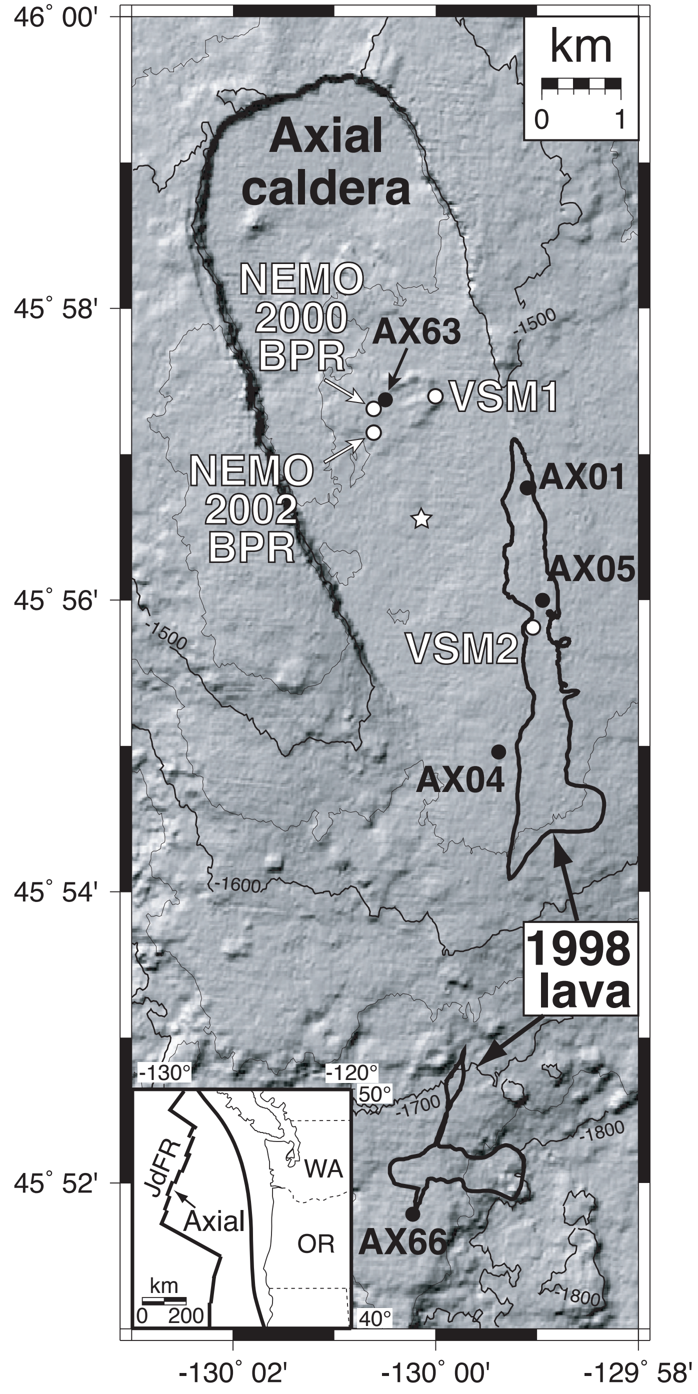

Figure 3.1 Map of Axial caldera showing locations of Bottom Pressure Recorders (BPRs) and Mobile Pressure Recorders (MPR benchmarks) (black dots). The black outlines indicate the 1998 lava flows and the white star shows the location of the best fitting Mogi point source for the MPR measurements. Inset shows the location of Axial Seamount relative to the JdFR. (From *Chadwick et al*., 2005)

118-226 × 10^6 m^3, which is consistent with the mechanical model of *Chadwick et al.* [1999] (207 × 10^6 m^3) based on surface deformation measurements.

Water temperature anomalies of 0.6 ºC up to 115 m above the bottom were observed on moorings along the eruption fissure [*Baker et al.*, 1999]. The temperatures remained high for about 5 days, then declined over the next two weeks. In February 1998, the NOAA Vents funded Axial Response Team (ART-1) mounted a rapid response cruise to investigate water column expressions of the volcanic event. They found increased levels of microbial biomass in the hydrothermal plumes [*Cowen et al.*, 1999], water-column chemical changes [*Lupton et al.*, 1999; *Resing et al.*, 1999], iron and sulfur enrichment in the hydrothermal plumes at Axial Seamount [*Feely et al.*, 1999], and widespread thermal anomalies due to the eruption [*Baker et al.*, 1999].

3.1.3 Post-eruption BPR measurements

After the 1998 eruption, VSM1 continued recording for about 10 months and VSM2 continued recording for about 20 months [*Chadwick et al.*, 2005 (in press)]. Immediately after the eruption-related *deflation*, a signal consistent with long-term *inflation* was recorded on the two instruments. VSM1 BPR measured a change in pressure corresponding to an uplift rate of ~101 cm/yr and VSM2 BPR measured a change corresponding to a rate of ~22 cm/yr [*Chadwick et al.*, 2005 (in press)]. These rates were initially high and decreased with time, consistent with patterns of inflation seen following eruptions on land [*Dvorak and Dzurisin*, 1993; *Dvorak and Okamura*, 1987; *Lu et al.*, 2003; *Sturkell et al.*, 2003].

There was a gap in the BPR data from May 1999 to July 2000, while new instruments were being completed. The NeMO2000 BPR was in place for 2 years until July 2002. It was replaced by NeMO2002 BPR, which was in place until July 2004. Both of these instruments recorded an apparent inflation rate of ~15 cm/yr in the center of the caldera [*Chadwick et al.*, 2005 (in press)].

The pressure sensors used in the BPR instruments are Paroscientific Digiquartz pressure transducers, model 410K. More detail is given about these gauges in the following sections. At a depth of ~1500 m, these gauges are subject to long-term linear drift in pressure that can yield inferred height changes up to 23 cm/yr [*Chadwick et al.*, 2005 (in press)]. The exact rate of drift is specific to each sensor and stabilizes during the first few weeks of deployment while the sensor equilibrates [*Eble et al.*, 1989; *Fox*, 1990]. Unfortunately, the range of potential drift rate encompasses the observed rates of inflation seen from NeMO2000 and NeMO2002 (15 cm/yr) [*Chadwick et al.*, 2005 (in press)]. Therefore, these instruments are very good for observing sudden or short period events, but are inadequate for observing long-term or gradual deformation.

3.2 Relative pressure measurements at Axial Seamount

Since 1999, an independent method to measure gradual volcanic inflation on the seafloor has been under development [*Chadwick et al.*, 2005 (in press)]. The technique is analogous to optical leveling or time-lapse gravity surveys on land, but involves making campaign style pressure measurements on an array of fixed seafloor benchmarks with a Mobile Pressure Recorder (MPR). The advantage of this technique is that drift in the pressure gauges can be calculated by assuming no relative deformation occurs during the survey (2-3 days). This eliminates the need to separate long-term instrument drift from gradual volcanic deformation. The disadvantage of this technique is that the all measurements are made with respect to a reference benchmark, which is assumed to be stationary over time. MPR measurements have been made at Axial every year since 2000. This technique was modeled after *Sasagawa et al.* [2003], who used repeated pressure and gravity measurements on the seafloor over an oil and natural gas field to examine seafloor subsidence and rise of the gas/water contact surface within the reservoir. All of the measurements at Axial Seamount are made with respect to a reference benchmark (AX66) located ~10 km south of the caldera center (Figure 3.1).

In the following sections, I will discuss the design of the MPR instruments, the data processing, and sources of error and uncertainty. I also will discuss the results of mechanical deformation models and the implications to the behavior of the volcano.

3.2.1 MPR design and methods

The MPR instrument consists of two redundant Paroscientific Digiquartz model 410K pressure transducers, which have a range of 0-10,000 psi (~0-6900 m), along with a micro-controller and support electronics, enclosed in a deep sea pressure housing. These transducers utilize an oscillating quartz crystal beam that is mechanically connected to a C-shaped Bourdon tube (Figure 3.2). When pressure enters the Bourdon tube, the tube tends to straighten out. Thus, changes in fluid pressure are converted into a change in the axial compressive load on the oscillating beam, which in turn alters the natural vibrational frequency of the beam. [*Boss and Gonzalez*, 1994; *Eble and Gonzalez*, 1991; *Wearn and Larson*, 1982]. Since the frequency of the beam oscillation is also dependent on the temperature, accurate temperature measurements are made inside the housing of the gauge. Bourdon tube sensors of this type have been shown to have a lower drift rate, improved long-term stability, and significantly greater accuracy than earlier types of pressure sensors [*Watts and Kontoyiannis*, 1990; *Wearn*, 1985; *Wearn and Larson*, 1982].

Having two gauges within the pressure housing increases the number of measurements made, making efficient use of ship time, and decreasing the uncertainty in the measurements. The MPR instrument is small enough to be carried and deployed by ROV, and direct electrical connection to the ROV provides power and data transmission. Prior to 2004, the data could not be viewed in real-time by an observer on the ship; in 2004, however, an interface that plots the data in real time was made using Labview. This allowed a higher level of quality control during the survey. Another addition to the instrument package in 2004 was a digital two-axis inclinometer, which was used to measure instrument tilt and rotation.

Each pressure measurement involves placing the MPR on the benchmark using the ROV's manipulator arm (Figure 3.3) and recording data for 20-30 minutes. This allows plenty of time for the gauges to stabilize. Making measurements at all 5 benchmarks over a short period of time (days) eliminates the ambiguity of long-term sensor drift. Short-term drift is quantified and accounted for by making multiple measurements on each benchmark during a survey (under the assumption that the

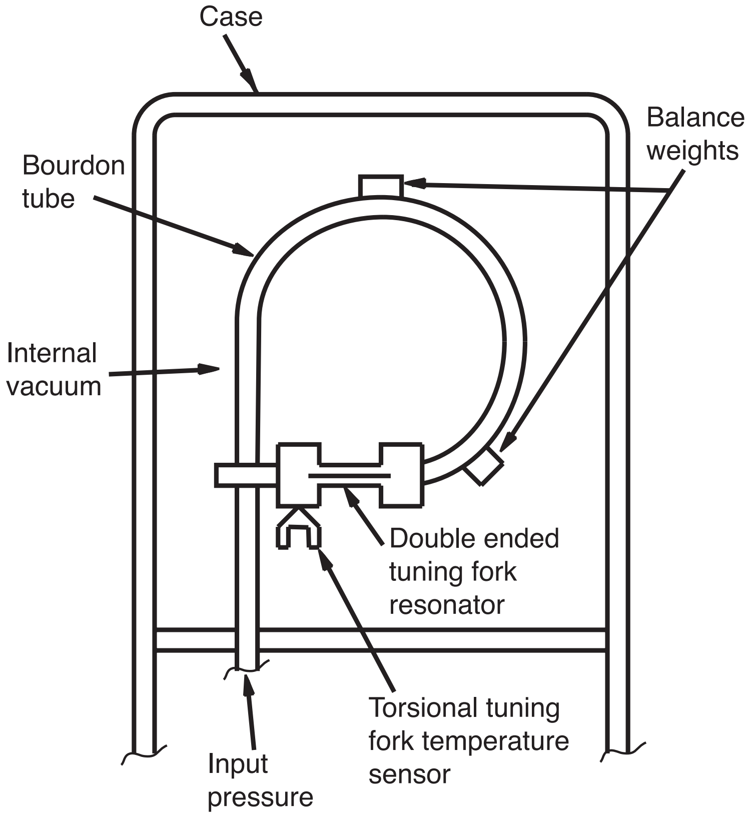

Figure 3.2 Internal design of the Paroscientific model 401K pressure transducer with a Bourdon tube design. The gauge is temperature corrected using the torsional tuning fork temperature sensor (after http://www.paroscientific.com).

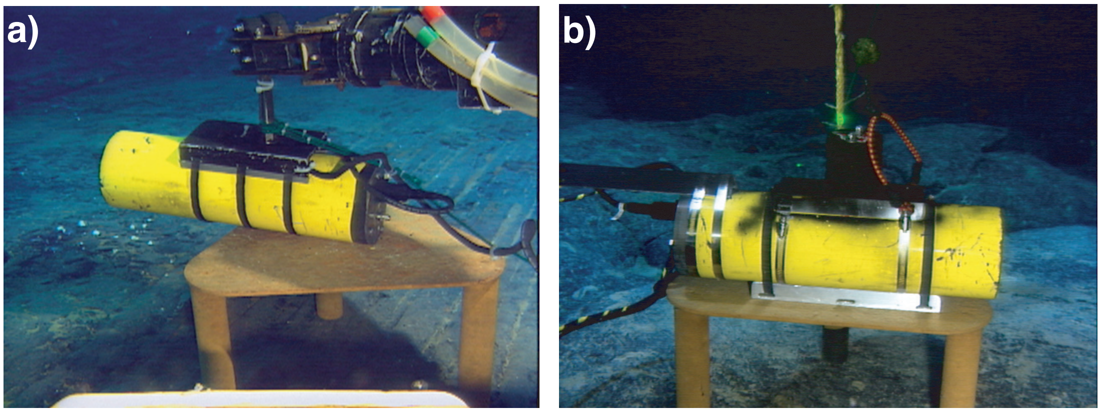

Figure 3.3 Photographs of MPR on a triangular benchmark. (a) MPR held by the ROPOS manipulator arm during a pressure measurement (2000-2003). (b) MPR released by the ROV during a pressure measurement in 2004.

benchmark depths don’t change within the short duration of the survey). The number of repeat measurements has increased with time, as the method has been refined.

The benchmarks used at Axial are triangular plates made out of galvanized steel that weigh 20 pounds in water. They are 46 cm on a side with three 25 cm tall legs (Figure 3.3). They are located on relatively flat stable areas of the seafloor, and are not likely to be disturbed between surveys due to the benign environment (except in the case of a volcanic eruption).

3.3 MPR data processing and error analysis

Processing the data prior to 2004 was a tedious procedure because of imperfections in the format of the raw data. Data recording began at the start of each ROV dive and ended when the dive was over. In each year, there were 3-6 days of 0.1 Hz data. The format of the data is shown in Table 3.1. The time is in seconds relative to an arbitrary start time. However, two thirds of the time, there is no time stamp, and whenever there is one, it is often on the same line as another data field or split between two lines. Additionally, sometimes gauge 1 responded first and sometimes gauge 2 responded first. About 10% of the time, a single line of data is randomly repeated. This non-uniform format made the data extremely difficult and time consuming to deal with.

Each record was filtered and organized using a series of Unix ‘sed’ commands, however, each record still had to be edited by hand. Missing time values were added by interpolating between the ones that did exist. Unfortunately, there were still regular 10-30 second long offsets in the time, indicating segments of missing data.

Occasionally, large jumps in the time value, up to ± 30,000 seconds occurred in the middle of a record for no apparent reason. This was corrected for by assuming no data were missing, and adjusting the time accordingly. The arbitrary time value was referenced to an absolute time value at the start of each data file and at the start of a benchmark occupation. Data gaps and jumps in the time value caused errors of up to 2 minutes to accrue during an ROV dive lasting ~24 hours. The time on the benchmark could be picked visually from the pressure record, since the pressure fluctuations were several orders of magnitude less on the benchmark where the gauge was held motionless (Figure 3.4). The duration of the benchmark occupations were taken from start and end times recorded in an excel spreadsheet. This duration was often shorter than the apparent benchmark occupation time (obtained visually from the pressure data) by up to 2 minutes. Coupled with the offset errors discussed above, this causes an uncertainty in the start time of a benchmark occupation of up to 2 minutes. Since the maximum tidal rate of change is about 1 cm/min, this leads to an error of at most 2 cm. This tide correction is discussed in more detail in section 3.3.2 below.

Table 3.1 2000-2003 data format

Data field	**Explanation of the data field**
*030014174	Time in arbitrary seconds
*00012246.181	Unit 1 pressure in psi
*000129.569807	Unit 1 pressure period
*00022245.676	Unit 2 pressure in psi
*000229.508625	Unit 2 pressure period
*00014.509	Unit 1 temperature in ºC
*00015.8795849	Unit 1 temperature period
*00024.855	Unit 2 temperature in ºC
*00025.8827476	Unit 2 temperature period

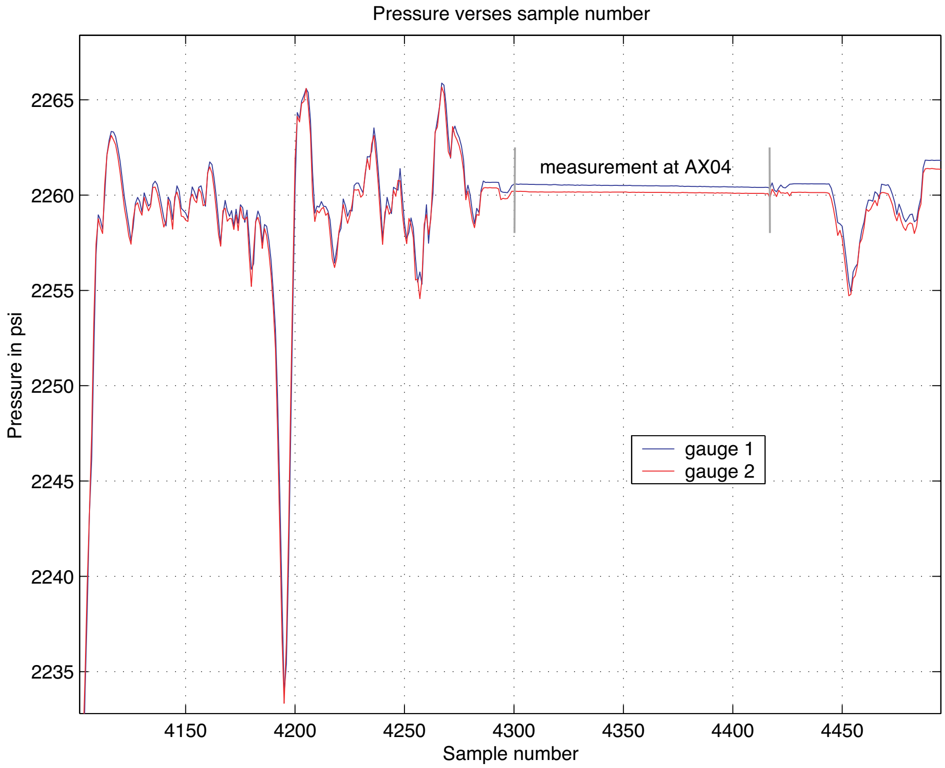

Figure 3.4 A pressure record showing the approach and measurement at benchmark AX04 during the 2001 survey. The record during the measurement (indicated by the grey lines) is notably quieter than elsewhere, allowing the time to be picked out visually. The X-axis indicates sample number since the beginning of the dive, with 10 seconds between samples.

In 2004, a new microprocessor and a digital inclinometer were put into the MPR instrument package and a Labview interface was made for data recording, allowing the data to be more reliably parsed and recorded. A data stream consisting of gauge 1 and gauge 2 pressure and temperature, x and y tilt values, and an absolute time stamp from the computer, was recorded at 1.33 Hz. The new software also allowed the operator on the ship to start a new file for each benchmark occupation. These changes eliminated the intensive data processing and timing ambiguities and allowed the data to be plotted and observed in real-time on board the ship, thus increasing the amount of quality control on the measurements.

Once the data were organized, the data reduction procedure was basically the same for all five years. First, the data were converted from pressure to depth and tide corrections were made. To eliminate gauge equilibration effects, the last third of each 20-30 minute record was then averaged to get a depth value for that benchmark occupation. The resulting depth values were corrected for linear drift of the gauges based on the repeat occupations of the individual benchmarks. Finally, the results of the two gauges were averaged to get the depth of each occupation. The mean of the repeat benchmark occupations for each site was taken as the benchmark depth for that year. These steps, along with the errors and uncertainties associated with each, are described in more detail in the following sections. (Note that the error budget presented here is slightly different from that of *Chadwick et al.*, [2005 (in press)].)

3.3.1 Depth conversion

The most accurate way to convert pressure to depth in the ocean is to first measure local seawater properties with a CTD (conductivity, temperature, density), then use this data in a formula derived by Fofonoff and Millard [1983], which is accurate to 10 cm in absolute depth over the full ocean range:

$$z = D/\overline{g} + \Delta D/9.81 \qquad 3.3.1.1$$

where z is the depth in meters, D is the geopotential distance at a salinity $S = 35$ psu and $T = 0$ ºC fitted to a fourth order polynomial in pressure, $\overline{g}$ is the average gravity, and ΔD is the geopotential anomaly. This first term in 3.3.1.1 is the standard ocean depth formula and is good to about 2 m over full ocean depth [*Fofonoff and Millard*, 1983]:

$$D = 9.72659 P_g - 2.512 \times 10^{-5} p_g{}^2 + 2.279 \times 10^{-10} p_g{}^3 - 1.82 \times 10^{-15} p_g{}^4, \qquad 3.3.1.2$$

$$\overline{g} = g(\theta) + \frac{1}{2}\gamma p_g, \qquad 3.3.1.3$$

and

$$g(\theta) = 9.780318\left(1.0 + 5.2788 \times 10^{-3} \sin^2\theta - 2.36 \times 10^{-5} \sin^4\theta\right) \qquad 3.3.1.4$$

where p_g is the gauge pressure in decibar (the measured absolute pressure from the gauges minus the atmospheric pressure at the sea surface), $g(\theta)$ is the latitude dependent gravity value at the sea surface, and $\gamma = 2.226 \times 10^{-6}$ m/s^2/dbar is the gravitational gradient in seawater. (Note that 1 dbar is approximately equal to 1 m of depth.)

The geopotential anomaly, ΔD, takes into account the salinity, temperature, and depth data from the CTD to correct for the assumption in the standard ocean depth model that the salinity and temperature are constant at a salinity $S = 35$ psu and $T = 0$ $^{\circ}$C:

$$\Delta D = \int_0^p \left[v_s(S,T,p) - v_s(35,0,p)\right]dp \qquad 3.3.1.5$$

where v_s is the specific volume, which can be calculated from the equation of state for seawater [*Fofonoff*, 1985; *Fofonoff and Millard*, 1983]. Alternatively, Leroy and Parthiot [1998] provide corrections terms, $\Delta D/9.81$, for various areas of the world's oceans. The correction term

$$\Delta D/9.81 = p_g/(p+100) + 5.7 \times 10^{-4} p_g \qquad 3.3.1.6$$

was found to represents all open ocean situations within ± 0.8 m in absolute depth.

Since no CTD measurements were available at Axial Seamount during the pressure surveys each year, pressure values in psi were converted to depth in meters using an empirically derived polynomial [*Mark Zumberge*, private comm.]:

$$z = 0.68576p - 1.3131\times10^{-6}p^2 + 2.191\times10^{-11}p^3, \qquad 3.3.1.7$$

where z is the depth in meters and p is the absolute pressure in psi. This formula is based on measurements made at a specific time and place in the Pacific Ocean (at about 30 ºN) and is consequently a poor approximation if absolute depths are sought.

The absolute depth values obtained from the pressure measurements depends on which of the two methods of conversion discussed above is used. In fact, it is informative to compare the two approaches. The four benchmarks within the caldera of Axial Seamount (AX63, AX01, AX05, and AX04) are at depths ranging from 1523-1534 m. The reference benchmark (AX66) is at a depth of 1723 m, making the relative depths on the order of 200 m. At a pressure of about 1500 dbar (1psi = 0.6894757 dbar) the difference between our empirical polynomial and the standard ocean model from *Fofonoff and Millard* [1983] is ~3.5 meters in absolute depth and ~39 cm in depth relative to AX66. Adding the correction from Leroy and Parthiot [1998] cuts the difference to ~1.8 meters in absolute depth and ~19 cm in relative depth. This difference is due primarily to the lack of a gravity correction with latitude in our polynomial. However, what we are really looking for at Axial are the relative changes in benchmark depth over time due to the movement of magma within the volcano, which are expected to be on the order of 10-20 cm/year based on the BPR measurements of *Chadwick et al.* [2005 (in press)]. For a change of 20 cm within the caldera with respect to the reference benchmark, the difference between the two depth estimates is about 0.02 cm, which is 2 orders of magnitude below the expected level of detection for the instrument. Therefore, as long as our method of depth conversion is consistent, and as long as the temperature and salinity profiles are constant, the errors in the time-lapse changes are small.

It has long been known that changes in atmospheric pressure cause corresponding changes in the local sea level due to pressure loading [e.g. *Wunsch and Stammer*, 1997]. This is known as the inverted barometer (IB) effect. Theoretical and experimental results indicate that due to the IB, atmospheric pressure changes induce little or no pressure changes on the seafloor [e.g. *Brown et al.*, 1975; *Wunsch and Stammer*, 1997]. For this reason, the atmospheric pressure was not taken into account when doing the pressure to depth conversions each year. The variation in atmospheric pressure at sea level is at maximum about 2%, or ± 0.3 psi [*Gill*, 1982]. Without the inverted barometer, the effect on absolute benchmark depths for 0.3 psi atmospheric pressure change would be ± 20.5 cm. *Brown et al.* [1975] did observe seafloor pressure fluctuations on the order of 2 mbar (approximately 2 cm) occurring with a period of about a day which they attributed to wind on the surface. This has not been observed in the BPR data.

Additionally, mixing in the upper layers of the ocean can cause the density to vary due to both temperature and salinity changes. The affect of this is the same as increasing or decreasing the gauge pressure, and hence the apparent depth. A density change of 5 kg/m^3 over the entire top 1000 m of the ocean causes a shift in the apparent absolute depth of ± 5 m, which in turn causes a relative depth error of ± 0.49 cm. A density change of this magnitude and extent is more than is observed in 98% of the world's oceans [*Gill*, 1982]. Combining all of these sources of error gives an uncertainty in the depth conversion of ± 0.5 cm (Table 3.2).

Table 3.2 Error budget for the MPR measurements

Error source	**Depth uncertainty (cm)**			
	2000	**2001, 2002**	**2003**	**2004**
Inherent precision of the gauges	0.2	0.2	0.2	0.2
Background noise	0.6	0.6	0.6	0.4
Calibration uncertainty	0.1	0.1	0.1	0.1
Tide correction uncertainty	2.0	2.0	2.0	1.2
Drift correction	5.0	0.7	0.7	0.3
Depth conversion uncertainty	0.5	0.5	0.5	0.5
Rotational uncertainty	6.2	6.2	1.8	0.1
RMS sum of errors	**8.3**	**6.3**	**2.9**	**1.5**
Observed repeatability	15.0	5.6, 5.1	3.2	0.9

3.3.2 Tide corrections

Once the pressure measurements were converted to depth, tidal corrections were made. Tidal data were obtained from the BPRs that were deployed in the caldera center [*Chadwick et al.*, 2005 (in press)] from 2000 until 2004. With this data we were able to correct the 2000-2003 data series with measured tide values. The 2004 data were corrected using a tide model computed using SPOTL [*Agnew*, 1996]. The error in the tide model can be estimated by comparing the predicted tides with the measured tides for the previous years. The difference between the two, indicate that about ± 1.2 cm of error could be introduced into the 2004 data by using the tidal model. The uncertainty in the tide correction from 2000-2003 comes from uncertainty in the absolute time of measurement (discussed above) and is ± 2.0 cm (Table 3.2).

If the tide correction is applied correctly, the resulting 20-30 minute depth record should appear flattened, with no slope. However, there is often a period of 10-15 minutes in which the gauges appear to settle or recover in response to movement and handling by the ROV. Therefore, for each gauge, the average value of the last one-third of each record was chosen as the depth for that occupation.

3.3.3 Drift corrections

Next, the average depth at each benchmark (from all occupations) was calculated and subtracted from each depth measurement at that benchmark, forcing all of the benchmarks to have a zero-mean depth. Then the median time was subtracted from the measurement times at each benchmark. This puts all the measurements at different stations in the same reference frame so they can be readily compared (Figure 3.5). A least squares fit to the resulting data points for each gauge gave a linear drift value for that survey year. The calculated drift rates each year ranged from 1-8 cm/day, which are much higher than observed for the same type of gauges when used as BPRs (less than 0.06 cm/day) [*Chadwick et al.*, 2005 (in press)]. This is because the sensors in the MPR are subject to highly variable conditions during ROV motions and manipulator handling. The final depth for each benchmark occupation is the average of the drift-corrected depths from both gauges.

The uncertainty in the drift correction can be estimated by calculating the formal uncertainty in the linear least squares fit for drift rate, then multiplying that by the duration of the survey. This is an upper bound on the likely error in the drift correction. This is shown for each year in Table 3.2.

After correcting for drift, the average depth values at all repeated benchmarks (in that year's survey) are subtracted from the individual measurements. The deviation from zero of these residual values indicates the noise in that year's survey. The standard deviation of the residuals is adopted as the error for a given survey, since this is the best estimate of the repeatability of the measurements (Table 3.2).

3.3.4 Gauge calibration, inherent precision, and background noise

Slight changes in the mechanical properties of the 410K pressure gauges over time require that they be periodically recalibrated. A calibration coefficient α relating the true pressure to the measured gauge pressure is defined by the relation $P_{meas} = (1+\alpha)P_{true}$. Calibrations in the lab are done using a dead weight calibrator in a temperature-controlled bath. Figure 3.6 shows the results of the 2003 calibration for each gauge. The 2003 calibration gave coefficients of $\alpha = 10 \times 10^{-5}$ for gauge 1 and $\alpha = -5 \times 10^{-5}$ for gauge 2 (Figure 3.6a). The formal uncertainty in the slope (α) in Figure 3.6a is $\sim 5 \times 10^{-6}$ for both gauges. This indicates how well a line fits the data, given the uncertainty in each data point. The uncertainty in each data point is simply the standard deviation of the pressure time series that was averaged in order to get that point. The uncertainty in depth over the 200 m range of the benchmarks at Axial is

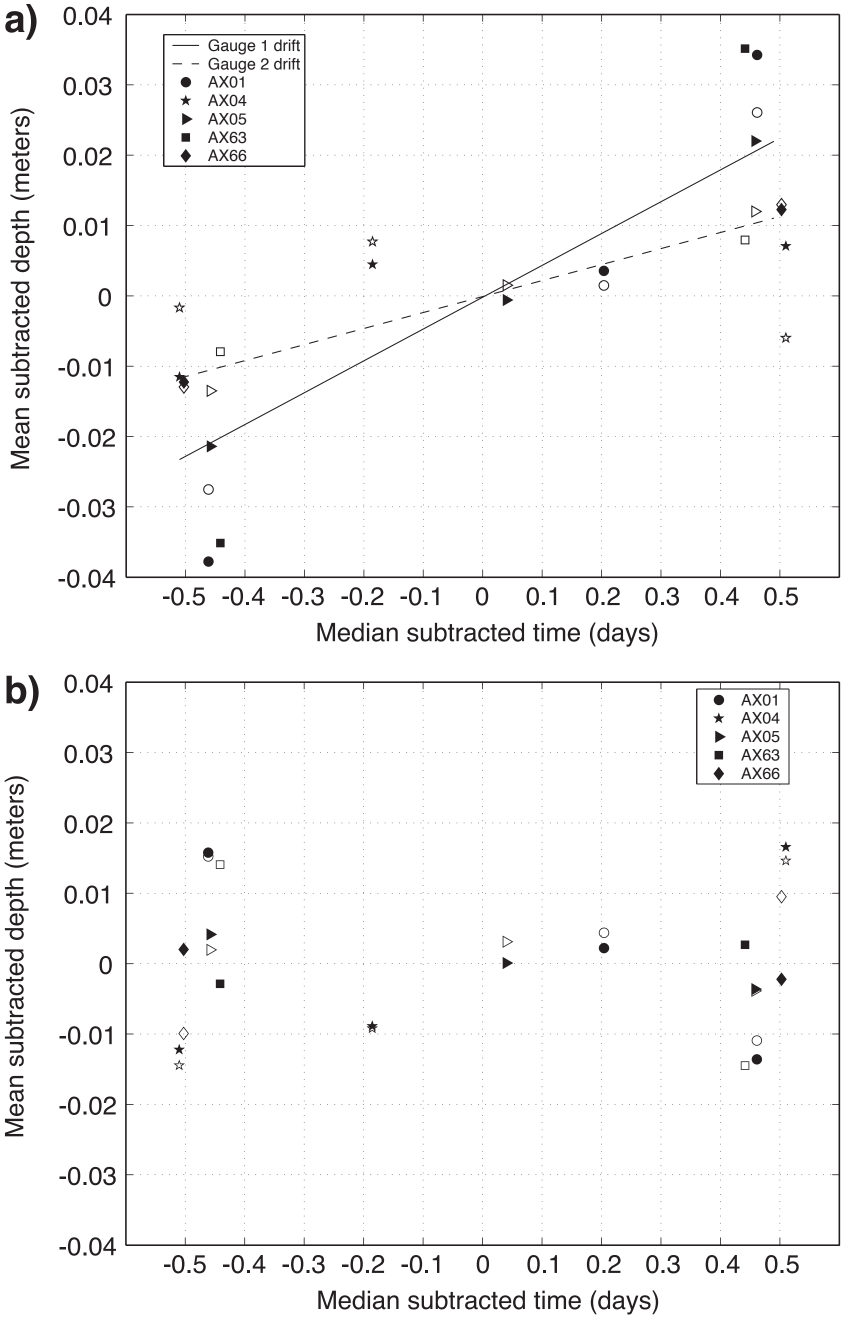

Figure 3.5 (a) Plot of the linear drift rate calculated from the depth values from repeated stations during the 2004 MPR survey. For each benchmark, the mean is subtracted from the all the measurements at that benchmark and the median time of measurement is subtracted. (b) Plot of the scatter after a linear drift is removed from the 2004 data. The standard deviation of the scatter is 0.9 cm. Gauge 1 is represented by the unfilled symbols and gauge 2 is represented by the filled symbols. (From *Chadwick et al.*, [2005 (in press)])

found by multiplying the calibration slope uncertainty (5×10^{-6}) by the depth range (200 m). From this, the calibration uncertainty was determined to be 0.1 cm.

After subtracting the gauge pressure from the absolute calibration pressure in 2003, the RMS scatter of the residuals is ~0.04 psi over a 4000 psi range (Figure 3.6b). This is an accuracy of 0.001%, which is a factor of 10 better than the manufacturer specifications. The depth range at Axial is close to 200 m, suggesting that the inherent precision of the sensors for the surveys is about 0.2 cm (Table 3.2).

The background noise in the sensors is estimated by calculating the average standard deviation for each occupation time series. The uncertainty was 0.6 cm from 2000-2003 and 0.4 cm 2004. The reduction in 2004 probably reflects less coupling noise between the ROV and pressure gauges, since the ROV released the MPR in 2004, but not previously.

3.3.5 Rotational uncertainty

Laboratory tests with the MPR instrument identified another source of error that had been overlooked in the first few years of the study. The output of the Paroscientific pressure gauges was found to depend strongly on their orientation relative to the Earth's gravitational field (Figure 3.7a). Small differences in the orientation of the pressure sensor about the long axis from one measurement to another can lead to large apparent depth differences, even though the actual depth of the sensor has changed by millimeters at most. Figure 3.7a shows the sinusoidal variability of the gauges with rotation. This was a major source of error from 2000-2003, since during those survey years the MPR was oriented by eye so that the ROV

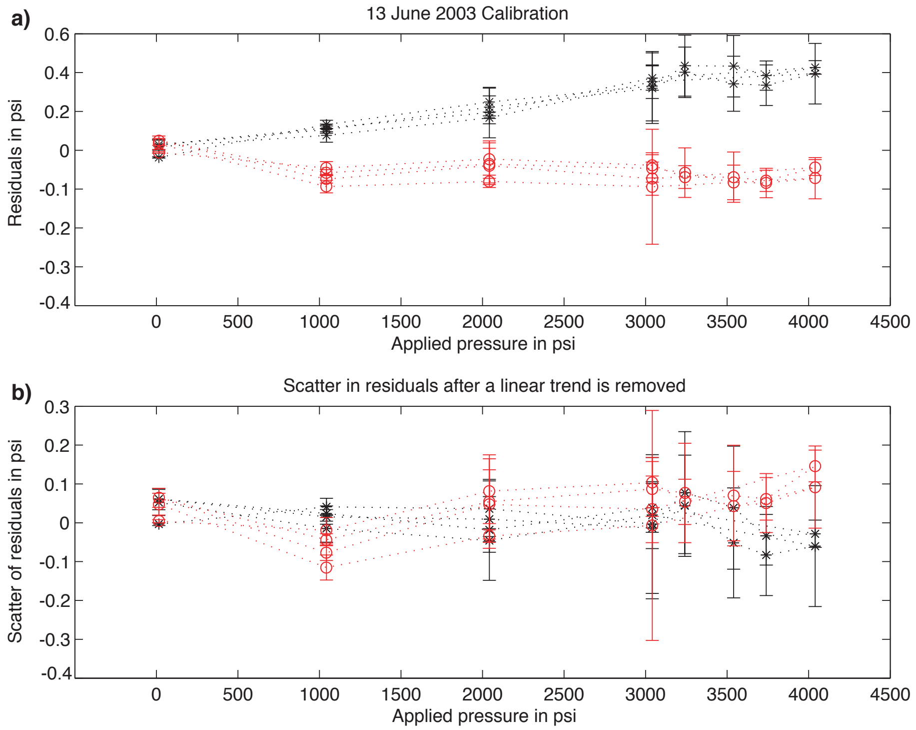

Figure 3.6: Plots showing the results of the 2003 calibration. Gauge 1 is red and gauge 2 is black. (a) The residual pressure (observed gauge pressure minus applied absolute pressure) versus the applied pressure. The slope of the linear trend of the residuals indicates the calibration coefficient, α. (b) The scatter of the data after a linear trend has been removed from each gauge. The scatter of the gauges over the 4000 psi range is about 0.04 psi.

handle appeared to be vertical, with the long-axis of the MPR flush with the top of the benchmark (Figure 3.3b). Based on photos of the MPR on the benchmarks, we estimate that the MPR was typically within 10° of vertical. The actual orientation of the gauges within the MPR is not known from 2000-2002. The amplitude of the rotation effect for gauge 1 is $A = 0.957$ psi and for gauge 2 is $A = 0.681$ psi (Figure 3.7a). For the purposes of assigning an uncertainty to the data, we take the average of the two gauges, $\overline{A} = 0.819$. To find the average error that a 10° rotation would cause, we need to first find $\left.\frac{dp}{d\theta}\right|_{RMS}$ for a sinusoid. This is done by computing the RMS value of a sinusoid (RMS = 0.7) and multiplying that by $\overline{A}$, yeilding $\left.\frac{dp}{d\theta}\right|_{RMS} = 0.5733$ psi/rad. This means that for $d\theta|_{RMS} = 10°$ or 0.017 rad, $dp|_{RMS} = 0.097$ psi, which translates to 6.2 cm. This number is what we use for the rotation uncertainty from 2000-2002 (Table 3.2).

Luckily, the relative orientations of the gauges were known during the 2003 survey, based on laboratory tests after the survey. Because the phase of both gauges is known relative to one another, and because the amplitude of the rotation sensitivity is different for the two gauges, it is possible to back calculate a rotation angle for each measurement in 2003 and then correct for it. To do this, the difference between the two gauges was calculated for each benchmark occupation. Based on a comparison between this difference and the difference between the two laboratory determined sensitivity curves in Figure 3.7a, a rotation angle was assigned to each gauge and a depth correction was made. This correction shifted the benchmark depth values by up to 12 cm relative to the reference, and reduced the observed scatter in the data from 6.6 cm to 3.2 cm. If this correction is valid, the value of the gauge difference should increase as the distance from the mean benchmark depth value increases (Figure 3.7b). The uncertainty of this correction was estimated by calculating the standard deviation of the residuals after a linear fit was subtracted from the data, shown in Figure 3.7b. This value, 1.8 cm, indicates the accuracy of the correction and was taken as the rotational uncertainty for 2003 (Table 3.2).

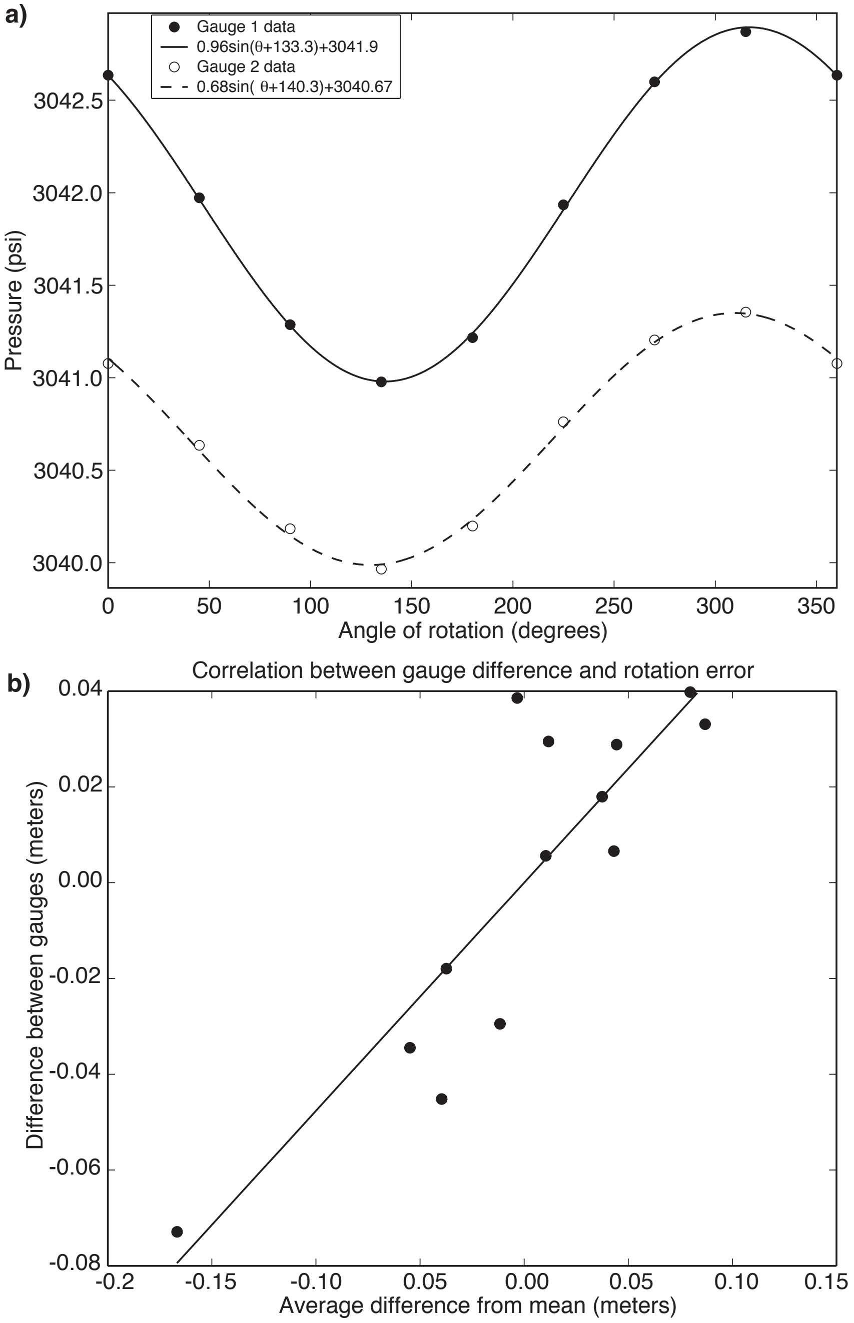

Figure 3.7 (a) The results of a laboratory test with the MPR held at a constant pressure of 3041.64 psi, which shows the effect that rotation has on the output from the pressure gauges. (From *Chadwick et al.*, [2005 (in press)]) (b) The correlation between gauge difference and average difference from the mean benchmark depth. Since the amplitude of the rotation effect is different for each gauge, the difference between them should increase as the difference from the average depth at the benchmark increases.

Table 3.3 Characteristics of MPR surveys in different years and residual errors (from *Chadwick et al.*, 2005). The computed error is the standard deviation of the residuals.

Year	Sensor serial numbers (gauge1/ gauge2)	Number of transects	Number of repeat measurements at each benchmark					Computed Error (cm)
			AX63	AX01	AX05	AX04	AX66	
2000	43886/ 53344*	1	1†	1	1	1	2†	15.0
2001	43526/ 43535	2	2†	1	1	2	1	5.6
2002	62201/ 43535	3	2	3	3	2	2†	5.1
2003	62201/ 43535	3	2	3	3	3	2†	3.2
2004	62201/ 43535	3	2	3	3	3	2	0.9

* Pressure gauge SN 53344 did not give reliable results in the 2000 survey.
† During the first measurement, pressure gauges probably were not thermally equilibrated.

Based on the effects of gauge rotation, the following steps were taken in 2004 to make the exact position of the instrument more repeatable at each benchmark: 1) a flat plate was attached to the bottom of the MPR so that the ROV could release it during measurements (Figure 3.3b), 2) the MPR was positioned in the same orientation during each occupation at a given site, 3) tilt sensors were added to the MPR and the tilt was recorded and displayed in real-time on the ship during measurements, and 4) the pressure gauges were oriented inside the MPR so that their rotational sensitivity was minimized. In this way, the rotational uncertainty was reduced to 0.1 cm (Table 3.2) based on the scatter of the recorded tilt data.

3.3.6 Total error budget

The repeatability of the MPR measurements has improved as sources of error have been progressively identified and eliminated each year. Additionally, the confidence of our measurements has increased with time, as the number of repeat measurements has increased. The standard deviations of the residuals were 15 cm in 2000, 5.6 cm in 2001, 5.1 cm in 2002, 3.2 cm in 2003, and 0.9 cm in 2004. The errors in 2000 were much higher because only one of the two pressure gauges worked reliably that year and repeat measurements were made at only 1 of the 5 benchmarks (whereas they have been made at all benchmarks since 2002; Table 3.3); however, another set of repeat measurements made during a different dive on the Cleft segment of the JdFR helped to constrain the drift and repeatability somewhat. The error budget for the MPR measurements is outlined in Table 3.2.

3.3.7 Reference benchmark uncertainty

There appear to be correlated year-to-year depth variations in the depth estimates. For example, in Figure 3.7 all the depth estimates in 2002 lie significantly above the best fitting line, and the points in 2001 and 2003 fall below the line. It is possible that these variations reflect systematic errors in the data processing or data collection procedure rather than actual seafloor deformation. Benchmark instability can be ruled out, because at each site, the benchmarks are stable and the underlying seafloor lavas are solid and relatively flat (Figure 3.3). Other possibilities investigated relate to the fact that there is a 200 m depth difference between the reference benchmark (AX66) and the others inside the caldera. For example, if changes in water

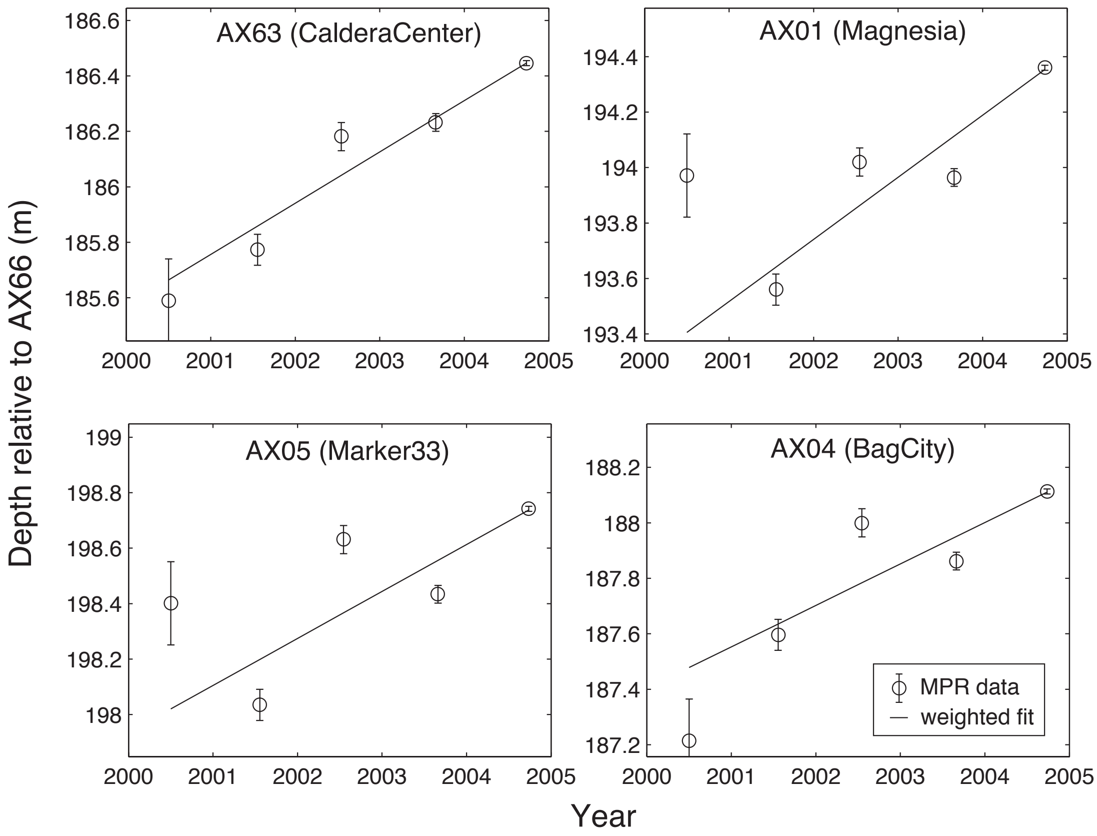

Figure 3.8 MPR results from 2000-2004 showing the measured depth changes with time relative to AX66 (its actual depth is –1723 m). The average inflation rates are slopes of the weighted least square fit lines. (From *Chadwick et al.*, [2005 (in press)])

density occurred from year to year within that 200 m depth interval between 1500-1700 m in which the benchmarks lie, it might introduce an error in conversion from pressure to depth (changes in water properties above 1500 m would affect all measurements equally). An error of 40 cm in depth over 200 m would result from a density change of about 0.2%. The equation of state of seawater [*Fofonoff*, 1985] shows that a density change of this amount (~2 kg/m^3) at that depth would require a change in temperature of 8 ºC, or a salinity change of about 2 PSU. However, changes of this size are several orders of magnitude greater than what is observed during annual conductivity, temperature, and depth (CTD) profiles in the area [*E. Baker*, personal communication, 2004].

Other potential sources of error are time variation of gauge calibration or a depth dependent rotational sensitivity. As shown in section 3.3.4, a calibration coefficient α relating the true pressure to the measured gauge pressure is defined by the relation $P_{meas} = (1 + \alpha) P_{true}$. In reality, the value of α for a gauge changes very little with time. The 2001 calibration showed coefficients of $\alpha = 12.5 \times 10^{-5}$ for gauge 1 and $\alpha = -8.3 \times 10^{-5}$ for gauge 2. The 2003 calibration gave coefficients of $\alpha = 10 \times 10^{-5}$ for gauge 1 and $\alpha = -5 \times 10^{-5}$ for gauge 2 (the change α in gauge 1 was due to switching gauges rather than from drift in the calibration factor) (Figure 3.6). Relating this to depth change gives a maximum depth error of 0.5 cm for gauge 1 and – 0.7 cm for gauge 2 if the calibration is not taken into account (it wasn't in 2000, and for gauge 1 in 2002). The same type of analysis for gauge orientation as a function of depth was tested in the lab, but the amplitude of the rotation effect was found to be relatively insensitive to the applied pressure. Therefore, none of these possible error sources are enough to explain away the large apparent depth differences observed from year-to-year.

After carefully examining the data from each year, another source of error that contaminated some of the measurements from 2000-2003 became apparent; the pressure sensors do not become thermally equilibrated until they have been at ambient seafloor temperature (~3 °C) for about 2 hours. This means that the first pressure measurements during each dive were made before the gauges had equilibrated, contributing an error that is difficult to quantify. The solution to this problem (implemented in 2004) is to either wait for 2 hours before making the first measurement, or to thermally equilibrate the pressure sensor in an ice bath on deck before each dive.

Compounding this problem, the first measurements in 2000-2003 were usually made at the reference benchmark (AX66). Additionally, the reference benchmark was never measured more than twice per survey. Since both measurements were also affected by an unknown gauge rotation (as discussed above), the second measurement provided little constraint on the uncertainty of that benchmark. Together, these two factors made the possible error in the reference benchmark larger than the survey repeatability suggests. This is the primary source of the correlated year-to-year depth variations during 2000-2003 (Figure 3.7). It was unfortunate that the reference benchmark was the one affected in this way, since all other measurements depend on how well the reference is known. The 2004 results show that the changes implemented to reduce the errors identified during the laboratory tests improved our repeatability dramatically to less that 1 cm (Table 3.2, Figure 3.5), and indicate that the MPR method has finally matured.

3.4 MPR results and modeling

The year-to-year results from the MPR measurements show apparent inflation at all four benchmarks inside the caldera relative to the benchmark outside the caldera, which is assumed to be stable. The MPR measurements, weighted by their uncertainties, are fit to a linear trend at each site in Figure 3.7. The average rate of uplift of the center of the caldera (AX63) is 19 ± 1.3 cm/yr. This formal uncertainty in the slope, based on the individual error bars and the observation time, is consistent with the standard deviation of the residuals to the fit (9.0 cm) and the four year time span of the MPR experiment (Table 3.4). The slope compares favorably with the apparent uplift rate of ~15 cm/yr as measured by the BPR instruments deployed at the caldera center during that time [*Chadwick et al.*, 2005 (in press)].

The average rates of uplift at the other three benchmarks (Figure 3.8 and Table 3.4) are either somewhat higher (AX01) or lower (AX05 and AX04). The dramatic subsidence observed in Axial caldera by the two BPRs during the 1998 eruption fit a simple deformation model (Figure 3.9a) with a Mogi point-source at 3.8 km depth beneath the center of the caldera [*Chadwick et al.*, 1999; *Fox et al.*, 2001; *Mogi*, 1958]. The subsequent rapid inflation observed by the two BPRs also suggests an inflationary source located near the caldera center [*Chadwick et al.*, 2005 (in press)] (Figure 3.9b). However, the fit of the pattern of uplift rates from the MPR measurements since 2000 to the Mogi model (with the same source depth and location) is not as good (Figure 3.9c). The fact that the average rate of inflation is greater at AX01 than at AX63 suggests the possibility that the location of maximum uplift during 2000-2004 was not at the center of the caldera, but instead was closer to AX01. The point inflation source that minimizes the misfit between the data and the model is located 1.7 km SSE of the caldera center at a depth of 5.0 km (Figure 3.10). However, source depth of 3.8 km fits the data almost equally as well (Figures 3.9d, 3.10, and 3.1). Figure 3.10 illustrates that there is a band of good fitting models running from just north of AX01 to the SSW. As the location of the source moves to the SSW, the depth and volume change must also increase in order to maintain a good fit to the data. Although the exact location, depth and volume change is not precisely known, the BPR and MPR data together suggest that post-eruption inflation began in the caldera center and subsequently migrated south. Better data coverage over the caldera would help greatly in constraining the locus of the deformation.

Note that the standard deviations of the residuals in Table 3.4 (other than for AX63) are not consistent with the formal slope uncertainty (they should be about 4 times greater for the 4 year time period). The two sites most inconsistent with a linear inflation rate (AX01 and AX05) are also the two within the area of 1998 lava (Figure 3.1). This may suggest that deformation on the 1998 lava flow has been more complex. However, if the 2000 data are not included, the standard deviation of the residuals drops to ~13 cm for AX01 and AX05. This plus the uncertainty in the reference benchmark prior to 2004 indicates that the imperfect fit to the linear trend probably reflects unaccounted for noise in the earlier measurements.

Table 3.4 MPR results (average rates of vertical displacement)

Benchmark	**2000-2004 (weighted as a function of error)**	
	Average rate (cm/yr)	**Standard deviation of residuals (cm)**
AX63	18.5 ± 1.3	9.0
AX01	22.4 ± 1.3	28.4
AX05	16.9 ± 1.3	24.0
AX04	14.9 ± 1.3	17.9

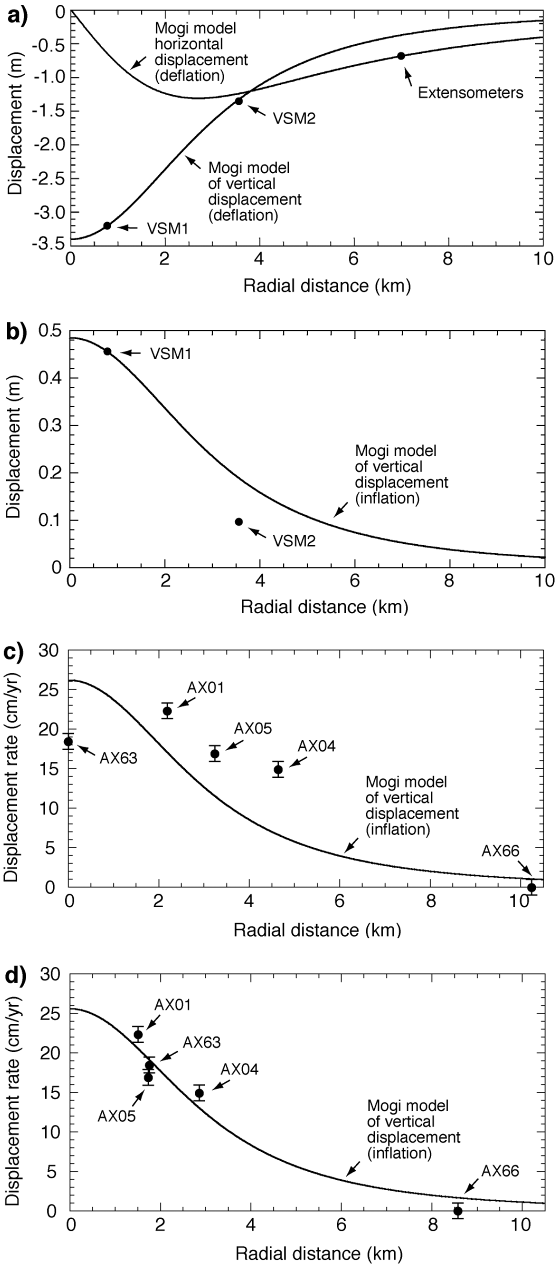

Figure 3.9 Plots of BPR data and MPR data at Axial Seamount compared to point source deformation models. (a) Deflation observed during the 1998 eruption plotted with displacements predicted by a model source located 3.8 km beneath the caldera center. (b) Uuplift observed by the VSM1 and VSM2 BPRs in the first six months after the 1998 eruption compared to a source located 3.8 km below the caldera center. (c) 2000-2004 MPR data plotted with a Mogi source located at the caldera center. The fit is not very good, indicating the source is no longer at the caldera center. (d) The data plotted with a Mogi source located 1.8 km SSE of the caldera center at a depth of 3.8 km (white star in Figure 3.1).

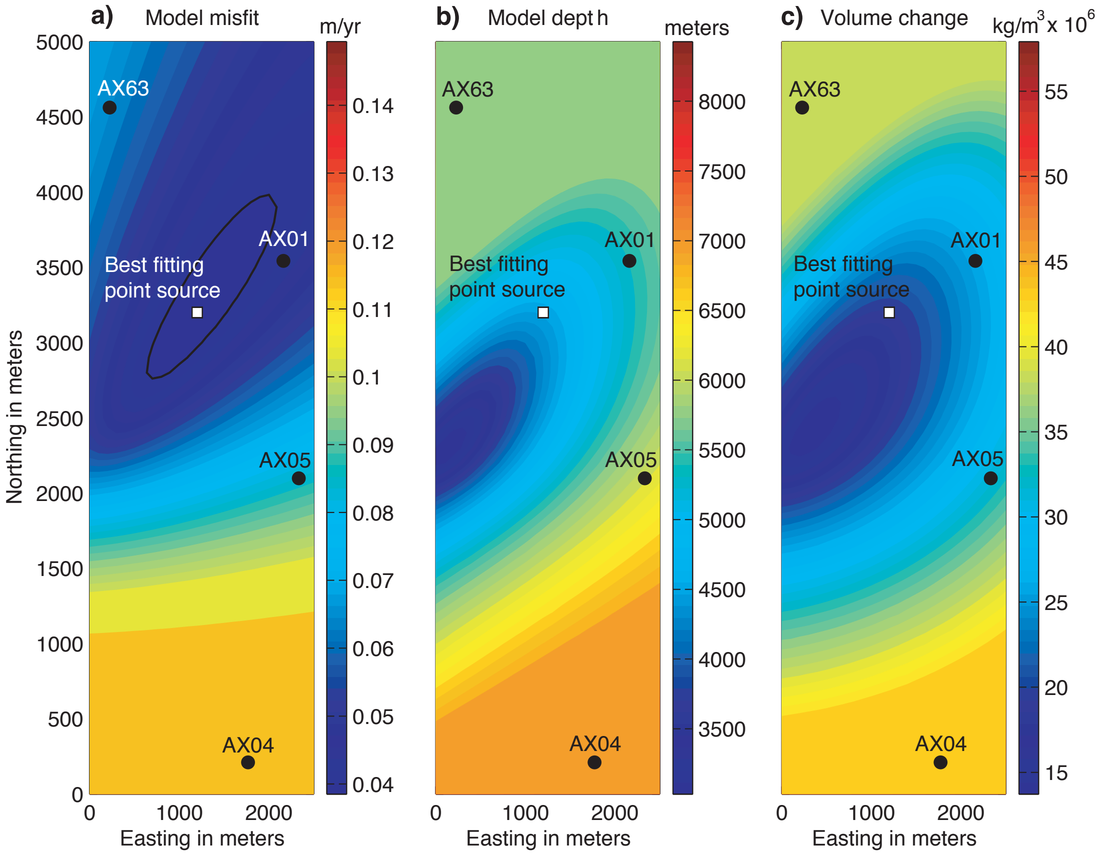

Figure 3.10 This figure maps out the range of best fitting point source inflation models to the MPR data near the caldera benchmarks. (a) The RMS misfit of the best fitting point source within the caldera. (b) The depth of the best fitting point source. (c) The volume change for the best fitting point source.

3.5 Discussion

Previous BPR results [*Chadwick et al.*, 1999; *Chadwick et al.*, 2005 (in press); *Fox et al.*, 2001] show that continuously recording pressure sensors are excellent tools for measuring large vertical, short period displacements of the seafloor. However, gradual deformation rates that are within the range of possible instrumental drift are difficult to identify unambiguously. The MPR results show that if properly done, campaign-style pressure measurements are a viable method to measure gradual volcano inflation on the seafloor. The MPR measurements can also serve as a way to constrain the drift rate of BPRs, which is likely to be very stable over time [http://www.paroscientific.com/longtermstab.htm].

The BPR and MPR data from Axial Seamount independently suggest that inflation has been occurring since its 1998 eruption at a rate that was initially high and gradually decreased to a more steady rate [*Chadwick et al.*, 2005 (in press)]. Figure 3.11 [from *Chadwick et al.*, 2005 (in press)] combines BPR and MPR results from the center of Axial caldera in one plot by making a few key assumptions: 1) the depth values of the NeMO2000 and NeMO2002 BPR data were shifted so that the rate of uplift observed in 2000-2004 (15 cm/yr) extends back to August 1998 when VSM1 was recovered, 2) the NeMO2002 data start at the same depth at which the NeMO2000 data end, and 3) the MPR data are overlain on the BPR data by aligning the 2001 MPR measurement with the underlying NeMO2000 BPR data (which is reasonable because they were co-located at the time).

The combined results in Figure 3.11 indicate that as of September 2004, the center of Axial caldera had risen 1.5 ± 0.1 m since the 1998 eruption (6.7 years). In other words, almost 50% of the 3.2 m of subsidence that occurred during the 1998 eruption has been recovered to date. If inflation continues at the current rate, the caldera will fully re-inflate to its January 1998 level by about 2014. This suggests a recurrence interval of ~16 years, which, although speculative, would not be unreasonable since it is also the time necessary to accumulate ~1 m of extensional strain (the mean thickness of dikes seen in ophiolites [*Kidd*, 1977] and tectonic windows [*Karson*, 2002] at the Juan de Fuca Ridge's spreading rate of 6 cm/yr [*Riddihough*, 1984].

The change in volume of the magma reservoir beneath Axial caldera required to cause 1.5 m of uplift depends on the location of the inflation source. Using the best fitting models, assuming the reservoir is spherical [*Delaney and McTigue*, 1994; *Johnson*, 1992], and ignoring any compression of stored magma [*Johnson et al.*, 2000], the average magma supply rate at Axial Seamount is $16\text{-}22 \times 10^6$ m^3/yr. For comparison, this rate is 2.3-5.6 times lower than the long-term average magma supply rate of $50\text{-}90 \times 10^6$ m^3/yr estimated for Kilauea Volcano, Hawaii [*Dvorak and Dzurisin*, 1993; *Dzurisin et al.*, 1984].

Long-term deformation monitoring from basaltic volcanoes on land, like Kilauea, Hawaii, or Krafla, Iceland, show that brief periods of sudden deflation associated with intrusions or eruptions are often separated by longer periods of gradual inflation during which magma is stored in centralized reservoirs [*Björnsson et al.*, 1979; *Decker*, 1987; *Tilling and Dvorak*, 1993]. During these periods of inflation, the center of uplift can migrate laterally as much as several km, apparently due to complex refilling within the magma reservoir [*Ewart et al.*, 1991; *Fiske and Kinoshita*, 1969]. Recent tomographic and multichannel seismic data show that a large magma reservoir exists beneath the summit caldera of Axial Seamount [*Kent et al.*, 2003; *West et al.*, 2001]. The deflation observed in the caldera during the 1998 eruption [*Fox*, 1999; *Fox et al.*, 2001] and the apparent re-inflation observed since then suggest the possibility of an eruption cycle at Axial with a deformation signature similar to those documented on land. Such a cycle has also been suggested by seismo-acoustic monitoring of earthquakes at Axial, which began in 1991 [*Dziak and Fox*, 1999b]. During the 7 years leading up to the 1998 eruption, the frequency and size of small earthquake swarms increased, but since the eruption, very few earthquakes have been detected. Therefore, it might be expected that as re-inflation continues and the summit magma reservoir re-pressurizes, that earthquake swarms will once again herald Axial's next eruption. The potential value of vertical deformation monitoring for estimating magma supply rates, forecasting eruptions, and quantifying displacements during eruptions is strong motivation to continue these efforts at Axial Seamount and other active submarine volcanoes.

Figure 3.12 shows two of the seismic lines from *Kent et al.* [2003] (15 such lines were collected—only two are shown for clarity). Also shown are the regional bathymetry at Axial Seamount and pressure benchmark locations (blue spheres) from *Chadwick et al.* [2005 (in press)]. The reflection from the top of magma bodies can be seen both within the caldera and to the southeast of the caldera. Little or no melt is observed along the rift zones [*Graham Kent*, personal communication]. The magma body within the caldera (~2 km depth) appears to contain a much smaller melt fraction than the shallow (~1.2 km depth) magma body southeast of the caldera, based on the observed $P_{melt}S$ phases (which are described by *Singh et al.* [1998]). Additionally, another body of melt is seen in the seismic data (not shown) further to the southeast ofthe caldera. The presence of multiple bodies of melt indicates that the geometry of

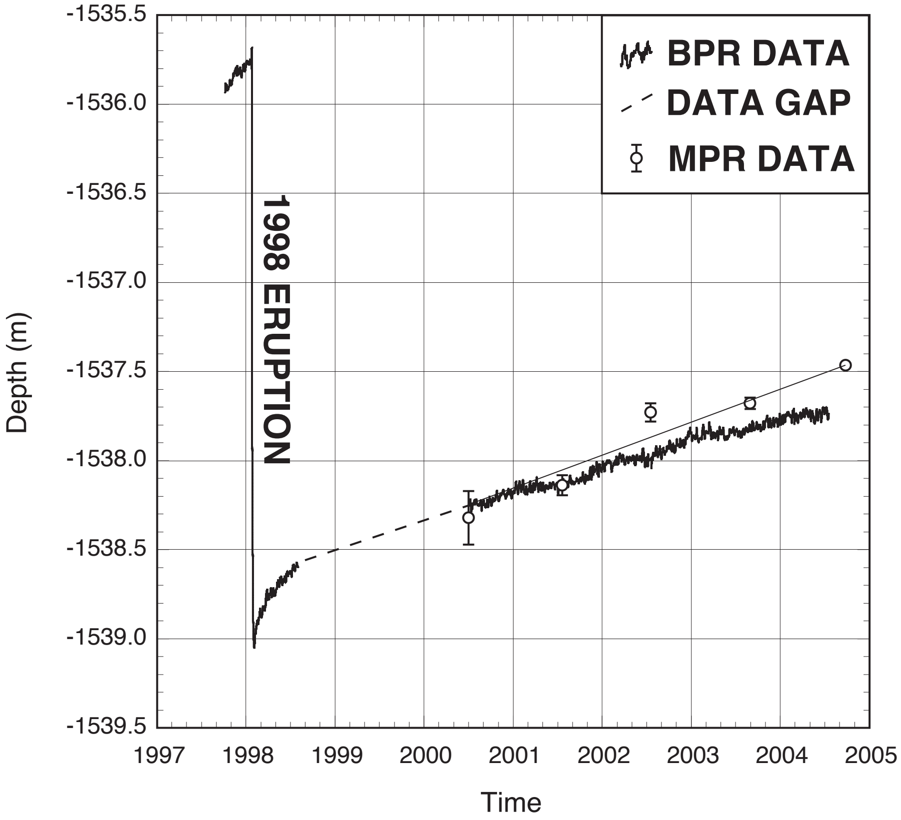

Figure 3.11 Interpretive plot of BPR and MPR data showing inflation at the center of the caldera since the 1998 eruption (BPR data include VSM1, NeMO2000, and NeMO2002; MPR data are from benchmark AX63). This plot is speculative because the individual BPRs do not share a common datum or location and the MPR measurements are relative. Nevertheless, the BPR and MPR results appear to be consistent with each other and suggest that the caldera center has been uplifting at a constant rate since the 1998 eruption. (From *Chadwick et al.*, [2005 (in press)].)

the magmatic system underlying Axial Seamount is complex. *West et al.* [2001] observed a large volume of low seismic velocities directly below the caldera from ~2 to 4 km in depth. They also found much smaller low velocity regions to the northeast and to the southwest of the caldera, but nothing anomalous to the southeast where *Kent et al.* [2003] observed the shallow melt body. *West et al.* [2001] collected their data from August 1998 to April 1999, while *Kent et al.* [2003] collected their data in

2002. While this is probably explained by differing resolutions in the two surveys, it is possible that the shallow melt body southeast of the caldera seen by *Kent et al.* [2003] was emplaced between 1999 and 2002.

Thus, the view of the volcano from our limited geodetic measurements may be inadequate. The vertical deformation data presented here can be fit by a point source of inflation located about 1.8 km southeast of the caldera center at a depth of 3.8 km below the sea floor. This model is likely too simplistic. Because of the shallow melt body to the southeast of the caldera, it is possible that some of the deformation signal that has been observed comes from this region. Interpreting deformation that in fact was produced by a sill with significant lateral extent as a point Mogi source would tend to overestimate the source depth. An additional inflationary source to the southeast could help to explain the apparent southeast shift in the location of the deformation source after the 1998 eruption. More coverage is clearly needed. The yellow spheres in Figure 4 indicate potential locations for additional gravity and pressure benchmarks. The locations were chosen based on the location of the shallow magma body southeast of the caldera.

Details about the movement of magma in this complex system are beyond our ability to resolve with the current geodetic network. However, Axial Seamount is currently the best site to study a large basaltic seafloor volcano. A significant amount of work has been done at Axial, but a significant amount remains to be done. The opportunity to study the volcano through an eruptive cycle using geodetic, seismic, geochemical, and other types of measurements would be a large step in understanding all systems of this type.

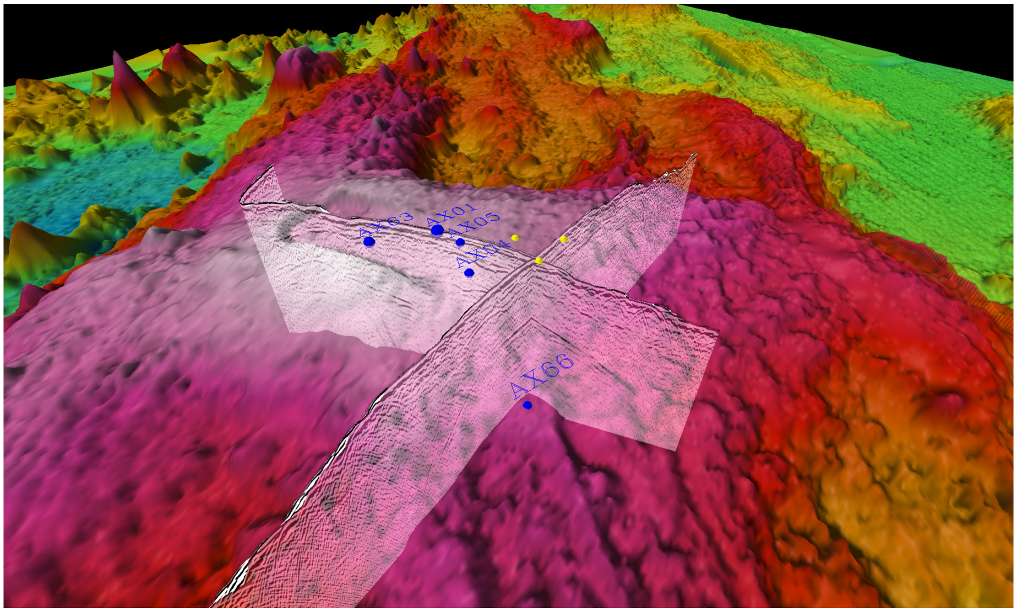

Figure 3.12 Bathymetry plot of Axial Seamount combined with two seismic sections provided by Graham Kent [*Kent et al.*, 2003]. The reflection from a shallow body of melt can be seen where the two lines cross. A deeper body of melt can be seen under the caldera. The blue spheres indicate the locations of the current seafloor benchmarks (see Fig. 1). The yellow spheres indicate possible locations of future benchmarks based on the presence of the shallow body of melt seen in the seismic profiles.

3.6 Acknowledgement

The material in Chapter 3 is an expanded version of the material as it appears in Chadwick, W. W., Nooner, S. L., Zumberge, M. A., Embley, R. W., and Fox, C. G., Vertical deformation monitoring at Axial Seamount since its 1998 eruption using deep-sea pressure sensors, *Journal of Volcanology and Geothermal Research*, (in press) 2005. I was the primary researcher on the material in this chapter, and the secondary author on the paper. Mark Zumberge and William Chadwick directed and supervised the research which forms the basis of this chapter, with contributions from the other co-authors.

3.7 References

Agnew, D.C., SPOTL: Some programs for Ocean-Tide Loading, *Scripps Institution of Oceanography Reference Series*, 96-98, 1996.

Applegate, T.B., Jr., Volcanic and structural morphology of the south flank of Axial Volcano, Juan de Fuca Ridge: results from a Sea Marc I side scan sonar survey, *Journal of Geophysical Research*, *95*, 12765-12783, 1990.

Baker, E.T., C.G. Fox, and J.P. Cowen, In situ observations of the onset of hydrothermal discharge during the 1998 submarine eruptioin of Axial Volcano, Juan de Fuca Ridge, *Geophysical Research Letters*, *26* (23), 3445-3448, 1999.

Björnsson, A., G. Johnsen, S. Sigurdsson, G. Thorbergsson, and E. Tryggvason, Rifting of the plate boundary in north Iceland, 1975-1978, *J. Geophys. Res.*, *84* (B6), 3029-3038, 1979.

Boss, E.F., and F.I. Gonzalez, Signal amplitude uncertainty of a digiquartz pressure transducer due to static calibration error, *Journal of Atmospheric and Oceanic Technology*, *11* (5), 1381-1387, 1994.

Brown, W., W. Munk, F. Snodgrass, H. Mosfjeld, and B. Zetler, MODE bottom experiment, *Journal of Physical Oceanography*, *5*, 75-85, 1975.

Chadwell, C.D., J.A. Hildebrand, F.N. Spiess, J.L. Morton, W.R. Normark, and C.A. Reiss, No spreading across the southern Juan de Fuca ridge axial cleft during 1994-1996, *Geophysical Research Letters*, *26* (16), 2525-2528, 1999.

Chadwell, C.D., F.N. Spiess, J.A. Hildebrand, L. Prawirodirdjo, L.E. Young, G.H. Purcell, and H. Dragert, The Juan de Fuca Ridge geodesy project: Strain and plate motion measurements using GPS and acoustics, *Eos Transactions American Geophysical Union*, *76* (46, Fall Meeting suppl.), F412, 1995.

Chadwick, W.W., Jr., Quantitative constraints on the growth of submarine lava pillars from a monitoring instrument that was caught in a lava flow, *Journal of Geophysical Research*, *108* (B11), 2534, 2003.

Chadwick, W.W., Jr., D.A. Butterfield, R.W. Embley, C. Meinig, S. S., S. Nooner, M. Zumberge, and C.G. Fox, Recent results from seafloor instruments at the NeMO Observatory, Axial Seamount, Juan de Fuca Ridge, *Eos Transactions American Geophysical Union*, *83* (47, Fall Meet. Suppl.), Abstract T22A-1132, 2002.

Chadwick, W.W., Jr., R.W. Embley, H.B. Milburn, C. Meinig, and M. Stapp, Evidence for deformation associated with the 1998 eruption of Axial Volcano, Juan de Fuca Ridge, from acoustic extensometer measurements, *Geophysical Research Letters*, *26* (23), 3441-3444, 1999.

Chadwick, W.W., Jr., and M. Stapp, A deep-sea observatory experiment using acoustic extensometers: Precise horizontal distance measurements across a mid-ocean ridge, *IEEE Journal of Oceanic Engineering (Special Issue on Ocean Observatories)*, *27* (2), 193-201, 2002.

Chadwick, W.W., S.L. Nooner, M.A. Zumberge, R.W. Embley, and C.G. Fox, Vertical deformation monitoring using deep-sea pressure sensors, *Journal of Volcanology and Geothermal Research*, submitted, 2005 (in press).

Cowen, J.P., R. Shackelford, D. McGee, P. Lam, E.T. Baker, and E. Olsen, Microbial biomass in the hydrothermal plumes associated with the 1998 Axial Volcano eruption, *Geophysical Research Letters*, *26* (24), 3637-3640, 1999.

Decker, R.W., Dynamics of Hawaiian volcanoes, in *Volcanism in Hawaii*, edited by R.W. Decker, T.L. Wright, and P.H. Stauffer, pp. 997-1018, 1987.

Delaney, J.R., and A.D. Chave, NEPTUNE: a fiber-optic "telescope" to inner space, *Oceanus*, *42*, 10-11, 2000.

Delaney, P.T., and D.F. McTigue, Volume of magma accumulation or withdrawal estimated from surface uplift or subsidence, with application to the 1960 collapse of Kilauea Volcano, *Bulletin of Volcanology*, *56*, 417-424, 1994.

Desonie, D.L., and R.A. Duncan, The Cobb-Eikelberg seamount chain; hotspot volcanism with mid-ocean ridge basalt affinity, *Journal of Geophysical Research*, *95*, 12697-12711, 1990.

Dvorak, J.J., and D. Dzurisin, Variations in magma supply rate at Kilauea volcano, Hawaii, *Journal of Geophysical Research*, *98* (B12), 22255-22268, 1993.

Dvorak, J.J., and D. Dzurisin, Volcano geodesy: The search for magma reservoirs and the formation of eruptive vents, *Reviews of Geophysics*, *35* (3), 343-384, 1997.

Dvorak, J.J., and A.T. Okamura, A hydraulic model to explain variations in summit tilt rate at Kilauea and Mauna Loa volcanoes, in *Volcanism in Hawaii*, edited by R.W. Decker, T.L. Wright, and P.H. Stauffer, pp. 1281-1296, 1987.

Dziak, R.P., and C.G. Fox, The January 1998 earthquake swarm at Axial Volcano, Juan de Fuca Ridge: Hydroacoustic evidence of seafloor volcanic activity, *Geophysical Research Letters*, *26* (23), 3429-3432, 1999a.

Dziak, R.P., and C.G. Fox, Long-term seismicity and ground deformation at Axial Volcano, Juan de Fuca Ridge, *Geophysical Research Letters*, *26* (24), 3641-3644, 1999b.

Dzurisin, D., A comprehensive approach to monitoring volcano deformation as a window on the eruption cycle, *Reviews of Geophysics*, *41* (1), 1001, doi:10.1029/2001RG000107, 2003.

Dzurisin, D., R.Y. Koyanagi, and T.T. English, Magma supply and storage at Kilauea Volcano, Hawaii, 1956-1983, *J. Volcanol. Geotherm. Res.*, *21*, 177-206, 1984.

Eble, M.C., and F.I. Gonzalez, Deep-ocean bottom pressure measurements in the northeast Pacific, *Journal of Atmospheric and Oceanic Technology*, *8*, 221-233, 1991.

Eble, M.C., F.I. Gonzalez, D.M. Mattens, and H.B. Milburn, Instrumentation, field operations, and data processing for PMEL deep ocean bottom pressure measurements, *NOAA Techical Memoradum*, *ERL PMEL-89*, 71pp, 1989.

Eiken, O., M.A. Zumberge, and G. Sasagawa, Gravity monitoring of offshore gas reservoirs, in *Proceedings of the Society for Exploration Geophysics*, Calgary, August 2000, 2000.

Embley, R.W., and E.T. Baker, Interdisciplinary group explores seafloor eruption with remotely operated vehicle, *Eos Transactions American Geophysical Union*, *80* (19), 213, 219, 222, 1999.

Embley, R.W., W.W. Chadwick, Jr., D. Clague, and D. Stakes, The 1998 Eruption of Axial Volcano: Multibeam anomalies and seafloor observations, *Geophysical Research Letters*, *26* (23), 3425-2428, 1999.

Embley, R.W., K.M. Murphy, and C.G. Fox, High-resolution studies of the summit of Axial Volcano, *Journal of Geophysical Research*, *95*, 12785-12812, 1990.

Ewart, J.A., B. Voight, and A. Björnsson, Elastic deformation models of Krafla Volcano, Iceland, for the decade 1975 through 1985, *Bulletin of Volcanology*, *53*, 436-459, 1991.

Feely, R.A., E.T. Baker, G.T. Lebon, J.F. Gendron, J.A. Resing, and J.P. Cowen, Evience for iron and sulfur enrichments in hydrothermal plumes at Axial Volcano following the January-February 1998 eruption, *Geophysical Research Letters*, *26* (24), 3649-3652, 1999.

Fiske, R.S., and W.T. Kinoshita, Inflation of Kilauea volcano prior to its 1967-1968 eruption, *Science*, *165*, 341-349, 1969.

Fofonoff, N.P., Physical properties of seawater: A new salinity scale and equation of state for seawater, *Journal of Geophysical Research*, *90* (C2), 3332-3342, 1985.

Fofonoff, N.P., and R.C. Millard, Jr., Algorithms for computation of fundamental properties of seawater, in *UNESCO technical papers in marine science*, pp. 53, 1983.

Fox, C.G., Evidence of active ground deformation on the mid-ocean ridge: Axial Seamount, Juan de Fuca Ridge, April-June, 1988, *J. Geophys. Res.*, *95*, 12813-12822, 1990.

Fox, C.G., Five years of ground deformation monitoring on Axial Seamount using a bottom pressure recorder, *Geophysical Research Letters*, *20* (17), 1859-1862, 1993.

Fox, C.G., Special collection on the June 1993 eruption on the CoAxial segment, Juan de Fuca Ridge, *Geophysical Research Letters*, *22*, 129-130, 1995.

Fox, C.G., In situ ground deformation measurements from the summit of Axial Volcano during the 1998 volcanic episode, *Geophysical Research Letters*, *26* (23), 3437-3440, 1999.

Fox, C.G., W.W. Chadwick, Jr., and R.W. Embley, Detection of changes in ridge-crest morphology using repeated multibeam sonar surveys, *Journal of Geophysical Research*, *97*, 11149-11162, 1992.

Fox, C.G., W.W. Chadwick, Jr., and R.W. Embley, Direct observation of a submarine volcanic eruption from a sea-floor instrument caught in a lava flow, *Nature*, *412*, 727-729, 2001.

Fujimoto, H., K. Koizumi, Y. Osada, and T. Kanazawa, Development of instruments for seafloor geodesy, *Earth, Planets, and Space*, *50*, 905-911, 1998.

Fujimoto, H., M. Mochizuki, K. Mitsuzawa, T. Tamaki, and T. Sato, Ocean bottom pressure variations in the southeastern Pacific following the 1997-98 El Nino event, *Geophysical Research Letters*, *30* (9), 1456, 2003.

Fujita, M., M. Sato, T. Yabuki, M. Mochizuki, and A. Asada, Examination on repeatability of GPS/Acoustic seafloor positioning for the reference points deployed around Japan, *Eos Transactions American Geophysical Union*, *84* (46, Fall Meet. Suppl.), Abstract G21D-0297, 2003.

Gill, A.E., *Atmosphere-Ocean Dynamics*, 662 pp., Academic Press, New York, 1982.

Hammond, S.R., and J.R. Delaney, Evolution of Axial Volcano, Juan de Fuca Ridge, *Eos Transactions American Geophysical Union*, *66*, 925, 1985.

Hildebrand, J.A., C.D. Chadwell, S.M. Wiggins, and F.N. Spiess, Offshore geodetic monitoring on the southeast flank of Kilauea Volcano (abstract), *Seismological Research Letters*, *71* (2), 232, 2000.

Hildebrand, J.A., J.M. Stevenson, P.T.C. Hammer, M.A. Zumberge, R.L. Parker, and C.G. Fox, A seafloor and sea surface gravity survey of Axial Volcano, *Journal of Geophysical Research*, *95*, 12751-12763, 1990.

Johnson, D.J., Dynamics of magma storage in the summit reservoir of Kilauea volcano, Hawaii, *Journal of Geophysical Research*, *97*, 1807-1820, 1992.

Johnson, D.J., F. Sigmundsson, and P.T. Delaney, Comment on "Volume of magma accumulation or withdrawal estimated from surface uplift or subsidence, with application to the 1960 collapse of Kilauea Volcano" by P. T. Delaney and D. F. McTigue, *Bulletin of Volcanology*, *61*, 491-493, 2000.

Karson, J.A., Geologic structure of the uppermost oceanic crust created at fast- to intermediate-rate spreading centers, *Annual Reviews of Earth and Planetary Science*, *30*, 347-384, 2002.

Karsten, J.L., and J.R. Delaney, Hot spot-ridge crest convergence in the Northeast Pacific, *Journal of Geophysical Research*, *94*, 700-712, 1989.

Kent, G., A. Harding, J. Babcock, J.A. Orcutt, R.S. Detrick, J.P. Canales, E.M. Van Ark, S.M. Carbotte, J. Diebold, and M. Nedimovic, A new view of 3-D magma chamber structure beneath Axial Seamount and Coaxial segment: Preliminary results from the 2002 multichannel seismic survey of the Juan de Fuca Ridge, *Eos Transactions American Geophysical Union*, *84* (46, Fall Meet. Suppl.), Abstract B12A-0755, 2003.

Kidd, R.G.W., A model for the process of formation of the upper oceanic crust, *Geophysical Journal of the Royal Astronomical Society*, *50*, 149-183, 1977.

Leroy, C.C., and F. Parthiot, Depth-pressure relationships in the oceans and seas, *Journal of the Acoustical Society of America*, *103* (3), 1346-1352, 1998.

Lu, Z., T. Masterlark, D. Dzurisin, R. Rykhus, and C. Wicks, Jr., Magma supply dynamics at Westdahl volcano, Alaska, modeled from satellite radar interferometry, *Journal of Geophysical Research*, *108* (B7), 2354, doi:10.1029/2002JB002311, 2003.

Lupton, J., E. Baker, R. Embley, R. Greene, and L. Evans, Anomalous helium and heat signatures associated with the 1998 Axial Volcano event, juan de Fuca Ridge, 1999.

Mogi, K., Relations between the eruptions of various volcanoes and the deformation of the ground surfaces around them, *Bulletin of the Earthquake Research Institute, University of Tokyo*, *36*, 99-134, 1958.

Morgan, W.J., Plate motion and deep mantle convection, *Geological Society of America Memoir*, *132*, 7-22, 1972.

Nagaya, Y., T. Urabe, and T. Yabuki, Crustal deformation observation at the crest of the EPR 18.5S with the seafloor acoustic ranging method, *Eos Transactions American Geophysical Union*, *80* (46, Fall Meeting suppl.), F1076, 1999.

Osada, Y., H. Fujimoto, S. Miura, A. Sweeney, T. Kanazawa, S. Nakao, S. Sakai, J.A. Hildebrand, and C.D. Chadwell, Estimation and correction for the effect of sound velocity variation on GPS/Acoustic seafloor positioning: An experiment off Hawaii Island, *Earth, Planets, and Space*, *55*, e17-e20, 2003.

Resing, J.A., R.A. Feely, G.J. Massoth, and E.T. Baker, The water-column chemical signature after the 1998 eruption of Axial Volcano, *Geophysical REsearch Letters*, *26* (24), 3645-3648, 1999.

Riddihough, R., Recent movements of the Juan de Fuca plate system, *Journal of Geophysical Research*, *89* (B8), 6980-6994, 1984.

Sasagawa, G., W. Crawford, O. Eiken, S. Nooner, T. Stenvold, and M. Zumberge, A new sea-floor gravimeter, *Geophysics*, *68*, 544-553, 2003.

Segall, P., and J.L. Davis, GPS applications for geodynamics and earthquake studies, *Annual Reviews of Earth and Planetary Science*, *25*, 301-336, 1997.

Singh, S.C., G. Kent, G., J.S. Collier, A.J. Harding, and J. Orcutt, A., Melt to mush variations in crustal magma properties along the ridge crest at the southern East Pacific Rise, *Nature*, *394*, 874-878, 1998.

Spiess, F.N., C.D. Chadwell, J.A. Hildebrand, L.E. Young, G.H. Purcell, Jr., and H. Dragert, Precise GPS/Acoustic positioning of seafloor reference points for tectonic studies, *Physics of the Earth and Planetary Interiors*, *108* (2), 102-112, 1998.

Stalin, S.E., H.B. Milburn, and C. Meinig, NeMO Net: A near real-time deep ocean observatory, in *Proceedings of the MTS/IEEE Conference and Exhibition, 11-14 September 2000*, pp. 583-587, Providence, RI, 2001.

Sturkell, E., P. Einarsson, F. Sigmundsson, S. Hreinsdottir, and H. Geirsson, Deformation of Grimsvotn volcano, Iceland: 1998 eruption and subsequent inflation, *Geophysical Research Letters*, *30* (4), 1182, 2003.

Tilling, R.I., and J.J. Dvorak, Anatomy of a basaltic volcano, *Nature*, *363*, 125-133, 1993.

Watanabe, T., H. Matsumoto, H. Sugioka, H. Mikada, and K. Suyehiro, Offshore monitoring system records recent earthquake off Japan's Northernmost island, *Eos Transactions American Geophysical Union*, *85* (2), 14, 2004.

Watts, D.R., and H. Kontoyiannis, Deep-ocean bottom pressure measurements, *J. Atmos. Ocean. Tech.*, *7*, 296-306, 1990.

Wearn, R.B., Jr., Year long stability measurements on Paroscientific atmospheric pressure transducers, in *Technical Note*, pp. 15, Paroscientific, Inc., 1985.

Wearn, R.B., and N.G. Larson, Measurements of the sensitivities and drift of Digiquartz pressure sensors, *Deep-Sea Research*, *29* (1A), 111-134, 1982.

West, M.E., W. Menke, M. Tolstoy, S. Webb, and R. Sohn, Magma storage beneath Axial Volcano on the Juan de Fuca mid-ocean ridge, *Nature*, *413*, 833-836, 2001.

Wunsch, C., and D. Stammer, Atmospheric loading and the oceanic "inverted barometer" effect, *Reviews of Geophysics*, *35* (1), 79-107, 1997.

Zebker, H.A., F. Amelung, and S. Jonsson, Remote sensing of volcano surface and internal processes using radar interferometry, in *Remote Sensing of Active Volcanism*, edited by P.J. Mouginis-Mark, J.A. Crisp, and J.H. Fink, pp. 179-206, American Geophysical Union, Washington, D.C., 2000.

Chapter 4

Structure of oceanic core complexes: Constraints from seafloor gravity measurements made at the Atlantis Massif

4.1 Introduction

4.1.1 Background

This study was focused on Atlantis Massif, which is located at the eastern inside corner of the intersection between the Atlantis Transform Fault and the Mid-Atlantic Ridge (MAR) at 30° N, 42° W. Spreading parallel corrugations on the domal surface (Figure 4.1) are reminiscent of surface morphology at some continental core complexes in the Basin and Range and have been interpreted as characteristics of a detachment fault surface [*Davis and Lister*, 1988, *Cann et al.*, 1997]. Similar features have been seen at two fossil massifs along the Atlantis Fracture Zone [*Blackman et al.*, 1998; *Cann et al.*, 1997], at other places along the MAR [e.g. *Cannat et al.*, 1995; *MacLeod et al.*, 2002; *Tucholke et al.*, 2001] and elsewhere [e.g. *Ranero and Reston*, 1999]. The current accepted models are that these topographic highs are oceanic core complexes that form when the extension of the crust is taken up by faulting along a detachment fault rather than by plate accretion [*Dick et al.*, 1991, *Mutter and Karson*,

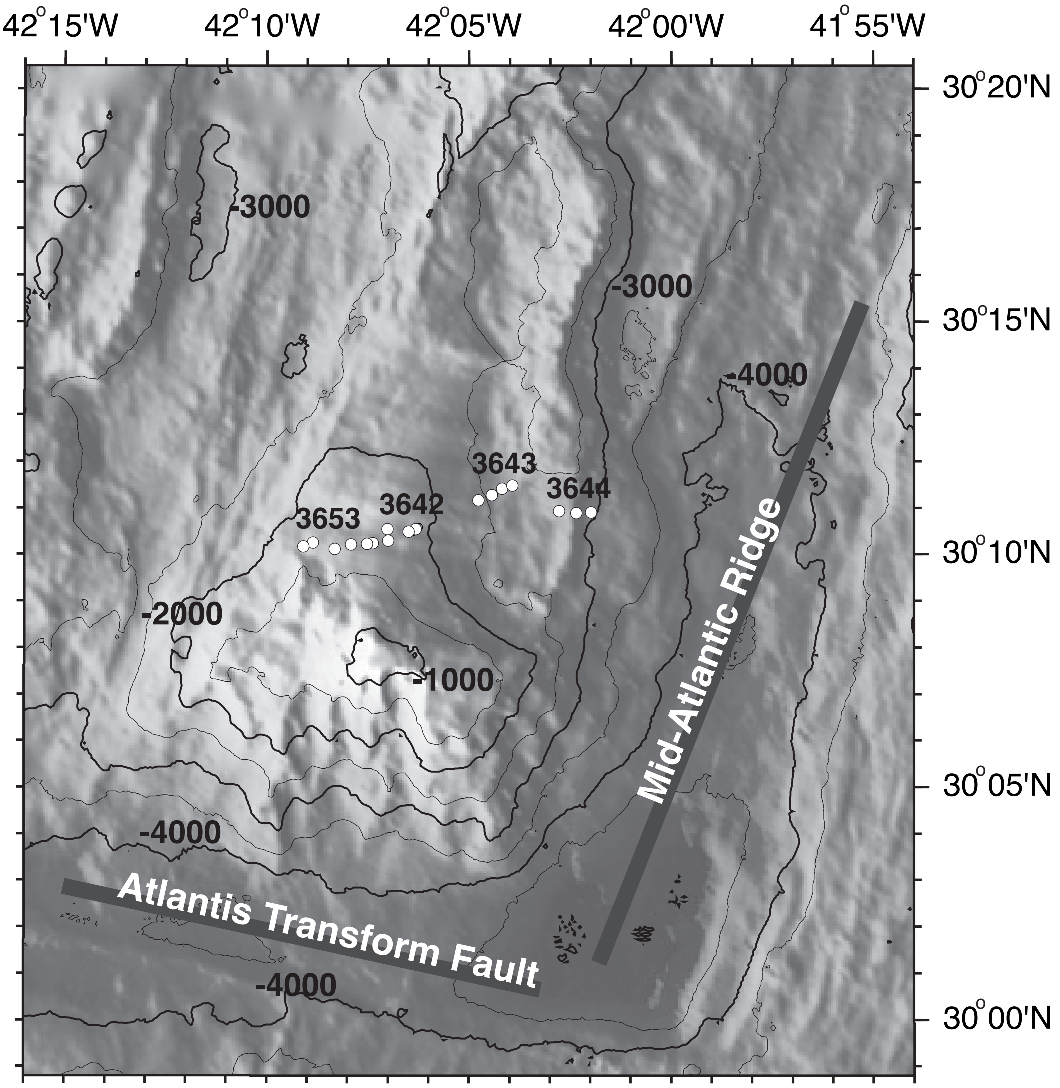

Figure 4.1 Bathymetry map with the location of seafloor gravity sites shown as white circles. Alvin dives are numbered. Notice the corrugations running from east to west near dive 3642.

1992, *Tucholke and Lin*, 1994]. As the crust extends via this low angle fault, lower crustal and upper mantle rocks are rafted to the surface. Therefore, fault rocks and ultramafic rocks that have been sampled on or near the Atlantis Massif and other hypothesized core complexes [*Dick et al.*, 1991; *Cannat et al.*, 1995; *Karson*, 1999;

MacLeod et al., 2002; *Tucholke and Lin*, 1994; *Cann et al.*, 1997; *Tucholke et al.*, 2001; *Blackman et al.*, 2001] are congruent with this idea.

Seismic evidence of a detachment fault on the African plate capable of exhuming lower crustal or upper mantle material has been shown by *Ranero and Reston* [1999]. Uplift of high-density rock in this way might explain the presence of the observed gravity high on the Atlantis Massif. However, *Campbell and John* [1996] gave evidence for emplacement of a synextensional dike-like pluton beneath a detachment fault within the Colorado extensional corridor to explain the gravity high observed there. We use new seafloor gravity data in combination with existing sea surface gravity data to constrain a suite of 3-D forward models in order to place bounds on the geometry and value of the anomalous density in the exposed oceanic core complex at Atlantis Massif.

4.1.2 Seafloor and sea surface gravity acquisition

We collected the seafloor gravity data with our seafloor gravimeter, ROVDOG (Remotely Operated Vehicle deployable Deep Ocean Gravimeter), during the Nov.-Dec., 2000 cruise of the *R/V Atlantis* as one component of MARVEL 2000. The ROVDOG was carried outside DSV *Alvin* and placed on the sea floor while an operator inside the *Alvin* controlled the instrument and observed the data collection in real time. After an observation time of 10-20 minutes the instrument was retrieved and transported to the next site. A seafloor survey taken with a single meter at an average depth of 300 m has demonstrated a precision of 28 μGal or better. Further technical details may be found in *Sasagawa et al.* [2003].

The locations of the gravity dive sites (shown in Figure 4.1) form an approximately spreading-parallel line. During each of the dives, the *Alvin* gathered rock samples and stopped for gravity measurements. On average, the 18 gravity sites were spaced 557 meters apart during each of the four dives[1]. The sea surface gravity data that we used as part of the modeling are described in *Blackman et al.*, [1998]. The uncertainty in these data are ~1.8 mGal as indicated by the standard deviation in track crossing misfits. The location of the line is shown in Figure 4.1.

4.2 Data Reduction for Seafloor Gravity

We corrected the gravity data for instrument drift, tides, latitude, and lithospheric cooling. We also made free water corrections to the data. The resulting uncertainties are summarized in Table 4.1. Further details can be found in Appendix 2 of the supporting material[1]. The accuracy in calculating the complete Bouguer anomaly from seafloor gravity data is greatly dependent on how well the shape of the seafloor itself is known. In a region like the MAR 30° N area, the terrain is often rugged and steep, making a precise terrain correction difficult. The regional bathymetry was gridded with a 100 m spacing [*Blackman et al.*, 1998], which effectively smoothes the terrain, causing discrepancies between the actual depth and that predicted by the grid. To minimize this problem, depth was measured at the gravity sites with a Paroscientific 410k pressure gauge which has demonstrated a repeatability of 3 cm in relative depth [*Sasagawa et al.*, 2003]. The free water corrections and the slab component of the terrain correction were made using these

---

[1] Supporting material is available in Appendix 4.

measured instrument depths. The resulting uncertainty in the slab correction is 0.004 mGal, using 2900 kg/m^3 as the reference density. We estimate the uncertainty in the free-water anomaly to be 0.083 mGal, whereas previous seafloor gravity studies reported uncertainties of 0.30 mGal or greater [*Luyendyk*, 1984; *Hildebrand et al.*, 1990; *Holmes et al.*, 1993; *Ballu et al.*, 1998; *Cochran et al.*, 1999].

The RMS difference between the measured depths and those obtained from the bathymetry grid was 37 meters (150 m maximum). Shifting the survey points 100 meters west relative to the bathymetry reduced the maximum difference to about 30 m, with an RMS difference of 20 m. To determine the error in the terrain correction due to this unmatched depth, a Monte Carlo approach was used: normally distributed zero mean random noise (with standard deviation $\sigma = 20$ m) was added to the bathymetric data and the terrain correction was computed. One thousand iterations of this yielded an average standard deviation of 0.262 mGal, which was adopted as the terrain correction uncertainty. This provides a better statistical estimate of uncertainty than simply computing the gravity effect of a 20 m slab, which would give an uncertainty value of about 2.4 mGal.

The complete Bouguer anomaly is shown in Figure 4.2. The RMS uncertainty in the measurements and corrections is summarized in Table 1. The total uncertainty (0.275 mGal) is dominated by the imperfect terrain correction (0.262 mGal), demonstrating the need for more detailed bathymetry in high precision seafloor gravimetry. However, the results of this study were not strongly influenced by this issue.

4.3 Gravity Modeling

Although difficult to model, small-scale features undoubtedly affect our ability to interpret the data. For instance, there is probably a continuum of density values as well as a complicated density interface boundary, such as a steepening or shallowing dip angle with depth. Due to these factors and to the inherent non-uniqueness of gravity, we approached the problem by looking only at simple, end member model geometries that neglect these second order effects. Thus we tested four types of models: homogeneous density, one-fault, cylindrical plug, and wedge.

Blackman et al. [1998] observed that the gravity high is slightly east of the topographic high at the Atlantis Massif. Our seafloor gravity measurements confirm this. Therefore a homogeneous density model does not adequately fit both data sets, since the gravity follows topography in such a case. However, the best fitting density to this model was useful in justifying our choice for the reference density used in the Bouguer and terrain corrections (2900 kg/m^3). A one-fault model with one east dipping density boundary has the same difficulty as the one density model, indicating that a west-dipping boundary may be present. We also modeled a vertically oriented cylindrical plug of higher density centered on the gravity high, as has been documented in the Basin and Range [*Campbell and John*, 1996]. However, for the Atlantis Massif, this geometry requires an extremely large density contrast (greater than 1200 kg/m^3) and a radial extent of 10-20 km for even a nominal fit to the seafloor data. The best fitting simple model that we examined consisted of only two bodies: a high-density wedge and the surrounding terrain (see Appendix 4). The boundaries of the high-density wedge are sides sloping off to the east and to the west (Figure 4.3) and the transform fault to the south. The northern boundary is at 30°20' N. Tests showed that the geometry of the north and south boundaries had no significance on the model results. We swept through all combinations of east and west dip angles and wedge density contrast, requiring that the model fit both sea-surface and seafloor data.

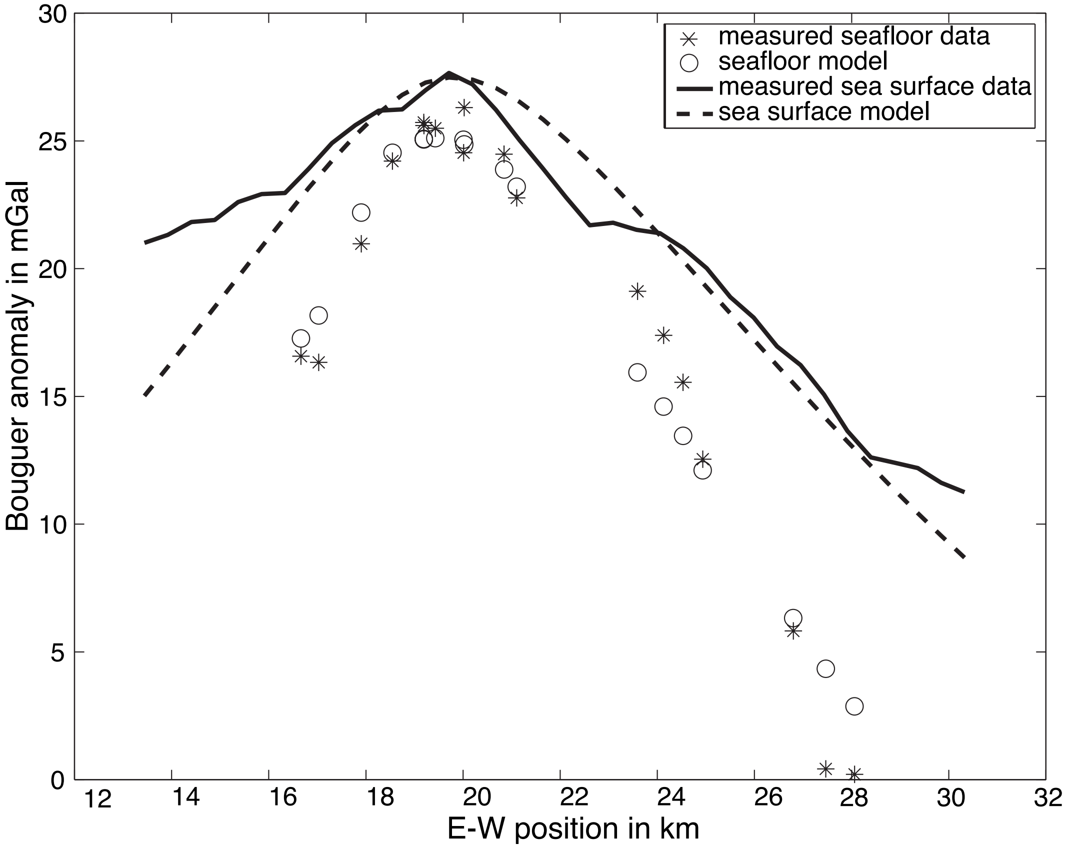

Figure 4.2 This figure shows one model fit to the seafloor and sea surface data. The dip angles bounding the high-density wedge are 16° in the east and 20° in the west; Δρ is 250 kg/m^3.

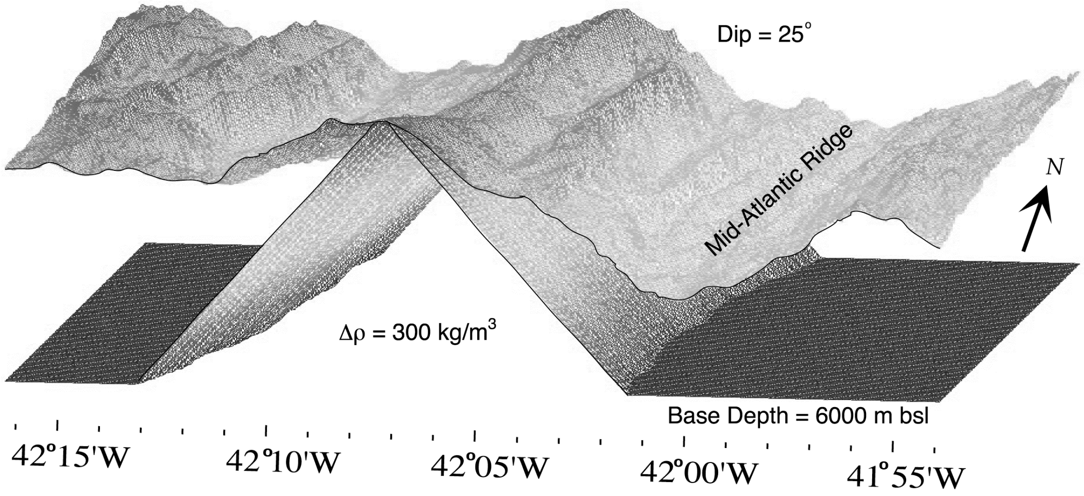

Figure 4.3 The boundaries of the high-density area form a wedge with sides sloping off to the east and to the west. We computed a suite of 3-D forward models, varying the dip angle and the density contrast of the wedge, requiring that the model fit both sea-surface and seafloor data. This wedge terminates at a depth of 6000 m below sea level (base depth). The horizontal extent of this region is 47.5 km and the vertical extent is ~5 km.

Figure 4.4 shows the standard deviation, σ, of both the seafloor and the sea surface residuals to the wedge model as a function of the east boundary dip angle and density contrast with respect to a 2900 kg/m^3 reference (the dip angle in the west is held fixed at 20° for the figure). The geometries that fit both data sets best have boundary dip angles between 16°-24° in the east and 16°-28° in the west and density contrasts of 250-350 kg/m^3. These ranges were obtained by requiring $\sigma < 2$ mGal for both seafloor and sea surface. For the sea surface, this range was chosen because it is about the same as the uncertainty in the data. It was chosen for the seafloor because 2 mGal is approximately the small-scale variation of the data. This was determined from the residuals to a best-fitting second order polynomial. The range of eastern dip angles is slightly steeper than the angle at which the corrugated seafloor dips (~11°), indicating that the density boundary does not coincide with the fault surface. It is worth noting that the seafloor data appear to constrain the model more tightly than the sea surface data, despite the limited coverage. The seafloor data favor higher density for the wedge and a low angle boundary dip, while the sea surface data favor geometries with lower density contrast and do not constrain the fault angles well. However, a combination of the two data sets provides much better constraints than either alone.

4.4 Discussion

At the Atlantis Massif, most of the detachment fault surface is draped with pelagic ooze of some thickness, making outcrops of basement rock difficult to find. However, serpentinized peridotites and evidence of shearing are widespread across the exposed southern wall of the massif [*Blackman et al.*, 2001]. Seismic data also suggest that partially serpentinized to unaltered peridotite exist less than 1 km below the seafloor in this area [*Collins et al.*, 2001]. Consistent with this, our gravity results indicate that the core of the massif is composed of rocks with an average density of 3150-3250 kg/m^3. The best fitting geometries indicate that both the east and west boundaries are more steeply dipping than the corrugated surface of the massif, as hinted at by the eastward shift of the gravity high with respect to the topographic high. This means that in the east the inferred detachment fault surface does not coincide with the density boundary, creating a strip of less dense material up to 1 km thick within the foot wall block. This is also seen in the results of the NOBEL seismic

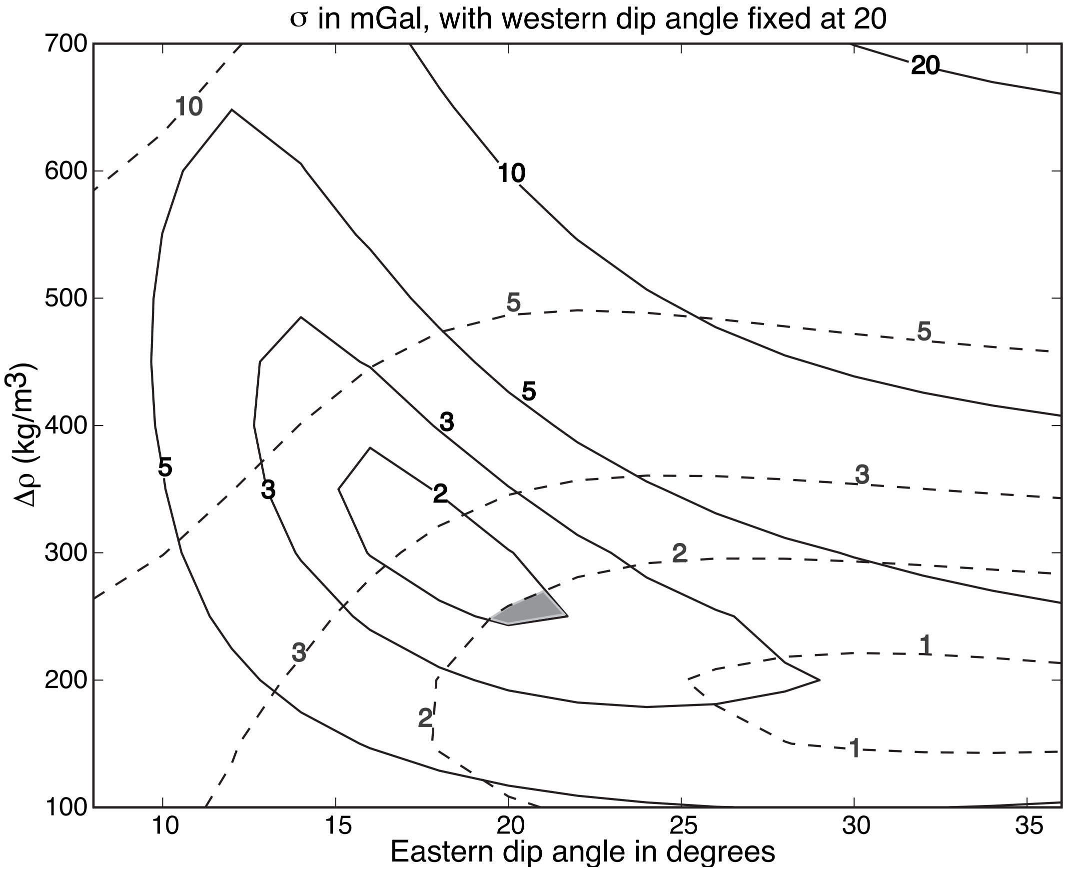

Figure 4.4 Standard deviation,σ, of the residuals to the model fit as a function of the eastern boundary dip angle and density contrast with respect to the 2900 kg/m^3 reference. For this figure, the dip is constant at 20° in the west. Seafloor results are shown by solid lines and sea surface results are shown by dashed lines. The models that fit both data sets best, shaded region, have central high density wedge boundaries with dip angles between 16°-24° in the east and 16°-28° in the west and density contrasts of 250-350 kg/m^3.

experiment [*Collins et al.*, 2001]. This low-density layer is most likely an alteration front that is sub-parallel to the detachment fault surface. Supporting this idea, rock samples from the detachment surface indicate that it is composed primarily of serpentinized peridotite with some lesser amount of gabbroic material [*Cann et al.*, 1997]. A less likely scenario is that this zone is instead magmatic in nature; i.e. rotated volcanic intrusives created during a brief magmatic phase early in the evolution of the massif, and later cut by the detachment fault, uplifted, and exposed at the surface. However, our modeling shows that large-scale dike-like intrusions beneath the detachment surface are not the cause of the observed gravity anomaly. Instead, the observed wedge-like geometry of the core is consistent with the unroofing of deep seated rock by extension and rotation along a detachment fault.

The western density boundary also dips below the seafloor. Several ideas can be put forth to explain this. First, this could be a compositional boundary due to layering of a rotated crustal block. Second, the low-density region might be due to the presence of a rider block that was carried eastward during extention along the detachment. Finally, the zone could be a continuation of the alteration front associated with the detachment fault surface. The breakaway zone is thought to be several kilometers west of the modeled area. Our limited gravity coverage in the west does not allow us to make any conclusive statements regarding structure of this area.

These interpretations are consistent with the presence of a detachment fault. Although some seismic studies have been done in the region [*Collins and Detrick*, 1998; *Collins et al.*, 2001], more detailed results could help further constrain dip angles and elastic properties of the massif, allowing us to better define the density contrast and geometry. Because of the limited coverage of our single-profile seafloor data set it is not beneficial to test more complicated models, although it is likely that there is some small scale surface density variability as well as subsurface density structure. In fact, because of the limited extent, the gravity data provide little north-south constraints on the structure. These come mostly from the morphology of the region. Further studies of these structures with more extensive gravity measurements, seismic studies, and drilling will help us to understand these interesting extensional regions.

Acknowledgements. We thank the shipboard participants on cruise AT03-60, the officers, crew and pilots of the RV *Atlantis* and *DSV Alvin,* Statoil for the loan of ROVDOG, Robert L. Parker for software, and Eric Husmann for instrument preparation, and the reviewers for their suggestions.

4.5 Acknowledgement

The material in Chapter 4 is a reprint of the material as it appears in Nooner, S.L, G.S. Sasagawa, D.K. Blackman, and M.A. Zumberge, Structure of oceanic core complexes: Constraints from seafloor gravity measurements made at the Atlantis Massif, *Geophysical Research Letters*, 30(8), 1446-1449, 2003. I was the primary researcher and author on the paper. Mark Zumberge directed and supervised the research which forms the basis of this chapter, with contributions from the other co-authors.

4.6 References

Ballu, V., J. Dubois, C. Deplus, M. Diament, S. Bonvalot, Crustal structure of the Mid-Atlantic Ridge south of the Kane Fracture Zone from seafloor and sea surface gravity data, *J. Geophys. Res.*, 103, 2615-31, 1998.

Blackman, D.K., J.R. Cann, B. Janssen, and D.K. Smith, Origin of extensional core complexes: Evidence from the Mid-Atlantic Ridge at Atlantis Fracture Zone, *J Geophys. Res.*, 103, 21,315-21,333, 1998.

Blackman, D.K., D.S. Kelley, J.A. Karson and MARVEL2000, New seafloor maps and samples from the Mid-Atlantic Ridge 30N oceanic core complex, *Eos Trans. AGU*, 82(47), Fall Meet. Suppl., 2001.

Campbell, E.A, B.E. John, Constraints on extension-related plutonism from modeling of the Colorado River gravity high, *Geolog. Soc. Am. Bulletin*, 108, 1242-1255, 1996.

Cann, J.R., D.K. Blackman, D.K. Smith, E. McAllister, B. Janssen, S. Mello, E. Avgerinos, A.R. Pascoe, J. Escartin, Corrugated slip surfaces formed at ridge-transform intersections on the Mid-Atlantic Ridge, *Nature*, 385, 329-332, 1997.

Cannat, M., C. Mevel, M. Maia, C. Deplus, C. Durand, P. Gente, P. Agrinier, A. Belarouchi, G. Dubuisson, E. Humler, J. Reynolds, Thin crust, ultramafic exposures, and rugged faulting patterns at the Mid-Atlantic Ridge (22°-24°N), *Geology*, 23, 49-52, 1995.

Cochran, J.R., D.J. Fornari, B.J. Coakley, R. Herr, M.A. Tivey, Continuous near-bottom gravity measurements made with a BGM-3 gravimeter in DSV Alvin on the East Pacific Rise Crest near 9°31'N and 9°50' N, *J. Geohys, Res.*, 104, 10841-10861, 1999.

Collins, J. and R.S. Detrick, Seismic structure of the Atlantis Fracture Zone megamullion, a serpentinized untramafic massif, *Eos Trans. AGU*, 79, F800, 1998.

Collins, J.A., Tucholke, B.E., and J. Canales, Structure of Mid-Atlantic Ridge megamullions from seismic refraction experiments and multichannel seismic reflection profiling, *Eos Trans. AGU*, 82, Fall Meet. Suppl., F1100, 2001.

Davis, G.A., and G.S. Lister, Detachment faulting in continental extention; perspectives from the southwestern U.S. cordillera, *Spec. Pap. Geol. Soc. Am.*, 218, 133-159, 1988.

Dick, H.J.B., P.S. Meyer, S. Bloomer, S. Kirby, D. Stakes, C. Mawer, Lithostratigraphic evolution of an in-situ section of oceanic layer 3, in Von Herzen and Robinson et al, *Proc. ODP Sci. Res.*, 118, 439-538, 1991.

Hildebrand, J.A., Stevenson, J.M., Hammer, P.T.C., Zumberge, M.A. and R.L. Parker, A seafloor and sea surface gravity survey of Axial Volcano, *J. Geophys.*, Res. 95, 12,751-12,763, 1990.

Holmes, M.L., H.P. Johnson, Upper crustal densities derived from seafloor gravity measurements: northern Juan de Fuca Ridge, *Geophys. Res. Lett.*, 20, 1871-1874, 1993.

Karson, J.A., Geological investigation of a lineated massif at the Kane Transform Fault: implications for oceanic core complexes, *Phil. Trans. Roy. Soc. Lond.*, A 357, 713-736, 1999.

Luyendyk, B.P., On-bottom gravity profile across the East Pacific rise crest at 21° north, *Geophysics*, 49, 2166-2177, 1984.

MacLeod, C.J., J. Escartin, D. Banerji, G.J. Banks, M. Gleeson, D.H.B. Irving, R.M. Lilly, A.M. McCaig, Y. Niu, S. Allerton, D.K. Smith, Direct geological evidence for oceanic detachment faulting: The Mid-Atlantic Ridge, 15°45'N, *Geology*, 30, 879-882, 2002.

Mutter, J.C. and J.A. Karson, Structural processes at slow spreading ridges, *Science*, 257, 627-634, 1992.

Ranero, C.R. and T.J. Reston, Detachment faulting at ocean core complexes, *Geology*, 27, 983-986, 1999.

Sasagawa, G., W. Crawford, O. Eiken, S. Nooner, T. Stenvold, M. Zumberge, A new seafloor gravimeter, *Geophysics*, in press 2003.

Tucholke, B.E. and Lin, J., A geological model for the structure of ridge segments in slow spreading ocean crust, *J. Geophys. Res.*, 99, 11,937-11,958, 1994.

Tucholke, B.E., K. Fujioka, T. Ishihara, G. Hirth and M Kinoshita, Submersible study of an oceanic megamullion in the central North Atlantic, *J. Geophys. Res.*, 106, 16,145-16,161, 2001.

Chapter 5

Conclusion

5.1 Summary of work

Studies on the seafloor are difficult, time-consuming, and expensive. Therefore, the development of seafloor geophysical instruments always lags the development of similar instruments on land. However, since about 71% of the Earth is covered by the oceans, it is crucial to study the structure of the seafloor. The studies described in this work utilize relatively new instruments and techniques in marine geophysics to examine three different problems on the seafloor. The first two describe seafloor deformation and the movement of mass within the crust (carbon dioxide in the first case and magma in the second case) using seafloor gravity and pressure measurements. The third puts constraints on the density structure of an oceanic core complex.

The first study is an examination of human induced changes in a sub-seafloor aquifer due to the injection of carbon dioxide. At the Sleipner project in the North Sea, a baseline gravity survey has been made over a site where CO_2 is being separated from natural gas, then injected into an underground saline aquifer. Uncertainty in the gravity measurements is estimated to be 4.3 μGal, making detection of small changes in gravity possible. 3-D modeling making use of both 4-D reflection seismic data and reservoir simulations indicates that the observed time-lapse gravity signal will depend on the density of the CO_2 within the reservoir, which in turn is highly dependent on the reservoir temperature. The time-lapse gravity signal is expected to range from 2-8 μGal/yr, making it a difficult signal to detect. Several years of time-lapse measurements are likely to be required before a robust estimate of the *in situ* CO_2 density can be made. However, an extremely high reservoir temperature (> 45 °C) would significantly lower the CO_2 density, making a much more easily observable gravity change. A repeat survey is planned for 2005, which would mean a three-year accumulation of CO_2 within the reservoir. Quantifying the reservoir characteristics and the behavior of CO_2 is essential for quantifying the contained mass. The ability to quantify the contained CO_2 mass is vital for this and for future sequestration efforts.

The second study examines Axial Seamount, a volcanic system located on the western side of the Juan de Fuca Ridge, which is influenced by both the ridge and a hot-spot. Water pressure measured at the seafloor was used as a proxy for relative depth of several seafloor benchmarks on the volcano. Five benchmarks were visited each year beginning in 2000, providing a five-year record of volcanic inflation following the its 1998 eruption. The data quality improved each year, as the technique and instruments were refined. The surface deformation data were used to estimate the location and volume change of the subsurface magma. The implied source location is consistent with seismic data for the area. These high precision pressure measurements have developed into a good technique for monitoring vertical deformation of the seafloor.

The third and final study presented in this dissertation was a spatial gravity survey done on Atlantis Massif, along the Mid-Atlantic Ridge. Modeling indicates the presence of a high-density wedge within the massif, consistent with a low-angle detachment fault. However, the density boundary required by the gravity data dips at a sharper angle than the surface expression of the fault does. This is probably due to a zone of serpentinized material along the fault, caused by exposure to seawater.

5.2 Future work

The first two studies discussed here have a time varying signal. A few years worth of data may not be enough to fully describe the long-term behavior of the systems in question. For this reason, it is important to continue monitoring for a decade or more from the present. At Sleipner, all of the injected CO_2 is expected to eventually accumulate beneath the caprock and begin to spread laterally. At this point, 4-D seismic reflection data may not be able to provide an adequate estimate of contained mass, since the thickness of the CO_2 layer may be greater than the tuning thickness (8 m). Some other verification technique will be important. Right now, time-lapse gravity is the only other monitoring technique available, making it crucial to continue making measurements. The first repeat gravity survey is planned for the summer of 2005.

Improvements to the ROVDOG instruments themselves that may produce higher precision measurements are underway. The major improvement is upgrading the internal gravimeters from the Scintrex CG-3M models that were used in the studies presented here to new Scintrex CG-5 models. Improvements in data reduction are possible as well. For instance, the change in gravity from earth tides could be measured by deploying one of the spare CG-3M gravimeters onto a benchmark in the survey area to continuously measure gravity throughout the duration of the survey. Gravity tides could then be extracted from the resulting data set and used to make corrections to the survey gravity data, rather than relying on predicted tidal values.

Injection of CO_2 into subsurface saline aquifers is one small but important way to begin to decrease greenhouse gas emissions. In conjunction with other emission reduction strategies, it may be possible to avoid a catastrophic climate change in the next 100 years. However, public awareness and concern is a vital key to this. Geophysical verification of injected CO_2 is a way not only to address the scientific challenge of quantifying the stored gas, but a way to determine whether or not the sequestration technique is stable and safe.

Axial Seamount marks the intersection of the Cobb-Eikelberg volcano chain and the Juan de Fuca Ridge. While its magma supply is likely linked to the nearby spreading axis plumbing, some researchers describe it simply as a small hotspot shield volcano not unlike Kilauea (except for its size). Recently, G. Kent and others [*Graham Kent*, private communications] carried out a reflection seismic survey of Axial Seamount, mapping the location of the magma chamber roof. Following what we have done at the Sleipner project, these data could provide a geometrical basis for a model that can account for the observed uplift on the surface and, if gravity measurements are added each year, a means to determine the density of the material that is producing the uplift. A study examining the ratio of gravity change over time to depth change over time ($\Delta g/\Delta z$), while quite common on land, has not been done for an undersea volcano. The amount of volatiles in the magma is not known and the presence of gas cannot be ruled out. In fact, we know so little about submarine volcanism that the opportunity to gain new information at such a well-studied site is important.

Details about the movement of magma in this complex system are beyond our ability to resolve with the current geodetic network, indicating the need for more comprehensive coverage. This could include more seafloor benchmarks, the addition of gravity measurements, and measurement of horizontal deformation using acoustic extensometers, for example. Axial Seamount is currently the best site to study a large basaltic seafloor volcano. A significant amount of work has been done at Axial, but a significant amount remains to be done. The opportunity to study the volcano through an eruptive cycle using geodetic, seismic, geochemical, and other types of measurements would be a large step in understanding all systems of this type.

Apart from these specific projects, the continuing development of seafloor geodetic instruments and techniques will provide a vital avenue of research for probing the physical evolution of our complex planet.

Appendix 1

ROVDOG instrument characterization

A1.1 Visco-elastic recovery effect

One important issue that is not addressed by *Sasagawa et al.* [2003] is that there is a visco-elastic recovery effect in the gravimeter springs due to tilt. All three CG-3M gravimeters used in the ROVDOG system show some amount of visco-elastic relaxation after being tilted over for more than five minutes. The cause of this phenomenon is that the length of the spring is kept constant by a force feedback system as long as the apparent gravity is within its dynamic range of about 8000 mGal. When a meter is tilted by more than about five degrees, however, the force feed back can no longer keep the mass centered, so it goes against the top stop. In this state, the spring becomes shorter until force feedback can re-center the mass, bringing the spring length back to its normal position. During the time the spring has been shortened, visco-elastic deformation of the spring takes place and some time is required for the spring to "recover" from this altered state. This behavior is called the recovery effect. The recovery appears to be exponential, leading to the equation

$$g_{obs} = g_{true} - \Delta g e^{-t/\tau}, \qquad \text{A1.1}$$

in which there are three unknown: the real gravity value (g_{true}), the amplitude of the effect (Δg), and the relaxation time (τ). We can write $\Delta g = g_{true} - g_0$, where g_0 is determined by taking the average of the first ten data points. Equation 1.2.1 then becomes

$$(g_{obs} - g_0) = \Delta g(1 - e^{-t/\tau}), \qquad \text{A1.2}$$

reducing the problem to two unknown parameters.

Laboratory tests were done to examine the recovery effect. In each test the meter in question was controlled by a Labview program which ran it through a sequence of actions for a preset number of iterations. This sequence consisted of two actions: 1. The meter was tilted for a set amount of time and then 2. It was leveled for a set amount of time. The resulting gravity data (gathered during the leveled periods) were first corrected for the solid earth tide and instrument drift. The records were then stacked and filtered to eliminate high frequency noise. Equation A1.2 was then fit to the data using a nonlinear fitting routine in Matlab (fminsearch), which iterates from a starting guess to find the best fit for both Δg and τ. An example is shown in Figure A1.1.

Units 1 and 2 show similar recovery effects in both amplitude and duration (around 0.1 mGal over 6-8 minutes), while Unit 3 shows recovery effects that are almost an order of magnitude lower in amplitude. From these tests, it is clear that the recovery from a constant tilt exceeding five minutes can have a large affect on measurements made within a 6-10 minute window following the tilting. More detailed results can be found in *Nooner et al.* [2002].

The sizes of the recoveries observed in the Sleipner survey (Figure 2.18) are about an order of magnitude lower than the laboratory values shown in Figure A1.1. This is primarily due to a transit leveling routine written by Glenn Sasagawa. While underway from one benchmark to the next, this routine was enabled, forcing each ROVDOG unit's gimbal motors to attempt to keep the gravimeters within a few degrees of level. This minimized gravimeter tilts and helped to keep the apparent gravity within each meters dynamic range.

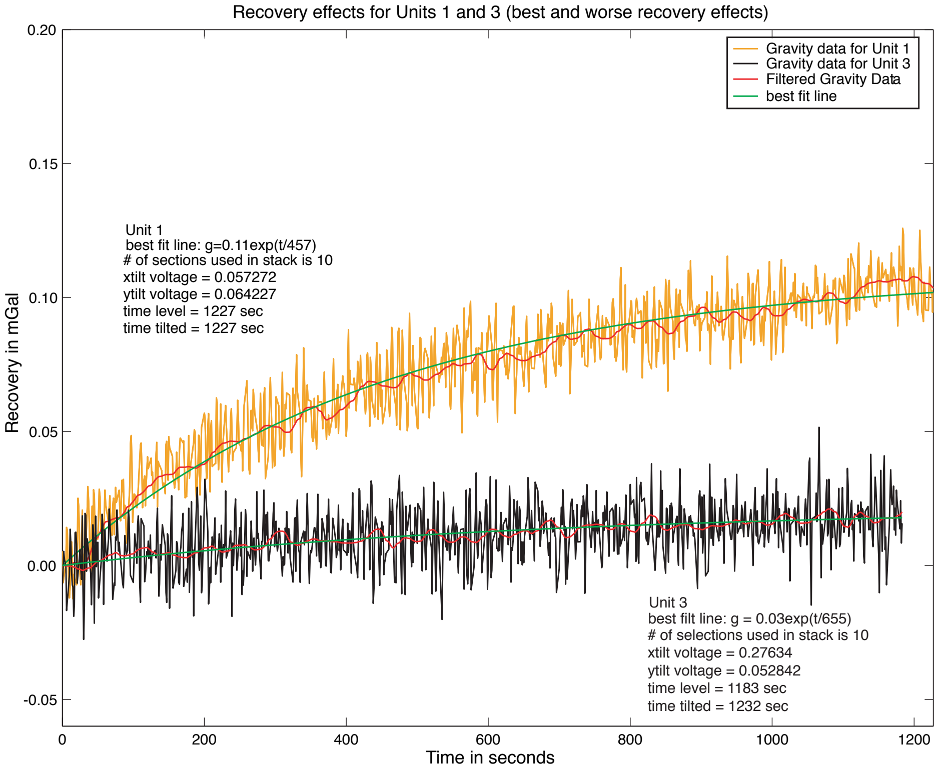

Figure A1.1 Results from laboratory experiments testing the visco-elastic recovery effects from tilting the ROVDOG CG-3M gravimeters at an angle of 10 degrees for about 20 minutes. The results shown are stacks of data from 10 repeated tilt and level cycles for Units 1 and 3, which have the largest and smallest effects respectively. The blue line shows the stacked data, the red line shows stacked data that have been low-pass filtered with a corner frequency of 0.033 Hz, and the green curve shows the best fitting exponential (from equation A1.2) to the filtered data set.

A1.2 Tilt meter calibration

Inside the temperature controlled core of the CG-3M gravimeters are high precision tilt meters. Over time, the voltage output of these tilt meters changes. Therefore, it is important to periodically re-calibrate them. The best way to do this is to tilt the gravimeter over a range of angles and use the apparent gravity as an absolute against which the tilt meters are calibrated. The apparent gravity changes proportionally to the cosine of the angle of tilt, θ, as follows:

$$g_{app} = g_0 \cos\theta \cong g_0(1-\theta^2) \qquad \text{A1.3}$$

where g_0 is the real local value of gravity and we have used the small angle approximation for $\cos\theta$. Therefore, the maximum apparent gravity occurs when the there is no tilt, meaning $\theta = 0$ and the output voltage from the tilt meter is V_{Null}. The relationship between the angle, θ, and the output voltage, V, and is linear and can be written as

$$\theta = \alpha(V - V_{Null}). \qquad \text{A1.4}$$

Tilt meter calibration in this way provides a method for finding the null voltage, V_{Null}, and the sensitivity, α, relating tilt voltage to angular displacement.

The CG-3M meters are relative gravimeters, meaning that there is an unknown offset between the real gravity, g_0, and the observed gravity from the gravimeter, g_{obs}. Taking this into account and substituting equation A1.4 into equation A1.3 yeilds

$$g_{obs} = g_0' - g_0\alpha^2(V - V_{Null})^2 \qquad \text{A1.5}$$

$$g_0' = g_0 + \text{constant}.$$

In order to solve this system of equations, the local value of gravity, g_0, must be known or guessed (although in practice, it makes little difference what value is chosen, as long as it is approximately 980000 mGal). The gravity versus tilt data can then be fit using a second order least squares. The voltage corresponding to the maximum gravity value in the fit is the null voltage, V_{Null}. The coefficients of the fit can be used to estimate the sensitivity, α.

In order to make the calibration process easy and reliable, I wrote code to automate the calibration routine. The program is in two parts, one Labview program to gather the data (tiltcal.vi), and one Matlab program to analyze the data (rovtilt.m). The Labview code has three modes of operation: low precision which makes six measurements along each axis at varying tilts; medium precision which makes twelve measurements; and high precision which makes twenty-four measurements. The data are recorded and can then be evaluated using rovtilt.m, which fits the data points to a parabola, finding the maximum value for g_0', which is then used to solve for the constant, α.

Equation A1.5 can be rewritten as

$$\Delta g = g_0 \alpha^2 \Delta V^2. \qquad \text{A1.6}$$

Typical values for the sensitivity are about 1.3 mRad/V. Putting the sensitivity and $g_0 = 980000$ mGal into equation A1.6 gives

$$\Delta g = 1.6562 \Delta V^2 \text{ mGal}, \qquad \text{A1.6}$$

indicating that a tilt of 0.1 V (~0.13 mRad) leads to a needed gravity correction of about 0.017 mGal. Uncertainty in the determination of the null voltage has been estimated to be about 0.03 V from the uncertainty in the parabolic fit to the tilt data. This leads to a gravity uncertainty of about 0.001 mGal for a perfectly leveled meter. In past surveys the tilt was kept to within 0.4 mRad (about 0.3 V). Thus, a tilt of 0.4 mRad (about 0.3 V) could cause an uncertainty in the observed gravity of up to 30 μGal.

Laboratory tests done in a cold vault have indicated that the null voltage may be somewhat temperature dependent, with V_{Null} decreasing by up to 0.03 V when the temperature changes from 22 ºC to 7 ºC. Thus, a tilt of 0.4 mRad (about 0.3 V) could cause an error in the observed gravity of up to 30 μGal if the tilt calibration is done on land (~22 ºC) and the measurements are made on the ocean floor (~7 ºC). However, a perfectly leveled meter would have an error of only 0.001 mGal. The sensitivity, α, does not appear to be temperature dependent, but is sensitive to the number of points used in the least squares fit. A deviation of 0.02 mRad/volt seems quite common, and corresponds to an uncertainty of 0.004 mGal for a tilt of 0.4 mRad.

From this it is clear that making high precision gravity measurements requires 1.) careful calibration of the tilt meters in conditions similar to what is expected during a survey and 2.) efforts to keep the amount of gravimeter tilt during measurements as small as possible. Therefore, the stable concrete benchmarks are crucial when attempting to observe gravity signals that are on the μGal level.

A1.3 Effect of tilt on pressure measurements

Each Paroscientific pressure gauge exhibits a DC shift in apparent pressure that is dependent on the spatial orientation of the gauge. This response is due to differential flexing of the C-shaped bourdon tube due to gravitational stressing (for an illustration of the Bourdon tube see Figure 3.2). The effect of rotation and tilt on the Paroscientific 31K pressure gauges used in the ROVDOG system was evaluated at atmospheric pressure in air. The rotations were made about both the long and short axes of the gauges as shown in Figure A1.2.

Rotations in φ where done first with θ held equal to zero (horizontal). The gauges were secured to a piece of steel channel bolted to an optical table. This allowed them to be rotated in a stable and repeatable way. In the experiment, two gauges were held fixed while a third was rotated. A measurement was made from all three gauges every 30 degrees. The data from the rotated gauge was then compared to the fixed gauges for quality control.

The gauges show a non-trivial response to rotation, which can be fit quite well by a sinusoidal curve (Figure A1.3). If the gauges are aligned so that a change in φ produces a minimum change in apparent pressure, a 10 degree rotation in φ causes an apparent depth change of about 0.1 cm in seawater (a rough estimate for conversion of depth to pressure for small changes in pressure is ~68 cm/psi in seawater). However, if the gauges are aligned so that a change in φ produces a maximum change in apparent pressure (90 degree rotation from the minimum case), a 10 degree rotation in φ causes an apparent depth change of about 1.6 cm in seawater (0.16 cm/degree).

The next experiment was done by changing θ while holding φ at a fixed angle. This was done for each gauge while holding the other two gauges fixed for references. The rotated gauge was attached to a rotating fixture on an optical table. Measurements were made every 20 or 30 degrees. This was done for φ = 0 and 90 degrees for all three gauges, and for φ = 45 degrees for gauge 88710.

The pressure gauge response to rotations in θ are about three to four times larger than for rotations in φ. Results are shown in Figures A1.4-A1.6. Again, the gauge response is fit quite well with a sinusoidal curve. If the gauges are aligned so that a change in θ produces a minimum change in apparent pressure (with the gauges oriented vertically), a 10 degree change in θ causes an apparent depth change of 0.4-0.5 cm in seawater. However, if the gauges are aligned so that a change in θ produces a maximum change in apparent pressure (gauges oriented horizontally), a 10 degree change in θ causes an apparent depth change of 4.3-5.3 cm in seawater (~0.5 cm/degree). Unfortunately, this is the orientation of the pressure gauges within the ROVDOG. Changing φ has a small effect of the experimental results, with a small amplitude difference as well as phase shift of up to 19 degrees in the observed pressure signal (Figures 3, 4, and 5). However, the amplitude and phase should not depend on φ, indicating perhaps imperfect alignment of the Bourdon tube within the outer stainless packaging.

The placement of the pressure gauges within the ROVDOG pressure case was determined prior to knowledge of the gauge sensitivity to tilts. The primary constraint was to minimize the size of the ROVDOG pressure cases. Therefore, the pressure gauges are constrained to lie horizontally with $\theta = 0$ degrees. This corresponds to the orientation of the largest $dg/d\theta$. Therefore, in high precision surveys, it is important to align the gauges to the orientation of minimum $dg/d\varphi$, reducing apparent depth changes related to tilts about that axis to < 0.1 cm (for tilts < 10 degrees). The larger problem (rotation in θ) is still a concern, however. Two things can be done to minimize this problem. 1.) By placing the ROVDOG on a benchmark in the same orientation each time a site is occupied, changes in gauge tilt for repeat occupations will be minimized. 2.) The measured response to tilt from Figures A1.4-A1.6 can be used to correct the data for any difference in benchmark tilt observed in repeated occupations.

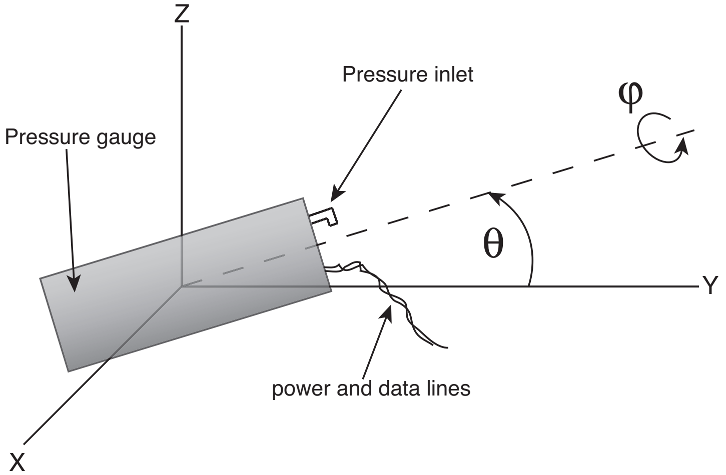

Figure A1.2 The rotation angles θ and φ are defined above in reference to a Cartesian coordinate system.

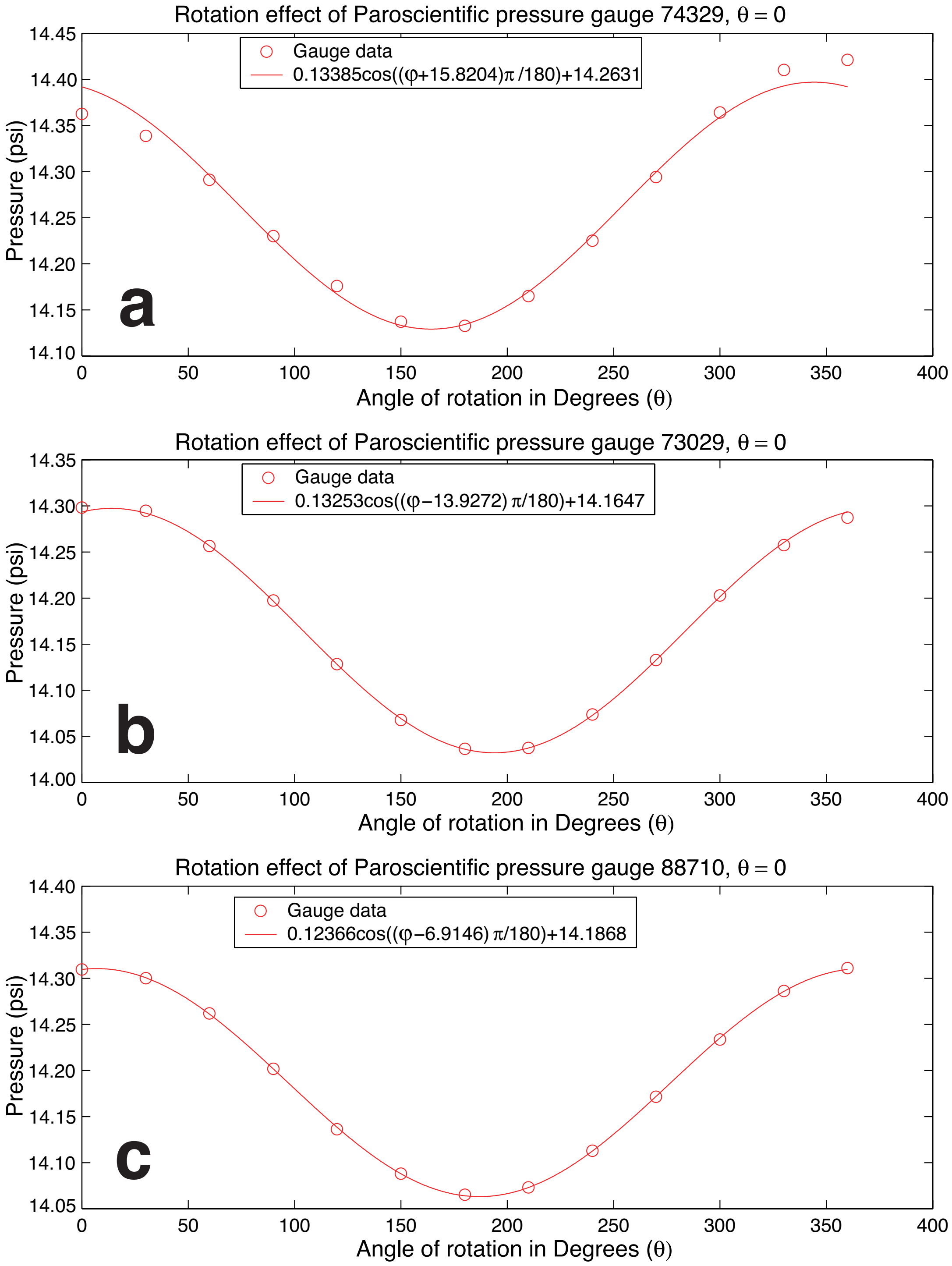

Figure A1.3 Paroscientific model 31K pressure gauge response to rotation about the long axis for gauges a.) 74329, b.) 73029, and c.) 88710.

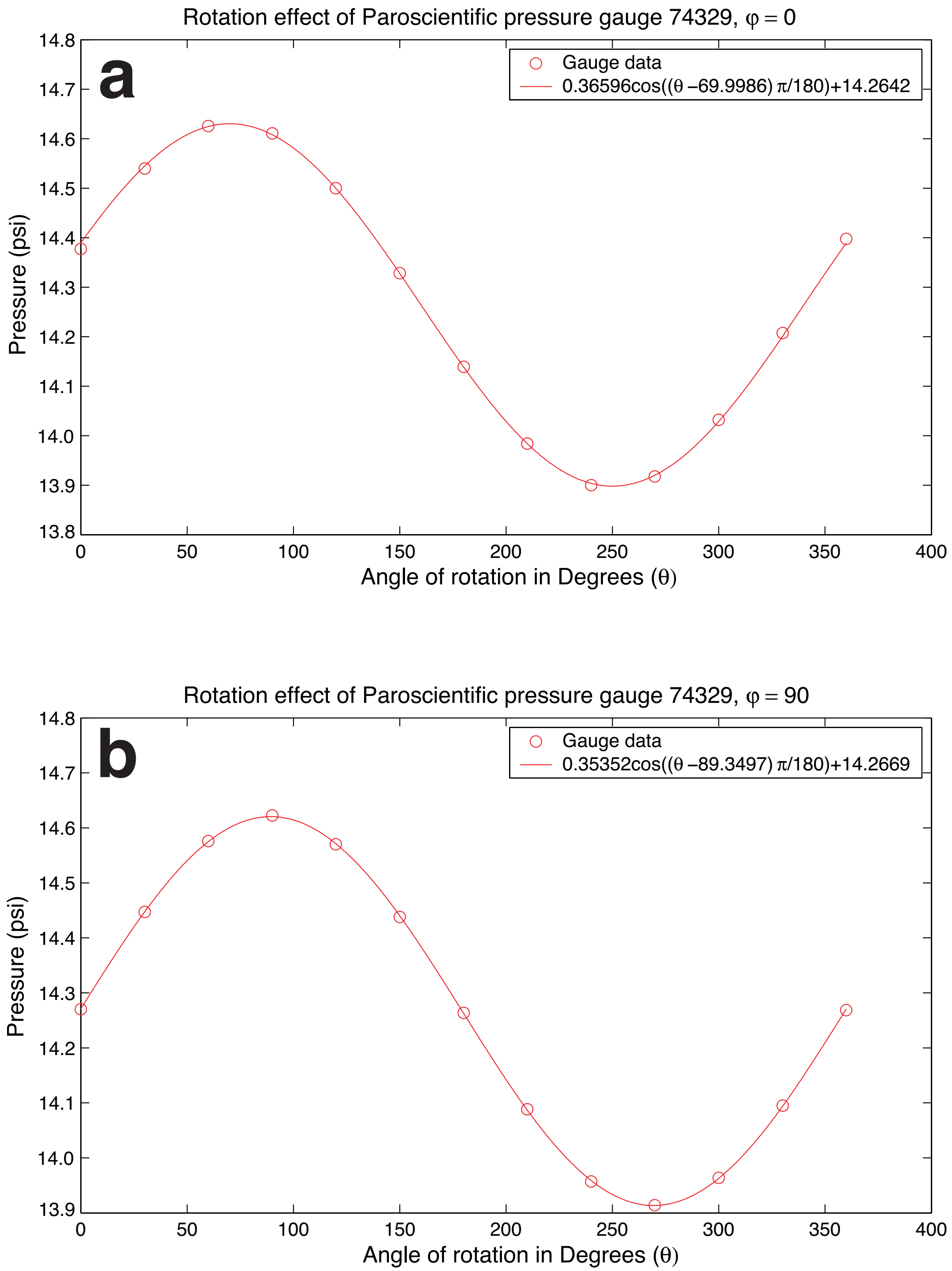

Figure A1.4 The pressure change in gauge 74329 for rotations in θ, holding φ constant at a.) 0 degrees and b.) 90 degrees.

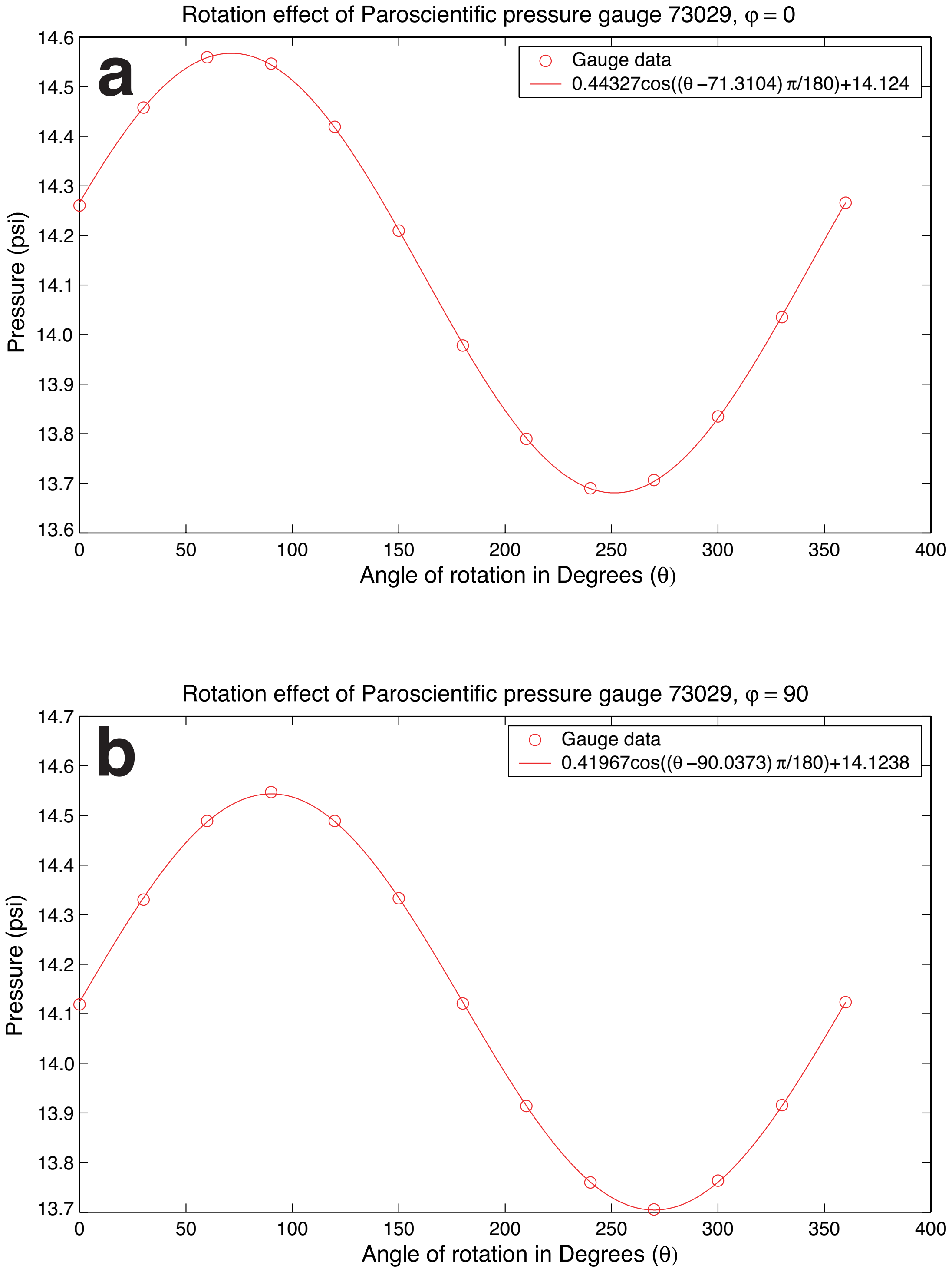

Figure A1.5 The pressure change in gauge 73029 for rotations in θ, holding φ constant at a.) 0 degrees and b.) 90 degrees.

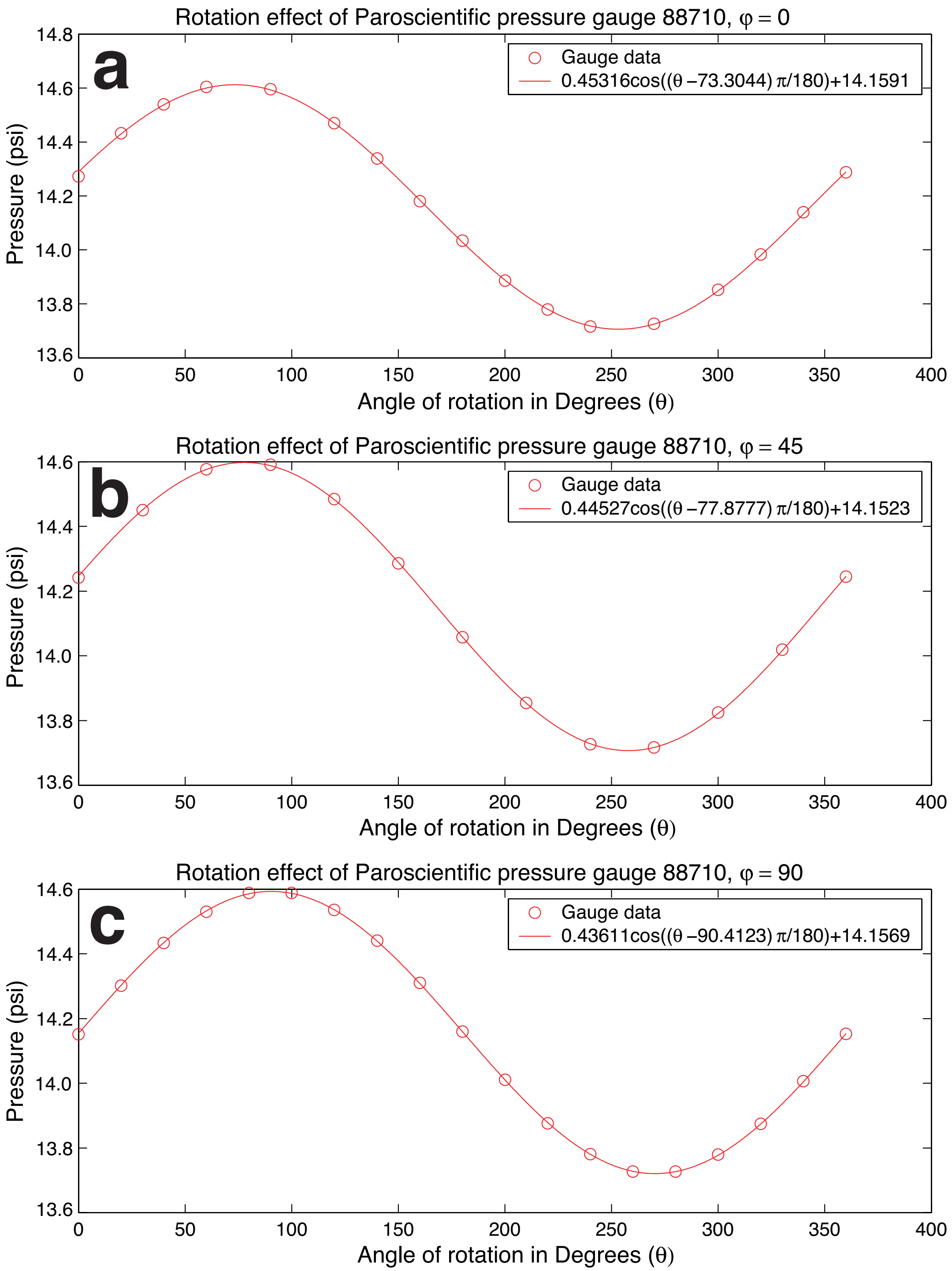

Figure A1.6 The pressure change in gauge 88710 for rotations in θ, holding φ constant at a.) 0 degrees, b.) 45 degrees, and c.) 90 degrees.

A1.4 References

Nooner, S., G. Sasagawa, and M. Zumberge, ROVDOG recovery testing, in *Laboratory evaluation of seafloor gravimeters: Statoil report*, pp. 5-11, Scripps Institution of Oceanography, La Jolla, CA, 2002.

Sasagawa, G., W. Crawford, O. Eiken, S. Nooner, T. Stenvold, and M. Zumberge, A new sea-floor gravimeter, *Geophysics*, *68*, 544-553, 2003.

Appendix 2

Instrumentation for each survey

Table A2.1 A list of the instruments used in each survey. P1-P3 lists the type (31K or 410K) and serial numbers of the pressure gauges. U1-U3 lists the ROVDOG sensor used.

Study	Year	P1	P2	P3	U1	U2	U3
Sleipner	2002	31K - 74329	31K - 73029	31K - 88710	9704391	9808423	9908435
Axial	2000	410K - 43886	410K - 53344	NA	NA	NA	NA
Axial	2001	410K - 43526	410K - 43535	NA	NA	NA	NA
Axial	2002	410K - 62201	410K - 43535	NA	NA	NA	NA
Axial	2003	410K - 62201	410K - 43535	NA	NA	NA	NA
Axial	2004	410K - 62201	410K - 43535	NA	NA	NA	NA
MAR	2000	410K - 43535	NA	NA	9704391	NA	NA

Appendix 3

Sleipner gravity data

Table A3.1 This table gives the gravity station number, the time of each measurement in Julian Days, raw gravity measurements at each site in mGal before tide and drift corrections were made (Note, the numbers in this column have been corrected for gravimeter temperature and tilt. To arrive at these numbers, at each site, approximately 15-20 minutes of 1 Hz data were gathered and then averaged.), and the uncertainty in the uncorrected gravity values of the previous column (This is based on the scatter of one second data that were averaged to obtain the previous column values.).

		Unit 1		**Unit 2**		**Unit 3**	
Station	**Day**	**Raw g (mGal)**	**Uncertainty (mgal)**	**Raw g (mGal)**	**Uncertainty (mGal)**	**Raw g (mGal)**	**Uncertainty (mGal)**
SP09	228.768	5950.898	0.532	5419.665	0.519	5962.597	0.624
SP08	228.803	5951.125	0.526	5419.917	0.513	5962.836	0.619
SP07	228.835	5951.438	0.462	5420.217	0.457	5963.099	0.536
SP06	228.864	5951.518	0.433	5420.287	0.422	5963.188	0.498
SP05	228.891	5951.671	0.465	5420.410	0.449	5963.316	0.529
SP04	228.917	5951.824	0.452	5420.542	0.440	5963.449	0.518
SP03	228.944	5951.996	0.437	5420.738	0.428	5963.609	0.500
SP02	228.973	5952.153	0.435	5420.881	0.426	5963.750	0.496
SP01	229.018	5952.471	0.422	5421.188	0.408	5964.050	0.482
SP09	229.070	5951.065	0.463	5419.768	0.449	5962.635	0.536
SP10	229.097	5950.910	0.445	5419.595	0.430	5962.461	0.513
SP11	229.127	5950.588	0.433	5419.285	0.425	5962.133	0.507
SP12	229.159	5950.398	0.457	5419.084	0.445	5961.923	0.527
SP13	229.184	5950.196	0.442	5418.879	0.431	5961.716	0.509
SP14	229.210	5949.780	0.522	5418.483	0.508	5961.314	0.608
SP15	229.241	5949.480	0.581	5418.183	0.562	5960.989	0.673
SP16	229.268	5949.022	0.598	5417.699	0.586	5960.524	0.693
SP17	229.295	5948.698	0.614	5417.389	0.594	5960.185	0.710
SP18	229.324	5948.270	0.767	5416.957	0.740	5959.745	0.906
SP19	229.353	5947.819	0.970	5416.507	0.937	5959.302	1.133
SP20	229.381	5947.812	1.043	5416.490	1.012	5959.270	1.216

		Unit 1		Unit 2		Unit 3	
Station	Day	Raw g (mGal)	Uncertainty (mgal)	Raw g (mGal)	Uncertainty (mGal)	Raw g (mGal)	Uncertainty (mGal)
SP09	229.455	5951.193	1.351	5419.867	1.311	5962.616	1.555
SP21	229.488	5952.075	1.360	5420.762	1.327	5963.524	1.564
SP28	229.531	5952.931	1.183	5421.588	1.154	5964.353	1.350
SP27	229.568	5952.419	1.139	5421.086	1.111	5963.841	1.329
SP22	229.595	5951.985	1.156	5420.634	1.115	5963.367	1.337
SP23	229.624	5951.670	1.124	5420.310	1.100	5963.043	1.311
SP09	229.662	5951.426	1.192	5420.042	1.164	5962.761	1.368
SP26	229.694	5950.337	1.254	5418.985	1.211	5961.682	1.428
SP30	229.737	5949.703	1.188	5418.330	1.159	5957.437	1.238
SP29	229.765	5950.267	1.188	5418.890	1.170	5958.146	0.137
SP25	229.879	5950.783	1.097	5419.431	1.077	5962.064	1.257
SP24	229.913	5951.192	1.101	5419.835	1.072	5962.460	1.273
SP09	229.947	5951.572	1.056	5420.185	1.043	5962.821	1.212
SP07	229.980	5952.083	1.084	5420.687	1.053	5963.316	1.258
SP05	230.013	5952.299	1.177	5420.902	1.150	5963.533	1.363
SP03	230.046	5952.596	1.413	5421.191	1.375	5963.821	1.620
SP01	230.087	5953.022	1.083	5421.642	1.055	5964.244	1.256
SP02	230.119	5952.749	1.183	5421.356	1.143	5963.947	1.349
SP04	230.149	5952.444	1.182	5421.055	1.143	5963.636	1.360
SP06	230.179	5952.214	1.216	5420.801	1.179	5963.390	1.405
SP08	230.211	5951.870	1.130	5420.453	1.092	5963.026	1.302
SP09	230.241	5951.637	1.201	5420.210	1.172	5962.783	1.400
SP20	230.300	5948.337	1.331	5416.927	1.314	5959.462	1.545
SP18	230.336	5948.833	1.295	5417.399	1.258	5959.935	1.509
SP16	230.373	5949.644	1.293	5418.202	1.253	5960.737	1.515
SP14	230.406	5950.427	1.267	5418.977	1.236	5961.504	1.481
SP12	230.442	5951.035	1.267	5419.580	1.235	5962.102	1.483
SP10	230.473	5951.577	1.300	5420.118	1.263	5962.648	1.507
SP09	230.497	5951.775	1.333	5420.308	1.292	5962.830	1.540
SP11	230.524	5951.334	1.337	5419.859	1.299	5962.378	1.543
SP13	230.552	5950.959	1.501	5419.487	1.450	5961.987	1.733
SP15	230.581	5950.285	1.613	5418.820	1.552	5961.316	1.864
SP17	230.615	5949.522	1.400	5418.062	1.374	5960.558	1.637
SP19	230.644	5948.689	1.825	5417.209	1.796	5959.690	2.138
SP20	230.674	5948.678	1.616	5417.193	1.564	5959.666	1.859
SP09	230.742	5952.013	1.753	5420.528	1.712	5962.981	2.026
SP23	230.776	5952.326	2.009	5420.839	1.947	5963.294	2.303
SP27	230.805	5953.165	1.942	5421.683	1.897	5964.131	2.233
SP28	230.833	5953.723	1.889	5422.234	1.848	5964.665	2.181
SP22	230.869	5952.704	1.822	5421.219	1.782	5963.640	2.096
SP21	230.897	5952.965	1.908	5421.472	1.872	5963.896	2.194
SP24	230.939	5951.773	2.210	5420.281	2.101	5962.664	2.547

		Unit 1		Unit 2		Unit 3	
Station	**Day**	**Raw g (mGal)**	**Uncertainty (mgal)**	**Raw g (mGal)**	**Uncertainty (mGal)**	**Raw g (mGal)**	**Uncertainty (mGal)**
SP29	230.970	5950.917	2.009	5419.413	1.959	5961.807	2.298
SP30	230.999	5950.390	1.979	5418.876	1.934	5961.267	2.268
SP26	231.037	5951.058	1.911	5419.550	1.873	5961.932	2.195
SP25	231.066	5951.453	1.960	5419.933	1.917	5962.321	2.236
SP09	231.093	5952.206	1.739	5420.691	1.694	5963.055	1.966
SP30	231.147	5950.474	1.770	5418.942	1.723	5961.283	2.012
SP29	231.176	5951.016	1.859	5419.479	1.811	5961.821	2.129
SP25	231.203	5951.513	1.759	5419.959	1.727	5962.290	2.021
SP08	231.231	5952.459	1.627	5420.910	1.594	5963.235	1.872
SP24	231.260	5951.878	1.840	5420.330	1.795	5962.646	2.111
SP07	231.288	5952.707	1.773	5421.166	1.734	5963.463	2.041
SP21	231.316	5953.110	1.801	5421.556	1.765	5963.857	2.076
SP09	231.344	5952.211	1.779	5420.663	1.737	5962.955	2.059
SP06	231.380	5952.789	1.643	5421.213	1.614	5963.521	1.870
SP05	231.408	5952.907	1.685	5421.348	1.627	5963.639	1.919
SP04	231.434	5953.058	1.668	5421.488	1.647	5963.780	1.919
SP03	231.460	5953.241	1.729	5421.671	1.682	5963.948	1.967
SP02	231.486	5953.402	2.043	5421.840	1.997	5964.102	2.262
SP01	231.518	5953.728	1.614	5422.142	1.557	5964.418	1.846
SP04	231.552	5953.186	1.578	5421.613	1.565	5963.870	1.839
SP09	231.587	5952.417	1.622	5420.833	1.572	5963.081	1.813
SP14	231.621	5951.200	1.694	5419.612	1.650	5961.837	1.915
SP15	231.648	5950.929	1.858	5419.348	1.802	5961.561	2.096
SP16	231.673	5950.490	1.801	5418.905	1.765	5961.139	2.047
SP17	231.700	5950.180	1.848	5418.586	1.822	5960.800	2.093
SP18	231.724	5949.744	1.896	5418.165	1.851	5960.361	2.160
SP19	231.753	5949.322	2.022	5417.725	1.933	5959.920	2.272
SP20	231.778	5949.287	1.815	5417.696	1.796	5959.885	2.079
SP16	231.816	5950.583	1.833	5419.003	1.791	5961.163	2.068
SP09	231.859	5952.622	1.800	5421.028	1.742	5963.198	2.046
SP28	231.899	5954.308	1.799	5422.723	1.726	5964.862	2.062
SP27	231.927	5953.781	1.886	5422.196	1.810	5964.331	2.112
SP22	231.956	5953.310	1.856	5421.700	1.817	5963.837	2.104
SP10	231.986	5952.542	1.823	5420.921	1.792	5963.059	2.091
SP23	232.014	5953.010	1.732	5421.417	1.688	5963.520	1.987
SP11	232.043	5952.249	1.949	5420.657	1.899	5962.750	2.238
SP26	232.073	5951.665	2.095	5420.040	2.025	5962.151	2.397
SP12	232.107	5952.099	2.400	5420.470	2.333	5962.571	2.816
SP13	232.132	5951.897	2.586	5420.266	2.523	5962.374	3.020
SP09	232.165	5952.793	2.886	5421.180	2.819	5963.240	3.371
SP30	232.205	5951.008	2.907	5419.397	2.794	5961.469	3.414
SP20	232.272	5949.481	2.571	5417.834	2.493	5959.906	3.014

		Unit 1		Unit 2		Unit 3	
Station	Day	Raw g (mGal)	Uncertainty (mgal)	Raw g (mGal)	Uncertainty (mGal)	Raw g (mGal)	Uncertainty (mGal)
SP28	232.335	5954.439	2.463	5422.823	2.397	5964.830	2.889
SP27	232.364	5953.919	2.626	5422.288	2.546	5964.299	3.075
SP01	232.431	5954.185	2.281	5422.536	2.204	5964.549	2.695
SP09	232.481	5952.820	2.066	5421.184	2.004	5963.167	2.466
SP31	232.509	5952.683	2.086	5421.057	2.036	5963.056	2.707
SP32	232.528	5952.679	2.304	5421.036	2.223	5963.052	2.733
SP33	232.546	5952.695	2.523	5421.053	2.433	5963.017	2.977
SP34	232.568	5952.641	2.942	5420.989	2.897	5962.947	3.571
SP35	232.593	5952.472	3.085	5420.826	2.960	5962.769	3.637
SP09	232.618	5952.995	3.017	5421.304	2.921	5963.284	3.533

Table A3.2 This gives the gravity station number, the coordinates in UTM, and the average value of gravity at each site corrected for tide and drift, the number of visits per station, the mean depth of each station in meters (from the pressure gauges), and the mean gravity in mGal for each station relative to station SP09.

Station	UTM East	UTM North	# visits	Depth (m)	Gravity (mGal)
SP01	435836	6472219	4	83.682	1.402
SP02	436494	6471980	3	82.898	1.107
SP03	436776	6471877	3	82.635	0.970
SP04	437058	6471775	4	82.332	0.818
SP05	437340	6471672	3	82.093	0.689
SP06	437622	6471569	3	81.841	0.571
SP07	437810	6471501	3	81.753	0.482
SP08	438171	6471369	3	81.506	0.228
SP09	438468	6471262	15	81.320	0.000
SP10	438749	6471159	3	81.125	-0.162
SP11	439031	6471056	3	80.929	-0.481
SP12	439313	6470954	3	80.767	-0.678
SP13	439595	6470851	3	80.601	-0.879
SP14	439971	6470714	3	80.475	-1.271
SP15	440347	6470577	3	80.318	-1.583
SP16	440817	6470406	4	80.071	-2.027
SP17	441287	6470235	3	79.883	-2.372
SP18	441756	6470064	3	79.744	-2.819
SP19	442226	6469893	3	79.616	-3.265
SP20	442696	6469722	5	79.563	-3.305
SP21	438169	6471902	3	81.615	0.885
SP22	438639	6471731	3	81.297	0.637
SP23	439108	6471560	3	80.969	0.301
SP24	437827	6470963	3	81.606	-0.352
SP25	438296	6470792	3	81.296	-0.726
SP26	438766	6470621	3	80.995	-1.091
SP27	438810	6472201	4	81.231	1.135
SP28	438981	6472671	4	81.250	1.664
SP29	438125	6470322	3	81.234	-1.216
SP30	437954	6469852	4	81.116	-1.765
SP31*	438750	6471137	1	81.486	1.402
SP32*	438751	6471116	1	81.491	1.107
SP33*	438751	6471094	1	81.482	0.970
SP34*	438753	6471051	1	81.466	0.818
SP35*	438756	6470944	1	81.453	0.689

*SP31-SP35 were measurements made on the seafloor with no benchmark.

Appendix 4

MAR data reduction, modeling, and raw data

A4.1 MAR data reduction

Prior to the cruise, we used the ROVDOG to observe gravity at an absolute gravity base station in Bermuda; at the end of the cruise (36 days later), observations were made at a second absolute gravity base station in Woods Hole, MA. During the cruise only one station was occupied twice during the survey, separated by 13 days. The drift coefficient, as determined by the absolute gravity station ties and verified by the inter-survey repeat was 0.264 ± 0.0004 mGal/day.

Numerically predicted tidal corrections [*Agnew*, 1996; *Agnew*, 1997] were also applied to the data. These consider the elastic solid earth tidal response, the ocean loading response, and the gravitational attraction of the water overhead. The maximum correction was 0.0612 mGal. Corrections for latitude were made using the 1967 Geodetic Reference System (GRS 67) Formula [e.g. *Turcotte and Schubert*, 1982]. The N-S gradient at this experiment's latitude is 78.36 mGal/degree; the observations spanned a 2.532 km N-S interval, giving a maximum correction of 1.793 mGal. The uncertainty in this correction is due to uncertainty in map and site coordinates, which we believe to be 100 m. This corresponds to an uncertainty of

0.071 mGal. A depth dependent free-water correction was made folowing the formulation of *Stacey et al*. [1982]. This rigorous treatment was necessary because of the large vertical extent of the survey. The maximum depth difference among the sites was 1311.18 m, corresponding to a maximum correction in gravity of 291.118 mGal. We conservatively estimate the uncertainty in this correction to be 0.030 mGal, due to the variability of seawater density at these depths. Lithospheric cooling effects were also subtracted from the Bouguer anomaly, following *Phipps Morgan and Forsyth* [*Phipps Morgan and Forsyth*, 1988].

A4.2 Best-fitting density models to the Atlantis oceanic core-complex

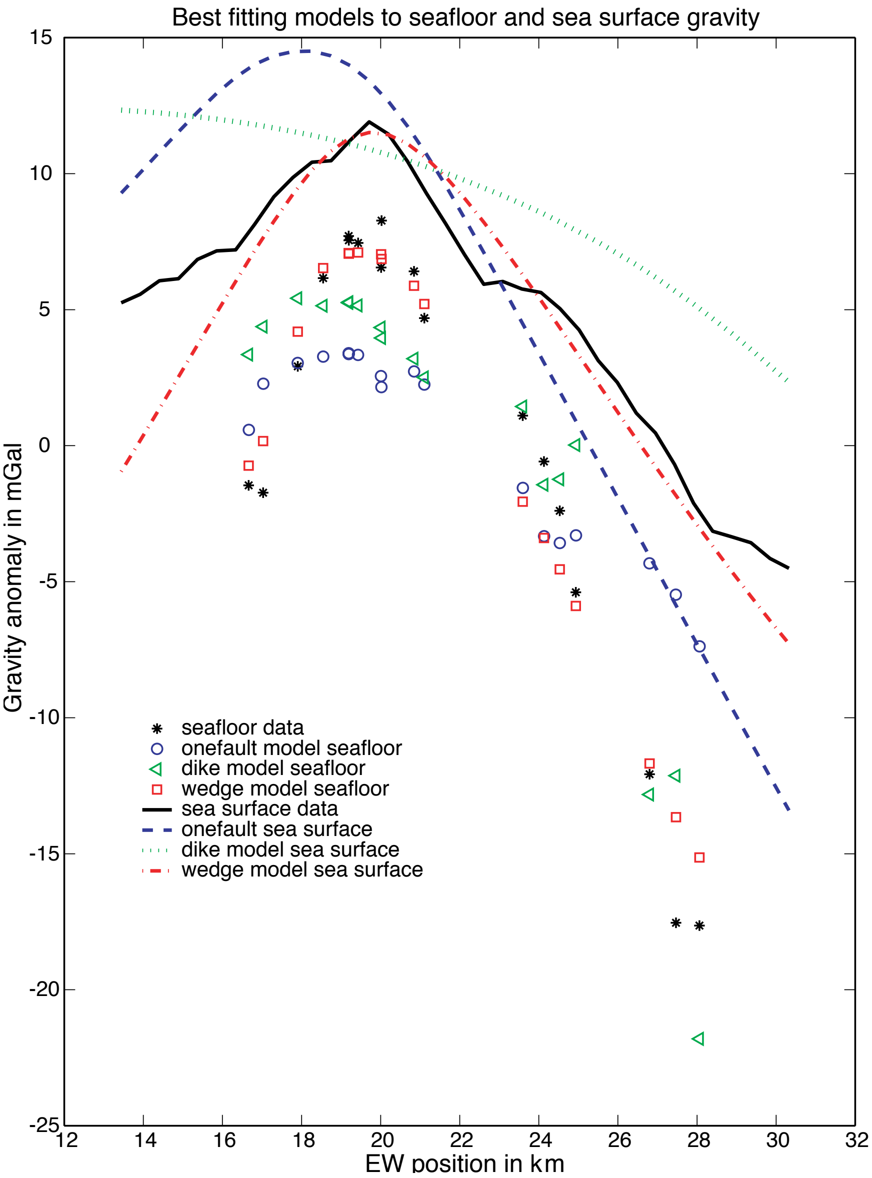

Figure A4.1 This figure shows the best model predictions for each geometry (one-fault model, dike model, and wedge model). Both seafloor and sea surface results are shown. The wedge model is obviously the best fitting model. Furthermore, in the figure, the one-fault and dike models are not constrained to simultaneously fit both the seafloor and the sea surface data. This means that the geometry corresponding to the best fitting line to the sea surface data is not the same as the geometry corresponding to the best fitting line to the seafloor data. The wedge model is constrained to fit both data sets.

A4.3 MAR gravity data

Table A4.1 Gives the DSV Alvin dive number for each gravity measurement, gravity site number during each dive, the Latitude of each site in degrees north, the Longitude of each site in degrees west, the depth below sea level of each site in meters, the time of each measurement in Julian Days, raw gravity measurements at each site in mGal before corrections were made (Note, the numbers in this column have been corrected for gravimeter temperature and tilt. To arrive at these numbers, at each site, approximately 15-20 minutes of 1 Hz data were gathered and then averaged.), and the uncertainty in the uncorrected gravity values of the previous column (This is based on the scatter of one second data that were averaged to obtain the previous column values.).

Dive #	Site	Latitude	Longitude	Depth	Day	Raw gravity (mGal)	Uncertainy (mGal)
3642	1	30.1758	42.1053	1883.49	329.488	4164.918	0.157
3642	2	30.1747	42.1081	1811.66	329.54	4155.657	0.007
3642	3	30.1756	42.1167	1772.87	329.59	4151.043	0.01
3642	4	30.1716	42.1166	1757.2	329.647	4149.264	0.009
3642	5	30.1707	42.1228	1651.1	329.696	4131.809	0.008
3642	6	30.1703	42.1252	1643.49	329.717	4130.93	0.007
3643	1	30.186	42.0794	2408.55	330.553	4242.7	0.008
3643	2	30.188	42.074	2561.56	330.654	4265.096	0.01
3643	3	30.1901	42.0697	2608.8	330.688	4271.271	0.009
3643	4	30.1913	42.0655	2596.02	330.724	4266.54	0.009
3644	1	30.1817	42.033	2954.67	331.524	4300.557	0.006
3644	2	30.1814	42.0391	2596.6	331.651	4244.457	0.01
3644	3	30.1821	42.046	2641.31	331.713	4262.179	0.017
3653	1	30.1703	42.1252	1644.02	343.538	4134.465	0.007
3653	2	30.1701	42.132	1647.02	343.597	4133.122	0.005
3653	3	30.1685	42.1386	1658.86	343.638	4132.315	0.007
3653	4	30.1708	42.1478	1722.79	343.672	4138.411	0.006
3653	5	30.1695	42.1516	1808.15	343.698	4151.846	0.006

A4.4 References

Agnew, D.C., SPOTL: Some programs for ocean tide loading, in *SIO Reference Series*, La Jolla, CA, 1996.

Agnew, D.C., NLOADF: a program for computing ocean-tide loading, *Journal of Geophysical Research*, *102*, 5109-5110, 1997.

Phipps Morgan, J., and D.W. Forsyth, Three-dimensional flow and temperature perturbations due to a transform offset: Effects on oceanic crustal and upper mantle structure, *Journal of Geophysical Research*, *93*, 2955-2966, 1988.

Sasagawa, G., W. Crawford, O. Eiken, S. Nooner, T. Stenvold, and M. Zumberge, A new sea-floor gravimeter, *Geophysics*, *68*, 544-553, 2003.

Stacy, F.D., G.J. Tuck, S.C. Holding, A.R. Maher, and D. Morris, Constraint on the planetary scale value of the Newtonian gravitational constant from the gravity profile within a mine, *Physical Review D*, *23*, 1683-1692, 1982.

Turcotte, D.L., and G. Schubert, *Geodynamics: Applications of Continuum Physics to Geological Problems*, John Wiley and Sons, New York, 1982.